



POLITECNICO DI TORINO
MASTER OF SCIENCE IN ENVIRONMENTAL AND LAND ENGINEERING
CLIMATE CHANGE
ACADEMIC YEAR 2021-2022
GRADUATION SESSION: DECEMBER 2022

Analysis of the impacts of Arctic sea ice decrease on future climate change

MASTER DEGREE THESIS

Supervisor

Prof. Jost VON HARDENBERG

Co-supervisor

Prof. Katinka BELLOMO

Candidate

Matteo MIGONE

Torino, 2022



Politecnico di Torino

Abstract

Sea ice cover is one of the key components of the Earth's climate system and regulates global weather and climate through a number of processes. Observations show that Arctic sea ice is undergoing a dramatic reduction, enhanced by the phenomenon of polar amplification, mediated by the sea-ice-albedo feedback, with potentially important impacts on climate change in a broad range of regions also outside the polar areas.

The objective of this thesis is to investigate the global climate response to projected future Arctic sea ice loss, through the analysis of the patterns of many relevant climate variables. The study is carried out on an ensemble of 32 global climate models belonging to the CMIP6 framework. Their future projections following the SSP1-2.6, SSP2-4.5 and SSP5-8.5 scenarios are studied and post-processed until the end of the century. Two reference time intervals are evaluated in the historical and future periods. For each model, sea ice cover differences between the two time frames are computed and normalised by the corresponding differences in global mean surface temperature (GMT), in order to limit the influence of GMT on the results. Models are then divided into two clusters: one including models that project smaller normalised Northern Hemisphere sea ice cover difference, and one including models that project greater normalised Northern Hemisphere sea ice cover difference. The differences between the two clusters are attributed to the impacts of sea ice decrease, and are supported by rigorous statistical testing. The effects of the difference in the amount of sea ice decrease between the two clusters are studied at four levels of global mean temperature warming relative to the historical baseline, thus allowing us to evaluate models by global warming levels, independently from the specific SSP scenario.

Arctic sea ice loss impacts are investigated at global scale and for several climate variables (e.g., temperature, precipitation, sea level pressure and geopotential height), and for the atmospheric circulation by examining future zonal wind and mass streamfunction changes. Moreover, an analysis using the Empirical Orthogonal Function (EOF) is carried out, in order to detect variations in the mean patterns of large-scale variability, in particular in the North Atlantic Oscillation (NAO). Sea ice effects are studied both on an annual and seasonal (winter and summer) time scales. It arises that at the same global warming level, sea ice affects temperature not homogeneously in the Northern Hemisphere. Models projecting the stronger decline in Arctic sea ice exhibit precipitation increase in Central-Northern Europe and a marked annual mean precipitation increase in Central Africa. Furthermore, the variation in sea ice cover modifies the strength of the Hadley cell, as well as modifications in other climate variables patterns. Our work confirms results from existing literature, which focuses mainly on the winter impacts of sea ice decrease, also proving the soundness of our approach, and further expands upon them by analysing impacts on a broader range of regions. Therefore, the thesis constitutes an important contribution in the framework of the investigation of the climatic consequences of projected Arctic sea ice loss.

*A mamma e papà,
ai miei nonni,
a Vittoria,
che da sempre credono in me.*

Contents

| | |
|--|-----------|
| Abstract | 1 |
| 1 Arctic sea ice cover: historical and current records | 15 |
| 1.1 Sea ice description | 15 |
| 1.1.1 Quantities to define sea ice cover | 16 |
| 1.2 Historical records | 17 |
| 1.3 Trend in the last decades | 18 |
| 1.4 Future projections | 20 |
| 2 Motivation: the impact of sea ice reduction | 23 |
| 2.1 Literature review on the topic | 24 |
| 3 Methodology | 27 |
| 3.1 Climate models | 29 |
| 3.1.1 CMIP6 models employed | 30 |
| 3.1.2 SSP scenarios | 32 |
| 3.2 Data and methods | 35 |
| 4 Definition of clusters of models based on sea ice cover projections | 37 |
| 4.1 Correlation between global mean temperature and Arctic sea ice cover | 39 |
| 4.2 Definition of clusters of models | 43 |
| 4.2.1 EC-Earth3 ensemble test | 47 |
| 4.3 Global warming levels definition | 48 |
| 5 Northern Hemisphere sea ice cover and temperature distributions in the two clusters | 55 |
| 5.1 Measure of the significance of the results | 56 |
| 5.2 Sea ice cover distribution | 57 |
| 5.3 Surface temperature distribution | 60 |
| 6 Impacts of sea ice decrease on the clusters' global climatology | 63 |
| 6.1 Surface temperature distribution | 63 |
| 6.2 Precipitation distribution | 66 |
| 6.3 Sea level pressure and geopotential height distributions | 69 |
| 6.4 Impacts on global atmospheric circulation | 73 |
| 6.4.1 Mean zonal wind patterns | 73 |

| | |
|---|-----------|
| 6.4.1.1 Northern Hemisphere 850-hPa zonal wind distribution | 77 |
| 6.4.2 Changes in the meridional mass streamfunction | 80 |
| 6.4.3 North Atlantic Oscillation (NAO) analysis | 86 |
| Conclusions | 89 |
| Bibliography | 98 |
| Abbreviations | 99 |

List of Figures

| | | |
|-----|--|----|
| 1.1 | Chunks of sea ice, melt ponds and open water are all seen in this image captured at an altitude of 1500 feet (457 m) by the NASA's Digital Mapping System instrument during an Operation IceBridge flight over the Chukchi Sea on Saturday, July 16, 2016. Credit: NASA's Goddard Space Flight Center [1]. | 16 |
| 1.2 | 10-year averages between 1979 and 2018 and yearly averages for 2007, 2012, and 2022 of the daily (a) ice extent and (b) ice area in the Northern Hemisphere and a listing of the extent and area of the current, historical mean, minimum, and maximum values in km^2 . The dashed vertical line indicates 12 th October 2022 values. Credit: NASA's Goddard Space Flight Center [2]. | 17 |
| 1.3 | Total maximum (green) and minimum (blue) ice extent time series for the period 1870-2003. Thick lines are robust spline functions to highlight low-frequency changes. Vertical dotted lines separate the three periods for which data sources changed fundamentally: (1) 1870-1952: observations of varying accuracy/availability; (2) 1953-1971: generally accurate hemispheric observations; (3) 1972-2003: satellite period – best accuracy and coverage. Figure and caption from Kinnard et al., 2008 [3]. | 18 |
| 1.4 | Monthly average sea ice extent for (a) March 2021, and (b) September 2021. The median extent for 1981-2010 is shown by the magenta contour. Figure and caption from Meier et al., 2021 [4]. | 20 |

| | | |
|-----|--|----|
| 1.5 | Northern Hemisphere (NH) sea ice extent in September over the late 20 th century and the whole 21 st century for the scenarios RCP2.6, RCP4.5, RCP6.0 and RCP8.5 in the CMIP5 models, and corresponding maps of multi-model results in 2081-2100 of NH September sea ice extent. In the time series, the number of CMIP5 models to calculate the multi-model mean is indicated (subset in brackets). Time series are given as 5-year running means. The projected mean sea ice extent of a subset of models that most closely reproduce the climatological mean state and 1979-2012 trend of the Arctic sea ice is given (solid lines), with the minimum to maximum range of the subset indicated with shading. Black (grey shading) is the modelled historical evolution using historical reconstructed forcings. The CMIP5 multi-model mean is indicated with dashed lines. In the maps, the CMIP5 multi-model mean is given in white and the results for the subset in grey. Filled areas mark the averages over the 2081-2100 period, lines mark the sea ice extent averaged over the 1986-2005 period. The observed sea ice extent is given in pink as a time series and averaged over 1986-2005 as a pink line in the map. Figure and caption from IPCC (2013), Assessment Report 5, Working Group I, Technical Summary, Fig. TS.17 [5]. | 21 |
| 3.1 | Schematic representation of the functioning of a Global Climate Model. Credit: National Oceanic and Atmospheric Administration (NOAA) [6]. | 30 |
| 3.2 | SSP-RCP scenario matrix illustrating CMIP6 simulations. Each cell indicates a combination of SSPs and climate outcome based on a particular forcing pathway. Dark blue cells indicate the key scenarios at the basis of climate model projections; light blue cells indicate additional scenarios of interest. White cells indicate scenarios for which climate information is supposed to come from the SSP scenario simulated for that row. Green cells indicate the corresponding CMIP5 RCPs for each row, which were developed from previous socio-economic scenarios rather than SSPs. Figure taken from O'Neill et al., 2016 [7]. | 34 |
| 3.3 | Future annual emissions of CO ₂ across the five SSP scenarios. Figure taken from IPCC (2021), Assessment Report 6, Working Group I, Summary for Policymakers, Fig. SPM.4 [8]. | 35 |
| 4.1 | Northern Hemisphere sea ice area anomaly from 1850-1950 average under the three scenarios. | 38 |
| 4.2 | Scatter plots showing, in each scenario, the relation between sea ice difference and global mean temperature difference for every model. Differences are computed between the means of the periods 2070-2099 and 1850-1950. In the left plots, Northern Hemisphere sea ice is considered, in the right ones all world sea ice. . . . | 40 |
| 4.3 | 21-year moving average filtered timeseries of (left) Northern Hemisphere sea ice area and (right) GMT anomalies from 1850-1950 average under the three scenarios. | 42 |
| 4.4 | Northern Hemisphere sea ice area anomaly as function of GMT anomaly. Based on 21-year moving average filtered timeseries. | 43 |

LIST OF FIGURES

| | | |
|-----|---|----|
| 4.5 | Scatter plots of NH sea ice difference against global mean temperature difference for every model showing, in each scenario, the division of the models in terciles. Differences are computed between the means of the periods 2070-2099 and 1850-1950. | 45 |
| 4.6 | Scatter plot of NH sea ice difference against global mean temperature difference for every model of the scenario SSP2-4.5, showing the division of the models in terciles and the ensemble of realisations of the model EC-Earth3 (in green). Differences are computed between the means of the periods 2070-2099 and 1850-1950. | 48 |
| 4.7 | Scatter plot of NH sea ice anomalies compared to 1850-1950 average – from the filtered timeseries – at $\text{GWL} = +2\text{ }^\circ\text{C}$: SSP2-4.5 versus SSP5-8.5. | 53 |
| 5.1 | Northern Hemisphere maps (for latitudes north of 30° N) of yearly average sea ice cover and surface temperature (tas) anomalies relative to 1850-1950 mean (Δ) for the four GWLs. Left: mean of the models of cluster "smaller"; center: mean of the models of cluster "greater"; right: difference between clusters "greater" and "smaller" (δ). Stippling indicates areas where the multi-model ensemble mean response is significant (95% confidence interval). | 59 |
| 6.1 | Maps of annual, DJF and JJA average surface temperature (tas, left) and precipitation (right) difference between clusters "greater" and "smaller" (δ) for $\text{GWL} = +3\text{ }^\circ\text{C}$. Δ stands for anomalies relative to 1850-1950 mean. Stippling indicates areas where the multi-model ensemble mean response is significant (95% confidence interval). | 64 |
| 6.2 | Maps of annual, DJF and JJA average sea level pressure (SLP, left) and geopotential height at 500 hPa (Z_{500} , right) difference between clusters "greater" and "smaller" (δ) for $\text{GWL} = +3\text{ }^\circ\text{C}$. Δ stands for anomalies relative to 1850-1950 mean. Stippling indicates areas where the multi-model ensemble mean response is significant (95% confidence interval). | 70 |
| 6.3 | Historical average annual zonal-mean zonal wind (\bar{u}) computed from the models of both clusters. Positive (negative) values indicate eastward (westward) direction of the wind speed. | 74 |
| 6.4 | Average annual zonal-mean zonal wind (\bar{u}) anomalies relative to 1850-1950 mean (Δ) for $\text{GWL} = +3\text{ }^\circ\text{C}$. 6.4a: mean of the models of cluster "smaller"; 6.4b: mean of the models of cluster "greater"; 6.4c: difference between clusters "greater" and "smaller" (δ). In panels 6.4a and 6.4b, superimposed contours show the average historical annual zonal-mean wind speed computed from the models of the respective represented cluster; in panel 6.4c, contours show the average historical annual zonal-mean wind speed computed from the models of both clusters. Stippling indicates areas where the multi-model ensemble mean response is significant (95% confidence interval). | 75 |

| | | |
|-----|--|----|
| 6.5 | Average DJF zonal-mean zonal wind (\bar{u}) anomalies relative to 1850-1950 mean (Δ) for $\text{GWL} = +3$ °C. 6.5a: mean of the models of cluster "smaller"; 6.5b: mean of the models of cluster "greater"; 6.5c: difference between clusters "greater" and "smaller" (δ). In panels 6.5a and 6.5b, superimposed contours show the average historical DJF zonal-mean wind speed computed from the models of the respective represented cluster; in panel 6.5c, contours show the average historical DJF zonal-mean wind speed computed from the models of both clusters. Stippling indicates areas where the multi-model ensemble mean response is significant (95% confidence interval). | 76 |
| 6.6 | Northern Hemisphere maps (for latitudes north of 20° N) of 6.6a: DJF average zonal wind at 850 hPa (u850) difference between clusters "greater" and "smaller" (δ) for $\text{GWL} = +3$ °C. Δ stands for anomalies relative to 1850-1950 mean. Stippling indicates areas where the multi-model ensemble mean response is significant (95% confidence interval); 6.6b (from Zappa et al., 2018 [9]): late winter (JFM) CMIP5 mean response (10-model subset) in zonal wind at 850 hPa (u850, $m s^{-1}$) computed as difference between the RCP8.5 scenario and AMIPsst+co2. Stippling indicates areas where the response has the same sign in at least 90% of the models. | 78 |
| 6.7 | Average JJA zonal-mean zonal wind (\bar{u}) anomalies relative to 1850-1950 mean (Δ) for $\text{GWL} = +3$ °C. 6.7a: mean of the models of cluster "smaller"; 6.7b: mean of the models of cluster "greater"; 6.7c: difference between clusters "greater" and "smaller" (δ). In panels 6.7a and 6.7b, superimposed contours show the average historical JJA zonal-mean wind speed computed from the models of the respective represented cluster; in panel 6.7c, contours show the average historical JJA zonal-mean wind speed computed from the models of both clusters. Stippling indicates areas where the multi-model ensemble mean response is significant (95% confidence interval). | 79 |
| 6.8 | Historical average annual meridional mass streamfunction (MSF) computed from the models of both clusters. Positive (negative) values indicate air masses clockwise (anti-clockwise) rotation. | 80 |
| 6.9 | Average annual meridional mass streamfunction (MSF) anomalies relative to 1850-1950 mean (Δ) for $\text{GWL} = +3$ °C. 6.9a: mean of the models of cluster "smaller"; 6.9b: mean of the models of cluster "greater"; 6.9c: difference between clusters "greater" and "smaller" (δ). In panels 6.9a and 6.9b, superimposed contours show the average historical annual MSF computed from the models of the respective represented cluster; in panel 6.9c, contours show the average historical annual MSF computed from the models of both clusters (contour interval is $2 \times 10^{10} kg s^{-1}$). Stippling indicates areas where the multi-model ensemble mean response is significant (95% confidence interval). | 82 |

| | | |
|------|---|----|
| 6.10 | Average DJF meridional mass streamfunction (MSF) anomalies relative to 1850-1950 mean (Δ) for $\text{GWL} = +3$ °C. 6.10a: mean of the models of cluster "smaller"; 6.10b: mean of the models of cluster "greater"; 6.10c: difference between clusters "greater" and "smaller" (δ). In panels 6.10a and 6.10b, superimposed contours show the average historical DJF MSF computed from the models of the respective represented cluster; in panel 6.10c, contours show the average historical DJF MSF computed from the models of both clusters (contour interval is $2 \times 10^{10} \text{ kg s}^{-1}$). Stippling indicates areas where the multi-model ensemble mean response is significant (95% confidence interval). | 83 |
| 6.11 | Average JJA meridional mass streamfunction (MSF) anomalies relative to 1850-1950 mean (Δ) for $\text{GWL} = +3$ °C. 6.11a: mean of the models of cluster "smaller"; 6.11b: mean of the models of cluster "greater"; 6.11c: difference between clusters "greater" and "smaller" (δ). In panels 6.11a and 6.11b, superimposed contours show the average historical JJA MSF computed from the models of the respective represented cluster; in panel 6.11c, contours show the average historical JJA MSF computed from the models of both clusters (contour interval is $2 \times 10^{10} \text{ kg s}^{-1}$). Stippling indicates areas where the multi-model ensemble mean response is significant (95% confidence interval). | 85 |
| 6.12 | Map of DJF average NAO index difference between anomalies of clusters "greater" and "smaller" for $\text{GWL} = +3$ °C. Stippling indicates areas where the multi-model ensemble mean response is significant (95% confidence interval). | 88 |

List of Tables

| | | |
|-----|---|----|
| 3.1 | Models employed in this study, along with their horizontal and vertical resolution of both the atmosphere and ocean component. Resolution units are in (lat. degrees) \times (lon. degrees) \times (n° of vert. levels). Data retrieved from WCRP-CMIP, CMIP6 Controlled Vocabularies [10]. | 31 |
| 3.2 | SSP scenarios available, among those considered, for the models employed in this study. | 33 |
| 4.1 | Models belonging to the clusters of smaller and greater normalised NH sea ice decrease, along with their respective sensitivity value, in the SSP1-2.6 scenario. . . | 46 |
| 4.2 | Models belonging to the clusters of smaller and greater normalised NH sea ice decrease, along with their respective sensitivity value, in the SSP2-4.5 scenario. . . | 46 |
| 4.3 | Models belonging to the clusters of smaller and greater normalised NH sea ice decrease, along with their respective sensitivity value, in the SSP5-8.5 scenario. . . | 46 |
| 4.4 | List of the realisations of the model EC-Earth3 employed in the three scenarios for the test. | 47 |
| 4.5 | Year in which GWLs are reached in the models of the scenario SSP1-2.6, based on 21-year moving average filtered timeseries of GMT anomalies from 1850-1950 average. | 49 |
| 4.6 | Year in which GWLs are reached in the models of the scenario SSP2-4.5, based on 21-year moving average filtered timeseries of GMT anomalies from 1850-1950 average. | 50 |
| 4.7 | Year in which GWLs are reached in the models of the scenario SSP5-8.5, based on 21-year moving average filtered timeseries of GMT anomalies from 1850-1950 average. | 51 |

Chapter 1

Arctic sea ice cover: historical and current records

The focus of this work is on the impacts on global climate of sea ice decrease in the Northern Hemisphere, in particular in the Arctic Ocean. Therefore, this introductory chapter deals with the description of sea ice and its formation, the ways to physically quantify it and the past, current and projected future trends. The following chapter, instead, will address the main impacts and mechanisms through which sea ice interacts with the climate system, before going into the proper modelling analysis, core of the thesis.

1.1 Sea ice description

Sea ice is a floating mass which forms in the polar regions from freezing of seawater. Sea ice thickness is usually lower than 3 m and is further thickened by snow accumulation. Sea ice may consist of discontinuous pieces moved on the ocean surface by wind and currents (pack ice), or a motionless sheet attached to the coast or to ice shelves (fast ice). In particular, Arctic sea ice is the frozen interface between the ocean and atmosphere at the northern latitudes, limiting ocean-atmosphere exchanges of energy and moisture and playing a critical role in the Earth's climate and in the regional ecosystem.

In fact, Arctic sea ice cover is one of the key components of the polar climate system, since it is responsible for many crucial functions: from a more practical point of view, it aids or hinders human activities such as transportation and travel routes in the polar regions; it provides essential habitat for polar species like marine mammals, that depend on the ice as a platform for mating, feeding, birthing and other activities. It also supports the livelihoods of people in the Arctic (including indigenous peoples). From a global point of view, it regulates climate by reflecting solar radiation, it inhibits ocean-atmosphere exchange of heat, momentum and gases (including CO_2) and it supports global deep ocean circulation via dense (cold and salty) water formation [11]. Furthermore, the cycle of ice formation and melting influences food web dynamics and the biogeochemical balance of the upper ocean [4].

Sea ice drifts around the Arctic Ocean, forced by winds and ocean currents, growing and melting thermodynamically. Ice convergence can also lead to dynamic thickening (i.e., ridging and rafting), whereas when ice divergence occurs during winter, it exposes open water within which new ice can form. Thickness is strictly related to age, as multiyear ice (ice that survives at least one summer melt season) grows thicker over successive winter periods [4].

There has been growing attention on sea ice in recent years, largely because of a strong



Figure 1.1: *Chunks of sea ice, melt ponds and open water are all seen in this image captured at an altitude of 1500 feet (457 m) by the NASA’s Digital Mapping System instrument during an Operation IceBridge flight over the Chukchi Sea on Saturday, July 16, 2016. Credit: NASA’s Goddard Space Flight Center [1].*

decrease in the Arctic sea ice cover and modelling results that indicate that global warming could be amplified in the Arctic on account of the ice-albedo feedback. This results from the high reflectivity (albedo) of sea ice and overlying snow towards incoming solar radiation, which inhibits summer warming [2]. Sea ice albedo, in fact, is much higher than that of ice-free ocean waters, which are darker than ice and snow. This concept will be further analysed in the next chapter.

1.1.1 Quantities to define sea ice cover

In order to study sea ice patterns and evolution, three key quantities must be defined: sea ice concentration (the variable employed by climate models), sea ice extent and sea ice area. Sea ice concentration is the percent areal coverage of ice within the data element (i.e., the grid cell). Sea ice extent is the integral sum of the areas of all grid cells with at least 15% ice concentration, so the total area where ice is present, while sea ice area is the integral sum of the product of ice concentration and area of all grid cells with at least 15% ice concentration [2]. The extent is thus always greater than the area, but it also seems to be a little more stable from year-to-year, especially early in the records [12]. Extent is a common and useful metric to assess seasonal and long-term Arctic sea ice changes, for which now is available a 43-year record derived from consistent satellite-borne passive microwave sensor observations.

The seasonal cycle of Arctic sea ice is characterised by the maximum annual extent in March, decreasing through spring and summer to reach an annual minimum extent in September [4], as shown by the graphic in Fig. 1.2. Especially in summer, sea shows large temporal changes in ice extent. The substantial decline in Arctic ice extent since 1979 is one of the most iconic indicators of climate change.

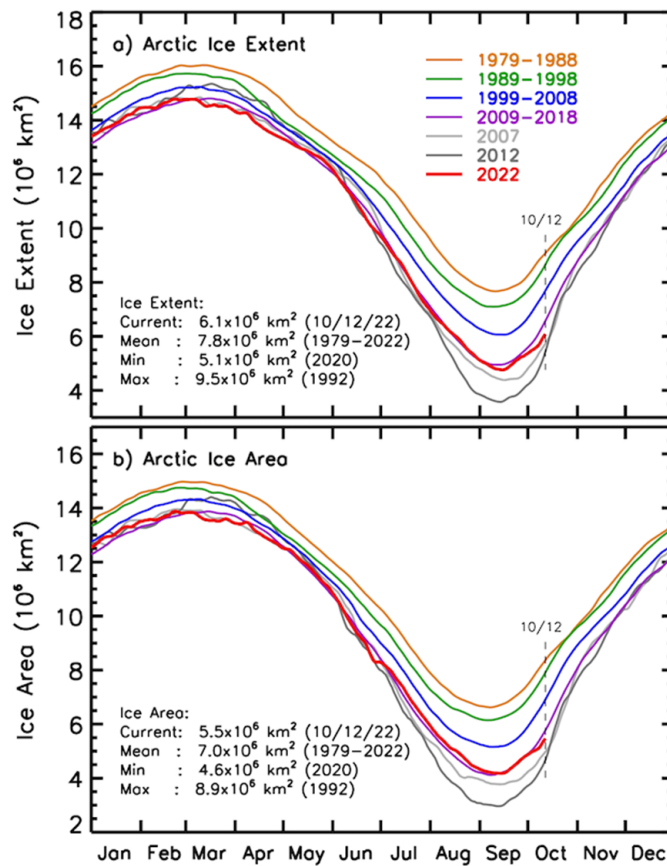


Figure 1.2: 10-year averages between 1979 and 2018 and yearly averages for 2007, 2012, and 2022 of the daily (a) ice extent and (b) ice area in the Northern Hemisphere and a listing of the extent and area of the current, historical mean, minimum, and maximum values in km^2 . The dashed vertical line indicates 12th October 2022 values. Credit: NASA’s Goddard Space Flight Center [2].

1.2 Historical records

Investigating the Arctic sea ice cover trends in the past is particularly challenging, since satellite-based data record started in the late 1970s. Therefore, other kinds of observations of differing accuracy must be considered if interested in time series prior to that year. In particular, Kinnard et al. (2008) [3], reconstructed time series of minimum (corresponding to September) and maximum (corresponding to March) ice extent for the period from 1870 to 2003, shown in Fig. 1.3.

The year-to-year variability of Arctic sea ice extent is fairly large. However, the composite historical record of Arctic ice margins shows that the maximum extent was relatively stable until the early 1960s, after which a gradual decline is observed. On the other hand, the minimum extent, which provides an order of magnitude of seasonal ice, is more variable on interannual to decadal timescales. However, a general retreat of seasonal ice can be recognised since about 1900; this declining trend, more pronounced than that of the maximum extent, started to accelerate in the same period as the March ice extent.

The most reliable observations are from 1979 onwards, corresponding to the modern satellite

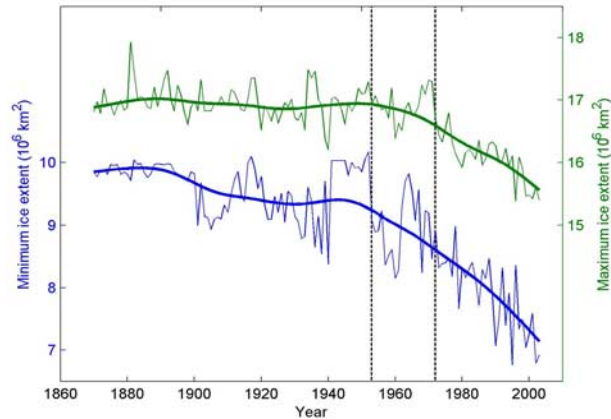


Figure 1.3: Total maximum (green) and minimum (blue) ice extent time series for the period 1870-2003. Thick lines are robust spline functions to highlight low-frequency changes. Vertical dotted lines separate the three periods for which data sources changed fundamentally: (1) 1870-1952: observations of varying accuracy/availability; (2) 1953-1971: generally accurate hemispheric observations; (3) 1972-2003: satellite period – best accuracy and coverage. Figure and caption from Kinnard et al., 2008 [3].

era. Patterns of ice-margin retreat may differ between different periods and regions of the Arctic, but the overall retreat trend is clearly larger than decadal-scale variability, as supported by observations and modelling of the 20th-century ice concentrations and water temperatures [13] [14] [15].

1.3 Trend in the last decades

Arctic sea ice is an expanse of frozen seawater floating on top of the Arctic Ocean and neighbouring seas. Every year, it expands and thickens during autumn and winter and grows smaller and thinner during spring and summer [16]. On the basis of satellite records, statistically significant negative trends in sea ice extent experienced in the last decades encompass all months, with the strongest trend in September [17], the month of minimum Arctic sea ice extent. Specifically, based on 1979-2018 satellite observations, September sea ice extent reductions are very likely $-12.8 \pm 2.3\%$ per decade relative to 1981-2010 mean (quantified in $-83000 \text{ km}^2/\text{year}$), while March is experiencing a reduction of $-2.7 \pm 0.5\%$ per decade in sea ice extent relative to the same reference period (corresponding to $-41000 \text{ km}^2/\text{year}$) [18]. Regionally, summer ice loss is dominated by reductions in the East Siberian Sea (which explains 22% of the September trend), and large declines in the Beaufort, Chukchi, Laptev and Kara seas [18]. Instead, winter ice loss is dominated by reductions within the Barents Sea, responsible for 27% of the pan-Arctic March sea ice trends [19]. Summer Arctic sea ice loss recorded since 1979 is unprecedented in 150 years based on historical reconstructions [20] and more than 1000 years based on palaeoclimate evidence [17] [21] [22].

As far as seasonality of sea ice is concerned, there is high confidence that the Arctic sea ice melt season has extended by 3 days per decade since 1979 due to earlier melt onset, and 7 days per decade due to later freeze-up [23]. This longer melt season is consistent with the observed loss of sea ice extent and thickness. Although the melt onset trends could seem small, they play a large role in the earlier development of open water [24] [25] and melt ponds [26], which enhance

the sea-ice-albedo feedback [27] [28]. Indeed, feedbacks from the loss of summer sea ice and spring snow cover on land have contributed to amplified warming in the Arctic region, where surface air temperature likely increased slightly more than three times faster than the rest of the world since 1970 [29]. The understanding of changes in Arctic sea ice is fundamental because these have potential to influence mid-latitude weather on timescales of weeks to months [11], as will be better discussed later on.

It has also been proved that Arctic sea ice cover, apart from shrinking, is also thinning rapidly [30] [31] [32] and therefore decreasing in volume [33]. Due to the mentioned relation between thickness and age, together with sea ice thinning, a transition to younger ice has taken place: between 1979 and 2018, the areal proportion of thick multi-year ice at least five years old has declined by approximately 90% (from 30% to 2%). Over the same period, first-year sea ice proportionally increased from approximately 40% to 60-70% [23]. The shift to thinner seasonal sea ice, in turn, contributes to further ice extent reductions through enhanced summer season melt via increased energy absorption [34].

Coming to the latest records, March and September 2021 total extent negative anomalies in the Arctic were not as extreme as in recent years, but still ranked among the lowest in the satellite record, far below the 1981-2010 average. In particular, March 2021 was characterised by lower-than-average extent in the Bering Sea, Baffin Bay, and the Gulf of St. Lawrence and near-normal extent elsewhere. September 2021 average extent was characterised by particularly lower-than-average coverage in the Siberian and East Greenland Seas and closer-to-normal coverage in the Beaufort and Chukchi Seas. The minimum extent reached in September 2021 was 4.72 million km², the 12th lowest value in 43 years of satellite records. However, the 15 lowest September extents in the satellite record have all occurred in the last 15 years [4]. The monthly average Arctic sea ice extent for March and September 2021, compared to their 1981-2010 mean, is represented in Fig. 1.4.

In the week before the 2021 annual minimum extent, when the age values of the remaining sea ice are incremented by one year, the amount of multiyear ice remaining in the Arctic Ocean was the second lowest on record (above only 2012). The September 2021 multiyear (of age between 1 and 4 years old) sea ice extent declined from 4.40 million km² in 1985 to 1.29 million km² in 2021. Over the same period, the oldest ice (> 4 years old) declined from 2.36 million km² to 0.14 million km² [4]. This suggests that in the Arctic, the contribution of multiyear ice more than 4 years old over the total sea ice is almost disappearing. Clearly, in the last decades, the Arctic Ocean has changed from a domain dominated by multiyear ice to one where first-year ice prevails. As already stated, younger ice cover implies a thinner, less voluminous ice pack.

The satellite-based data record started in late 1978 shows unequivocally that rapid changes have been occurring in the Arctic, where the ice coverage has been declining at a substantial rate. The pan-Arctic loss of sea ice cover is a prominent indicator of climate change. In contrast, in the Antarctic, which isn't of direct interest for this study, the sea ice coverage has been increasing in all seasons from 1979 on, although at a lesser rate than the decreases in the Arctic [2]. Anyway, the trend in Antarctic sea ice extent is overall not statistically significant in the period 1979-2018, due to contrasting regional signals and large interannual variability [11].

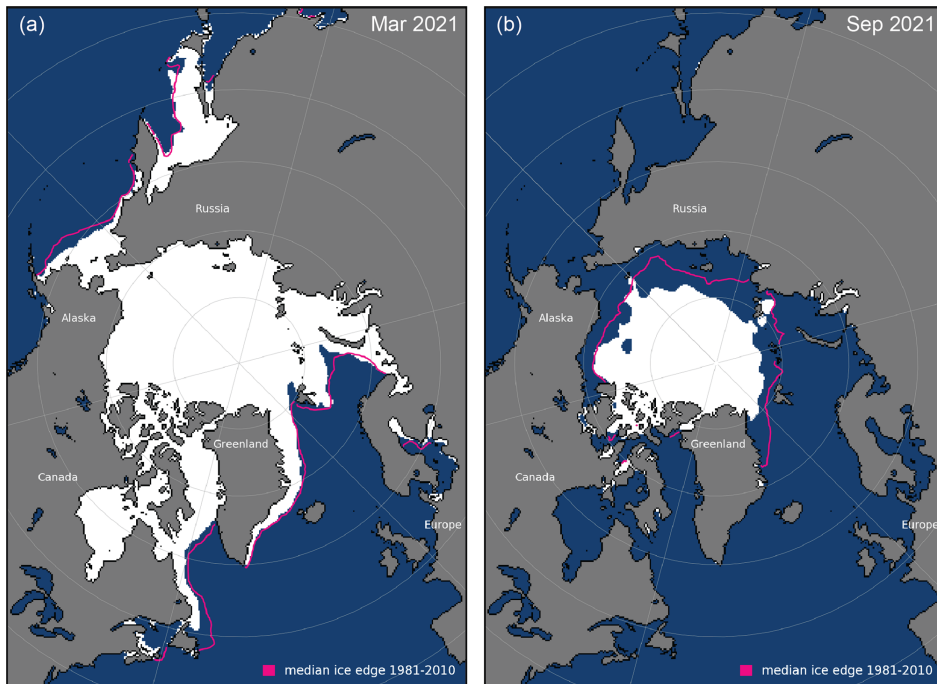


Figure 1.4: Monthly average sea ice extent for (a) March 2021, and (b) September 2021. The median extent for 1981-2010 is shown by the magenta contour. Figure and caption from Meier et al., 2021 [4].

1.4 Future projections

After analysing what has been retrieved as for the historical sea ice cover and how it has evolved over the last few decades up to nowadays, this section provides an overview of the projection of Arctic sea ice trends until the end of the century, although a description of sea ice modelling will be given in later chapters.

Current models vary greatly in their future projections of sea ice. Basically, greenhouse gas emissions will determine the impact on sea ice from man-made climate change through radiative forcing (i.e., Representative Concentration Pathways or RCPs), as will be better explained. However, the dramatic Arctic sea ice reduction is projected to continue through mid-century, with differences thereafter depending on the magnitude of global warming: for stabilised global warming of 1.5 °C, the annual probability of a sea-ice-free September by the end of century is approximately 1%, which rises to 10-35% for stabilised global warming of 2 °C [35].

Fig. 1.5 shows the projected future trends of Northern Hemisphere September sea ice extent according to the main four CMIP5 emission scenarios until 2100. Projections for RCP2.6 – one of the most optimistic scenarios – show that reduced greenhouse gas emissions will lead to a stabilization of Arctic sea ice area over the 21st century. For all the other scenarios, it is very likely that there will be further shrinking and thinning of Arctic sea ice cover year-round as global mean surface temperature rises. Some climate projections exhibit 5- to 10-year periods of sharp summer Arctic sea ice decline, even steeper than observed over the last decade. The CMIP5 multi-model projections foresee average reductions in Arctic sea ice extent for 2081-2100 compared to 1986-2005 ranging from 8% for RCP2.6 to 34% for RCP8.5 – the scenario with the highest emission

levels – in February and from 43% for RCP2.6 to 94% for RCP8.5 in September [5]. This confirms that the steepest decreasing trend will affect the month with the lowest extent rather than the winter ones. CMIP5 models that produce the most realistic recent-years sea ice conditions (i.e., the 1979-2012 trend) predict a nearly ice-free Arctic Ocean (sea ice extent lower than 10^6 km² for at least five consecutive years) in September around mid-century under the RCP8.5 scenario. A similar projection arises for RCP6.0, whereas the Arctic would be practically ice-free towards the end of the century under the intermediate GHG emission scenario RCP4.5. According to the most recent CMIP6 models, the annual Arctic sea ice area minimum will likely fall below 1 million km² at least once before 2050 under all assessed SSP scenarios. Even under SSP5-8.5 – the highest emission scenario in CMIP6 – the Arctic is projected to become practically sea ice-free in September around mid-century. In general, CMIP6 models better simulate the sensitivity of Arctic sea ice area to anthropogenic CO₂ emissions, thus they better capture the time evolution of the satellite-observed Arctic sea ice loss [36].

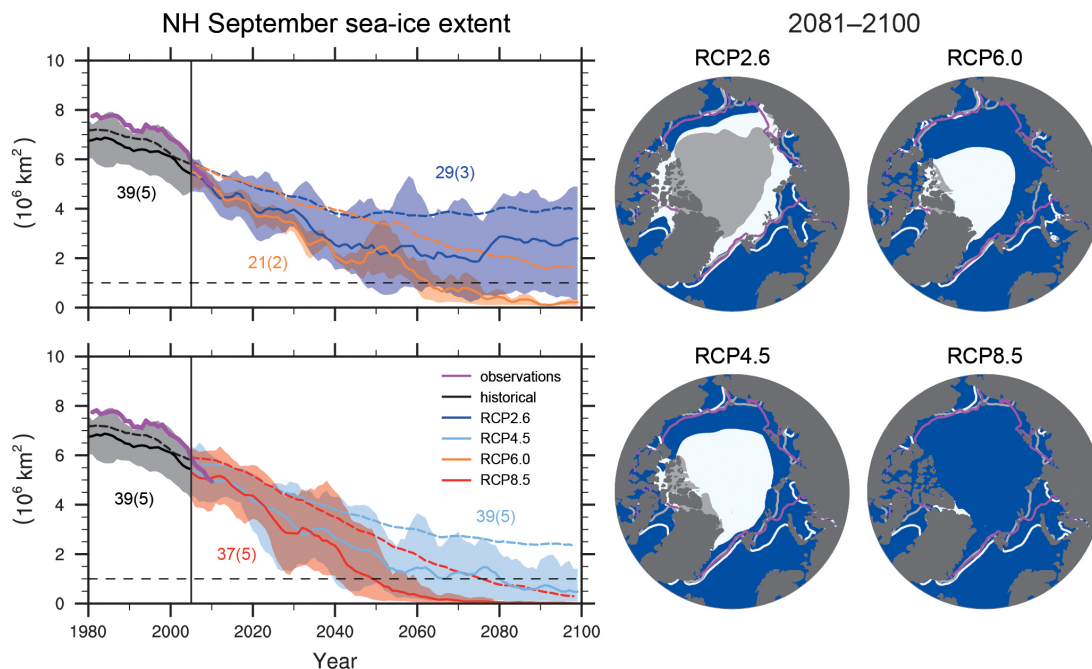


Figure 1.5: Northern Hemisphere (NH) sea ice extent in September over the late 20th century and the whole 21st century for the scenarios RCP2.6, RCP4.5, RCP6.0 and RCP8.5 in the CMIP5 models, and corresponding maps of multi-model results in 2081-2100 of NH September sea ice extent. In the time series, the number of CMIP5 models to calculate the multi-model mean is indicated (subset in brackets). Time series are given as 5-year running means. The projected mean sea ice extent of a subset of models that most closely reproduce the climatological mean state and 1979-2012 trend of the Arctic sea ice is given (solid lines), with the minimum to maximum range of the subset indicated with shading. Black (grey shading) is the modelled historical evolution using historical reconstructed forcings. The CMIP5 multi-model mean is indicated with dashed lines. In the maps, the CMIP5 multi-model mean is given in white and the results for the subset in grey. Filled areas mark the averages over the 2081-2100 period, lines mark the sea ice extent averaged over the 1986-2005 period. The observed sea ice extent is given in pink as a time series and averaged over 1986-2005 as a pink line in the map. Figure and caption from IPCC (2013), Assessment Report 5, Working Group I, Technical Summary, Fig. TS.17 [5].

However, there is little evidence in global climate models of a tipping point (or critical threshold) in the transition from a perennially ice-covered to a seasonally ice-free Arctic Ocean beyond which further sea ice loss is unstoppable and irreversible [5]. A situation of this kind would be excluded primarily because of the linearity of the correlation between Arctic summer sea ice loss and rising global mean surface temperature [36].

Reduced seasonal sea ice extent and continued loss of multi-year sea ice, together with warming and ocean acidification, are projected to impact polar marine ecosystems through direct and indirect effects on habitats, populations and their viability [35].

Chapter 2

Motivation: the impact of sea ice reduction

The last chapter was devoted to the characterisation of sea ice and its evolution over time; the focus of the thesis will be on the consequences of the well-established reduction in Arctic sea ice on the climate system. Therefore, herein the scientific problem at the basis of the work is exposed, starting from the role that sea ice plays in regulating global climate.

Sea ice is a fundamental component of the Earth's climate system and changes in its abundance have important implications for global weather and climate, as well as for polar ecosystems and other more practical aspects relevant to trade and economy [37]. Some aspects through which it regulates the climate were already mentioned previously: by reflecting solar radiation, by inhibiting ocean-atmosphere exchange of heat, momentum and gases (including CO_2) and by supporting global deep ocean circulation via dense (cold and salty) water formation [11]. The first cited one is probably the most impactful factor, and occurs because of the high albedo of ice and snow that covers it. The surface albedo, α_s , is defined as the fraction of the downward solar flux density that is reflected by the surface. The surface albedo varies widely depending on the surface type and condition, ranging from values as low as 5% for oceans under light winds to as much as 90% for fresh, dry snow [38]. Based on satellite measurements, the average Earth's albedo is 29%. As for sea ice, if not covered by snow, the albedo can range between 25% and 40%, with a typical value of 30%, while typical albedo values for snow covering sea ice are 50% if the snow is old and melting, 70% for dry, cold snow and 80% for fresh and dry snow. On the other hand, deep ocean water has typical albedo values of 7% and 12%, respectively if under low or high wind conditions [38]. From the definition of surface albedo it is clear that if sea ice cover melts and is therefore replaced by dark ocean, having an extremely lower albedo, much lower radiation energy is reflected by that surface. In fact, the decreased sea ice cover would reduce the albedo and increase the amount of solar energy absorbed by the planet. This increase in solar energy absorption would cause further warming and thus further ice shrinking that might ultimately lead to an ice-free ocean. The association of ice melting with higher temperatures can constitute a very powerful positive feedback – called *ice-albedo feedback* – since it modulates the direct energy input from the Sun [38]. A feedback mechanism is a process that changes the sensitivity of the climate response, so the relationship between the measure of forcing – a perturbation to the climate system that can be expected to change the climate – and the magnitude of the climate change response. In other words, a feedback can amplify or dampen the mechanism of a given forcing; the output of a certain process acts to modify the input of the process itself, creating a feedback loop. Climate forcings are usually quantified in terms of how many $W m^{-2}$ they change the energy balance

of the Earth when imposed. Assuming linearity in the response, if some radiative forcing R is applied to the climate system, its relation with the global mean surface temperature response is the following

$$R = -\lambda\Delta T_s \quad (2.1)$$

where ΔT_s is the change in equilibrium temperature, that is, the change in temperature through which the climate system reaches a new equilibrium. λ is the climate feedback parameter, which in the case of ice-albedo is quantified as $0.3 \pm 0.1 \text{ W m}^{-2} \text{ K}^{-1}$ [38]. The ice-albedo feedback is a positive feedback because its process increases the magnitude of the response.

The feedback just described is at the basis of the so called “polar amplification”, namely the fact that the poles warm up much rapidly and more than lower latitudes. In fact, Arctic surface air temperature has likely increased by more than double the global average over the last two decades [11]. During the period 2014-2018, Arctic annual surface air temperature exceeded that of any year since 1900. During the winters (January to March) of 2016 and 2018, surface temperatures in the central Arctic Ocean were 6 °C above the 1981-2010 average, contributing to unprecedented regional sea ice absence. In summer months, over large sectors of the seasonally ice-free Arctic, upper oceanic mixed layer temperatures increased at around 0.5 °C per decade during 1982-2017, primarily due to increased absorbed solar radiation accompanying sea ice loss; moreover, the inflow of ocean heat from lower latitudes increased since the 2000s [11].

There is growing observational evidence that suggests ongoing reductions of Arctic sea ice may be impacting various aspects of weather and climate, both locally in the Arctic and remotely in the Northern Hemisphere mid latitudes. As a matter of fact, because of the albedo effect if the amount of Arctic sea ice decreases, the Arctic starts warming up, and at that point the circulation of the jet stream, which brings weather to the mid latitudes, begins to change [16].

In this thesis, the research question is to investigate which changes in the climate are associated to the projected changes in Arctic sea ice cover, apart from the obvious variation in polar temperature, for which the polar amplification effect is responsible. The key challenge for achieving the determination of the effects of sea ice decrease itself is therefore to avoid, as far as possible, the tight correlation existing between the variation in sea ice cover and the global temperature change, due to the very important ice-albedo feedback, at the basis of polar amplification. To implement this isolation of the effects of Arctic sea ice decline itself, the procedure explained in the chapter 3 is followed. The work will focus on the effects on Northern Hemisphere and more widely on global climate, investigating also the atmospheric circulation: will be analysed patterns of temperatures, precipitation, zonal winds, pressure and geopotential height, and the North Atlantic Oscillation (NAO).

2.1 Literature review on the topic

Among the climate science, the topic of Arctic sea ice impacts on the climate has not been developed extensively as others in scientific literature. However, several publications on the subject have been produced in the last 10-15 years. A review of the literature on the matter of this thesis is useful under different aspects: first of all, it provides an overview of what has already been analysed and therefore can guide on the most critical aspects; then, in a next stage, it can be of

help to compare the results obtained, in order to verify if they agree with previous studies.

Most of the publications addressing the impacts of sea ice cover loss on the climate analyse the effects on the atmospheric circulation: in fact, due to the changes in polar temperatures enhanced by the polar amplification, the temperature gradient between the equator and the poles varies, and so the intensity and the position of the jet streams. For this reason, also the energy transports between the equator and the poles change, having a direct impact on the atmospheric circulation.

To mention some examples, the dwindling Arctic ice cover has been cited as a cause of recent changes in Arctic air temperature and humidity [39] [40] [41] [32], storm activity [42] and tropospheric circulation patterns [43] [44] [45] [46], as well as in trends in Siberian snow cover [47] and in the occurrence of Eurasian cold winters [48] [49] [50]. This last aspect has been extensively studied by the scientific community in the last decade: the loss of Arctic sea ice has been identified responsible for the weakening of mid-latitude westerlies, thus promoting more severe cold winters on Eurasia and mid latitudes. Most of this research has found support from observations [51] [52] [50] [53] [54] [55] [56]; other papers have found confirmation of this in model simulations [48] [49] [50] [57] [58], although most recent publications argued that the effect of mid-latitude winter cooling caused by sea ice decrease is weak [59] [60] [61]. It is important to note that all these studies looked at the seasonal scale, in particular they focused on the winter response; as these, many other studies, even if not centred on winter cooling on mid latitudes, analysed the seasonal response of the climate to sea ice loss. For instance, Cheung et al. (2022) assessed the influence of Arctic sea ice cover on the uncertainties, interpreted as inter-model spread, in future projections of the boreal winter climate [62]; Nakamura et al. (2019) found enhanced negative Arctic Oscillation-like anomalies in the winters following sea ice decrease, triggered by memory effects in the snow amount and soil temperature fields [63]. Screen et al. (2013) proposed a rather complete picture of the atmospheric response to observed sea ice loss: they detected increased energy transfer from the ocean to the atmosphere, enhanced warming and moistening of the lower troposphere, decreased strength of the surface temperature inversion and increased lower tropospheric thickness, all changes more pronounced in autumn and early winter (September–December). They also looked for atmospheric temperature responses and associated changes in lower atmospheric stability, humidity, cloud cover, precipitation responses, tropospheric circulation responses, as well as impacts of sea ice loss on the stratosphere [37]. Petrie et al. (2015) analysed the atmospheric circulation response in summer to Arctic sea ice loss, temperature anomalies and sea level pressure [64]. In general, it arises that most of the impacts of Arctic sea ice loss are confined to the lower troposphere [37]. It is also relevant to point out that every cited publication examined the influence of Arctic sea ice cover reduction on Northern Hemisphere: some on Europe, others on Eurasia, on northern or mid latitudes, on the North Atlantic sector or on the whole Northern Hemisphere.

As far as the methods are concerned, the cited works followed different approaches: most of them employed Atmospheric General Circulation Models (AGCMs) with prescribed sea surface temperatures and sea ice data, retrieved from observations [59] [49] [64] [63] [37], thus evaluating the impacts of sea ice loss occurred in recent decades. On the other hand, Cheung et al. (2022) and Koenigk et al. (2019) made use of coupled models following the RCP8.5 scenario [62] [57], as well as Yang et al. (2012), who considered also the RCP4.5 scenario [58]; therefore, they identified the impacts of sea ice decline from future climate projections. Smith et al. (2022) did the same

by adopting models from the Polar Amplification Model Intercomparison Project (PAMIP) [61]; finally, Petrie et al. (2015) analysed also reanalysis products – full 3D weather models forced, through a mathematical technique called “data assimilation”, to stay close to observations – in order to compare them with the climate model experiments they performed [64]. Of those who looked at the impacts of sea ice on the future climate, just Smith et al. (2022) (the most recent of the cited studies) employed the sixth Coupled Model Intercomparison Project (CMIP6), while the others used CMIP5, which is the previous generation of models.

The results of several of the papers cited in this section will be compared with our results where useful in the next chapters.

Chapter 3

Methodology

This chapter presents an overview of the method adopted in the study, that will be then thoroughly described step by step starting from the next chapter. It is very challenging to unambiguously assign causality and to separate the influences of multiple interconnected processes in the climate system, especially if using observations or atmospheric reanalyses alone. Formal attribution and quantification of changes to Arctic sea ice loss and of linkages between different climatic processes requires a different approach [37]. This study doesn't employ General Circulation Models forced by sea ice data, nor observation or reanalysis data, but is based on future climate projections from coupled models belonging to the CMIP6 framework, the most recent generation of models. The models, that initially had different grid resolutions, are all interpolated on a common fine $0.5^\circ \times 0.5^\circ$ grid.

The research question from which the work arises is to detect and understand the variations on the projected future climate attributable to the shrinking of sea ice cover, apart from the expected increase in polar temperatures, caused by the polar amplification effect. The fundamental point is indeed to leave apart as much as possible the correlation existing between the change in sea ice cover and that in global temperatures, so the dominance of the ice-albedo effect in the Arctic domain. In other words, this means isolating the response of the climate to Arctic sea ice exclusively, separately from the connection to rising temperatures. Afterwards, the interest will be in the impact on temperature patterns and on several other climate variables.

In order to isolate the response to sea ice changes alone, we consider the difference in sensitivity of sea ice cover changes compared to the temperature variation. To do so, first a difference in sea ice cover surface (for simplicity referred to as *sea ice*) is defined between two relevant periods. In fact, since the interest is in the future variations, a historical reference period is taken as 1850-1950, and a future period is considered as 2070-2099 based on models projections: the difference between the mean of the end-of-century sea ice cover and the historical one constitutes the $\Delta_{sea-ice}$. As far as the future projections are concerned, three relevant scenarios are taken into account: SSP1-2.6, SSP2-4.5, SSP5-8.5 (see paragraph 3.1.2). The sensitivity of sea ice changes in regard to temperature variation is retrieved by dividing $\Delta_{sea-ice}$ by a difference in global mean surface temperatures between the same two periods, called Δ_{GMT} .

Different models have different sensitivities, assessed through the distribution of the normalised sea ice cover difference, $\frac{\Delta_{sea-ice}}{\Delta_{GMT}}$. These distributions – one for each scenario considered – are visualised through scatter plots, from which it is possible to evaluate the correlation between temperature variations and sea ice variations in every model. Based on this parameter, the

models are grouped in clusters corresponding to the upper and lower terciles of the distribution. Those represent respectively the models that, being the global mean temperature variation from past to future equal, foresee a greater and smaller change in sea ice cover surface.

Then the analysis is conducted at different levels of global mean temperature warming: four global warming levels (GWLs) are defined at +1, +2, +3 and +4 °C relative to the historical baseline (1850-1950). For each model, the year in which a given GWL is reached is identified in the global surface temperature timeseries, filtered with a 21-year moving average. Clearly, not all of the three scenarios reach all four levels of global warming.

Once defined the GWLs, the climate variables of interest are plotted on maps where their differences are represented between the mean of 21 years centred on the year in which a certain GWL is attained and the mean of the historical period. This procedure is applied for all the models belonging to the clusters defined previously. Next, the models belonging to the clusters with smaller normalised sea ice area defined before for the three SSPs are put together independently from the scenario, as the models belonging to all the clusters with greater normalised sea ice area. This is possible thanks to the definition of global warming level; in this way two ensemble of models are created. Then, the maps of the climate variables analysed, plotted individually for each model, are averaged together within the upper and lower clusters, to have a picture of the average change in the variable in the models that project a smaller and a greater sea ice loss when reaching a threshold of global warming. The procedure described allows us to detect the impacts of different future patterns of Arctic sea ice on the climate, aside from the differences in global mean temperature, which is set equal. In any variable studied, to better visualise the impacts due to changes in Arctic sea ice cover, the difference between the maps of the two clusters is plotted too. In this last map, stippling shows statistical significance of the results.

The goodness and effectiveness of the methodology applied is corroborated by several statistical tests, both for the identification of the clusters of models and the choice of working with global warming levels, as will be pointed out. One important difference between this study and the ones presented in the previous paragraph is that many of those are focused on the seasonal impacts of Arctic sea ice reduction, mostly winter ones, while this work aims to find impacts principally on an annual timescale, meaning independently from the season. In fact, the originally monthly model data are averaged yearly. However, for many variables linked to the atmospheric circulation it is useful to look at variations in the seasonal patterns, and those are analysed. Furthermore, all the cited articles look for impacts on the Northern Hemisphere and mainly its mid latitudes, not global ones; this study, as anticipated, seeks global, large-scale responses to the decrease of Arctic sea ice on the climate. The usefulness of this choice, which constitutes an element of novelty of the work, lies in the global scale of the atmospheric circulation, whose domain has no strict boundaries.

As anticipated, apart from sea ice cover and temperature, the variables investigated and mapped are precipitation, zonal winds and mass streamfunction, sea level pressure and geopotential height. Moreover, an analysis using the Empirical Orthogonal Function (EOF) is carried out, in order to detect variations in the mean patterns of large-scale variability, in particular in the North Atlantic Oscillation (NAO).

3.1 Climate models

All the analyses implemented in this study are carried out through the manipulation of climate data relative to several climate variables. These are simulated by climate models; therefore, it is important to dedicate this section to the explanation and the description of such an essential part of the study.

Climate models are numerical representations of the Earth’s climate system that allow the understanding of climate and predicting its future variations. They are mathematical models which incorporate the principles of physics, chemistry, and biology; several types of climate models exist and can be subdivided based on the level of complexity with which they represent these principles. They range from simple energy-balance models, that can be solved through manual calculations, to very complex models that employ the most sophisticated numerical techniques and require fast supercomputers to generate their outputs. The ones adopted in this study are among the most complex global climate models, that can produce the most realistic simulations of climate and on which we rely for predicting future climates in sufficient detail to be useful for planning purposes. For our aims, these models are also useful for understanding the climate system and how various processes interact to determine the structure that climate change will take, in order to support attribution of forecast changes to specific forcings. In particular, all the models adopted belong to the “GCM” category (acronym for global climate model), sometimes also referred to as atmosphere–ocean general circulation model (AOGCM), since in these the fluid motions of both atmosphere and ocean are explicitly calculated [65]. GCMs typically simulate the atmosphere, ocean, sea ice, and land surface, and sometimes also incorporate terrestrial and marine ecosystems. GCMs describe the climate applying a three-dimensional grid on the globe; models may differ in their horizontal and vertical resolution and grid type, and in the extent to which processes are explicitly represented or approximated (parameterised) [11]. The physical processes of the climate system are described by differential equations (converted to computer codes), that are solved giving as output the climate variables characterizing each box at each timestep. In other words, external radiative forcings are prescribed in GCMs as boundary conditions; then, GCMs use a model of the physical climate system to compute the response of the climate [65]. Fig. 3.1 illustrates a schematic example of the way the Earth is numerically rendered in a GCM through grid cells and the most important climate processes represented.

Every global climate model is made up of different components, that can be seen as proper “sub-models”. They follow the three primary physical components of the climate system: the atmosphere, the ocean, and the land surface. The cryosphere is split between the oceans, where sea ice plays an important role, and the land surface, where snow, glaciers, and ice sheets may form. In most climate models, at least a thermodynamic model of sea ice is employed. As previously explained, there are many processes through which sea ice interacts with other elements of the climate system: it increases the albedo of the ocean surface, inhibits the exchanges of heat, moisture and momentum between atmosphere and ocean, alters the local salinity during freezing and melting phases and so on. Schematically, sea ice role can be split in thermodynamic processes, leading to freezing and melting of seawater, and dynamic processes, such as driving by winds and currents, which cause mechanical deformation and transport of sea ice. For instance, transport of sea ice by winds and currents is treated with varying degrees of complexity by GCMs, ranging from

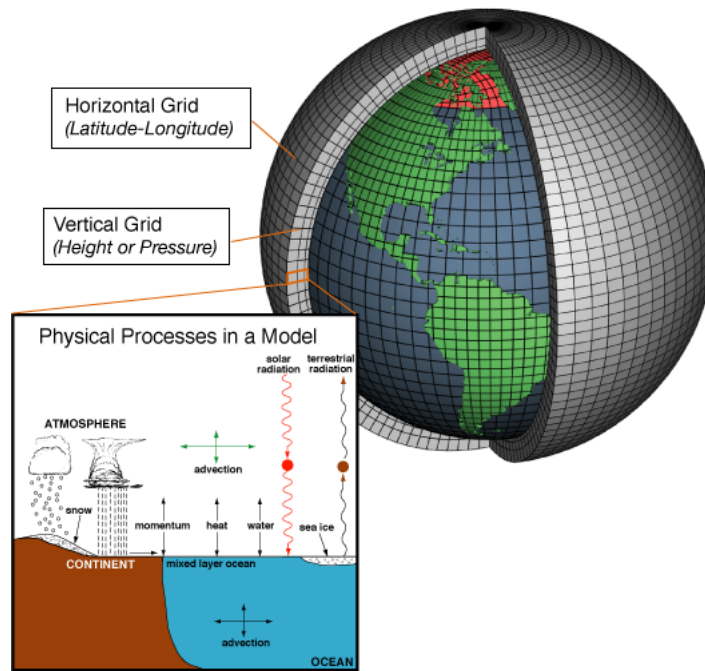


Figure 3.1: Schematic representation of the functioning of a Global Climate Model. Credit: National Oceanic and Atmospheric Administration (NOAA) [6].

mixed-layer ocean models with no ice transport at all, to more complete models that calculate the movement of ice in response to both winds and currents [65]. Also the effect of ice-albedo feedback is included in climate models, since they simulate land snow cover and sea ice on a seasonal basis. Models, by construction, have different climate sensitivities, meaning that they are sensitive in a different way to climate forcings, so have a different climate change response to the same forcing. This is the so called *inter-model uncertainty*, which translates for instance in a distinct representation of the ice-albedo feedback in the models, reason why their projections vary considerably, as it will be shown.

3.1.1 CMIP6 models employed

A process for conducting coordinated climate modelling experiments and sharing simulation data has been endorsed and organised by the World Climate Research Programme (WCRP) under the name of Coupled Model Intercomparison Project (CMIP). CMIP started in 1995 and involves multiple international modelling teams to analyse, share and compare state-of-the-art climate model simulations to gain insights into the processes, mechanisms, and consequences of climate variability and climate change. Another aim of the project is to better understand past, present and future climate change in a multi-model context, by coordinating the design and distribution of global climate model simulations [67]. CMIP climate modelling experiments are coordinated, since a common set of forcings and boundary conditions has been prescribed for climate simulations, although models can vary heavily in the way they implement them. These concern land and vegetation, anthropogenic and natural aerosols, volcanic aerosols, greenhouse gases and solar forcing. Thus, it is possible to perform multi-model ensemble analyses, which are demonstrated

Table 3.1: Models employed in this study, along with their horizontal and vertical resolution of both the atmosphere and ocean component. Resolution units are in (lat. degrees) \times (lon. degrees) \times (n° of vert. levels). Data retrieved from WCRP-CMIP, CMIP6 Controlled Vocabularies [10].

| No. | Model | Institute | Atmosphere resolution | Ocean resolution |
|-----|------------------|--|--|---|
| 1. | ACCESS-CM2 | CSIRO, ARCCSS, Australia | $1.25^\circ \times 1.88^\circ \times 85$ | $1.00^\circ \times 1.00^\circ \times 50$ |
| 2. | ACCESS-ESM1-5 | CSIRO, Australia | $1.24^\circ \times 1.88^\circ \times 38$ | $1.00^\circ \times 1.00^\circ \times 50$ |
| 3. | BCC-CSM2-MR | BCC, China | $1.13^\circ \times 1.13^\circ \times 46$ | $1.00^\circ \times 1.00^\circ \times 40$ |
| 4. | CAMS-CSM1-0 | CAMS, China | $1.13^\circ \times 1.13^\circ \times 31$ | $1.00^\circ \times 1.00^\circ \times 50$ |
| 5. | CanESM5 | CCCma, Canada | $2.81^\circ \times 2.81^\circ \times 49$ | $1.00^\circ \times 1.00^\circ \times 45$ |
| 6. | CAS-ESM2-0 | CAS, China | $1.41^\circ \times 1.41^\circ \times 35$ | $1.00^\circ \times 1.00^\circ \times 30$ |
| 7. | CESM2-WACCM | NCAR, USA | $0.94^\circ \times 1.25^\circ \times 70$ | $1.00^\circ \times 1.00^\circ \times 60$ |
| 8. | CIESM | THU, China | $0.94^\circ \times 1.25^\circ \times 30$ | $0.50^\circ \times 0.50^\circ \times 46$ |
| 9. | CMCC-CM2-SR5 | CMCC, Italy | $0.94^\circ \times 1.25^\circ \times 30$ | $1.00^\circ \times 1.00^\circ \times 50$ |
| 10. | CMCC-ESM2 | | $0.94^\circ \times 1.25^\circ \times 30$ | $1.00^\circ \times 1.00^\circ \times 50$ |
| 11. | E3SM-1-1 | E3SM-Project, RUBISCO, USA | $1.00^\circ \times 1.00^\circ \times 72$ | variable [66], 60 |
| 12. | EC-Earth3 | EC-Earth Consortium, Europe | $0.70^\circ \times 0.70^\circ \times 91$ | $1.00^\circ \times 1.00^\circ \times 75$ |
| 13. | EC-Earth3-CC | | $0.70^\circ \times 0.70^\circ \times 91$ | $1.00^\circ \times 1.00^\circ \times 75$ |
| 14. | EC-Earth3-Veg | | $0.70^\circ \times 0.70^\circ \times 91$ | $1.00^\circ \times 1.00^\circ \times 75$ |
| 15. | EC-Earth3-Veg-LR | | $1.13^\circ \times 1.13^\circ \times 62$ | $1.00^\circ \times 1.00^\circ \times 75$ |
| 16. | FGOALS-f3-L | | CAS, China | $1.00^\circ \times 1.25^\circ \times 32$ |
| 17. | FGOALS-g3 | $2.25^\circ \times 2.00^\circ \times 26$ | | $1.00^\circ \times 1.00^\circ \times 30$ |
| 18. | FIO-ESM-2-0 | FIO, QLNLM, China | $0.94^\circ \times 1.25^\circ \times 26$ | $0.27-0.54^\circ \times 1.10^\circ \times 60$ |
| 19. | GFDL-CM4 | NOAA-GFDL, USA | $1.00^\circ \times 1.25^\circ \times 33$ | $0.25^\circ \times 0.25^\circ \times 75$ |
| 20. | GFDL-ESM4 | | $1.00^\circ \times 1.25^\circ \times 49$ | $0.50^\circ \times 0.50^\circ \times 75$ |
| 21. | INM-CM4-8 | INM, Russia | $1.50^\circ \times 2.00^\circ \times 21$ | $0.50^\circ \times 1.00^\circ \times 40$ |
| 22. | INM-CM5-0 | | $1.50^\circ \times 2.00^\circ \times 73$ | $0.25^\circ \times 0.50^\circ \times 40$ |
| 23. | IPSL-CM5A2-INCA | IPSL, France | $1.88^\circ \times 3.75^\circ \times 39$ | $2.00^\circ \times 2.00^\circ \times 31$ |
| 24. | IPSL-CM6A-LR | | $1.27^\circ \times 2.50^\circ \times 79$ | $1.00^\circ \times 1.00^\circ \times 75$ |
| 25. | MIROC6 | MIROC Consortium, Japan | $1.41^\circ \times 1.41^\circ \times 81$ | $1.00^\circ \times 1.00^\circ \times 63$ |
| 26. | MPI-ESM1-2-HR | MPI-M, DWD, DKRZ, Germany | $0.94^\circ \times 0.94^\circ \times 95$ | $0.40^\circ \times 0.40^\circ \times 40$ |
| 27. | MPI-ESM1-2-LR | MPI-M, AWI, DKRZ, DWD, Germany | $1.88^\circ \times 1.88^\circ \times 47$ | $1.50^\circ \times 1.50^\circ \times 40$ |
| 28. | MRI-ESM2-0 | MRI, Japan | $1.12^\circ \times 1.13^\circ \times 80$ | $0.50^\circ \times 1.00^\circ \times 61$ |
| 29. | NESM3 | NUIST, China | $1.88^\circ \times 1.88^\circ \times 47$ | $1.00^\circ \times 1.00^\circ \times 46$ |
| 30. | NorESM2-LM | NCC, Norway | $1.88^\circ \times 2.50^\circ \times 32$ | $1.00^\circ \times 1.00^\circ \times 53$ |
| 31. | NorESM2-MM | | $0.94^\circ \times 1.25^\circ \times 32$ | $1.00^\circ \times 1.00^\circ \times 53$ |
| 32. | TaiESM1 | AS-RCEC, Taiwan | $0.94^\circ \times 1.25^\circ \times 30$ | $1.00^\circ \times 1.00^\circ \times 60$ |

to increase the reliability and consistency of the model projections [68]. Due to their fundamental importance in the framework of climate science, CMIP model experiments have routinely been the basis for future climate change assessments made by the IPCC, lastly in the 6th Assessment Report (AR6).

The 6th and most recent phase of the CMIP is called CMIP6 and its models support the statements of IPCC AR6, published in three contributions from August 2021 to April 2022. Around 130 global climate model runs produced by 49 different modelling teams compose the CMIP6, which encompasses a very large number of experiments [69]. As all the other phases of CMIP, it includes both historical and future climate simulations: the historical time frame was defined to span the period between 1850 and 2014. Table 3.1 lists all the models employed in this study, along with their spatial resolution both of the atmospheric and oceanic component. Please note that the reported ocean resolution is the nominal one: in fact, most of the models make use of an irregular grid for the ocean component, usually changing resolution with latitude.

The choice of the models to adopt was made primarily based on the availability and completeness of sea ice concentration data in the past and in future projections. A relatively large number of models is necessary in order to provide robustness to the results. As can be noticed from data in the table, every model differs in horizontal and vertical resolution of its grids: therefore, they were all re-gridded using a $0.5^\circ \times 0.5^\circ$ resolution. As far as of the models' realisations are concerned – ensembles of experiments performed with the same model – for all the models the same one was used, called “r1i1p1f1”, except for a test analysis carried out during the definition of the clusters of models based on sea ice cover projections, as will be later specified.

3.1.2 SSP scenarios

It is very important to predict how climate will change in the future for several reasons, among which especially for planning actions to limit the impact of climate change on the natural and built environment (adaptation measures) and for reducing positive climate forcing through mitigation measures. Predicting future climate is one of the main scopes of climate models and this work, as was specified, looks at future projections for fulfilling its purpose.

In order to make meaningful projections for several decades or more into the future, various frameworks can be followed, of which the most widely adopted worldwide is the one of climate change scenarios. These are constructed on the basis of the actions affecting the climate that humans will undertake in the near future. Under the CMIP6 framework, a set of five scenarios based on the Shared Socio-economic Pathways (SSPs) were defined in such a way to cover the likely spread of possible future human emissions of greenhouse gases. These scenarios, which support the IPCC 6th Assessment Report, are named SSP1-1.9, SSP1-2.6, SSP2-4.5, SSP3-7.0, and SSP5-8.5. Scenarios are based on assumptions of how socio-economic systems could evolve over the 21st century, taking into account factors such as future population, urbanisation, GDP and the type of policies implemented. These assumptions underpin future projections following the scenarios, that provide information about future emissions or concentrations of greenhouse gases, aerosols, ozone-depleting substances, and land use over time [36]. Following the way they are defined, each SSP results in a different radiative forcing outcome by the end of the century (identified as the year 2100). In the convention followed by CMIP6, in which scenarios are referred to as *SSPx-y*,

Table 3.2: *SSP scenarios available, among those considered, for the models employed in this study.*

| No. | Model | SSP1-2.6 | SSP2-4.5 | SSP5-8.5 |
|-----|------------------|----------|----------|----------|
| 1. | ACCESS-CM2 | ✓ | ✓ | ✓ |
| 2. | ACCESS-ESM1-5 | | ✓ | ✓ |
| 3. | BCC-CSM2-MR | ✓ | ✓ | ✓ |
| 4. | CAMS-CSM1-0 | ✓ | ✓ | ✓ |
| 5. | CanESM5 | ✓ | ✓ | ✓ |
| 6. | CAS-ESM2-0 | ✓ | ✓ | ✓ |
| 7. | CESM2-WACCM | ✓ | ✓ | ✓ |
| 8. | CIESM | ✓ | ✓ | ✓ |
| 9. | CMCC-CM2-SR5 | ✓ | ✓ | ✓ |
| 10. | CMCC-ESM2 | ✓ | ✓ | ✓ |
| 11. | E3SM-1-1 | | | ✓ |
| 12. | EC-Earth3 | ✓ | ✓ | ✓ |
| 13. | EC-Earth3-CC | | ✓ | ✓ |
| 14. | EC-Earth3-Veg | ✓ | ✓ | ✓ |
| 15. | EC-Earth3-Veg-LR | ✓ | ✓ | ✓ |
| 16. | FGOALS-f3-L | ✓ | ✓ | ✓ |
| 17. | FGOALS-g3 | ✓ | ✓ | ✓ |
| 18. | FIO-ESM-2-0 | ✓ | ✓ | ✓ |
| 19. | GFDL-CM4 | | ✓ | ✓ |
| 20. | GFDL-ESM4 | ✓ | ✓ | ✓ |
| 21. | INM-CM4-8 | ✓ | ✓ | ✓ |
| 22. | INM-CM5-0 | ✓ | ✓ | ✓ |
| 23. | IPSL-CM5A2-INCA | ✓ | | |
| 24. | IPSL-CM6A-LR | ✓ | ✓ | ✓ |
| 25. | MIROC6 | ✓ | ✓ | ✓ |
| 26. | MPI-ESM1-2-HR | ✓ | ✓ | ✓ |
| 27. | MPI-ESM1-2-LR | ✓ | ✓ | ✓ |
| 28. | MRI-ESM2-0 | ✓ | ✓ | ✓ |
| 29. | NESM3 | ✓ | ✓ | ✓ |
| 30. | NorESM2-LM | ✓ | ✓ | ✓ |
| 31. | NorESM2-MM | ✓ | ✓ | ✓ |
| 32. | TaiESM1 | ✓ | ✓ | ✓ |

these are indicated by y , while x is the code of the SSP. Therefore, the approximate end-of-century radiative forcing taken into account by the scenarios are, in increasing order, 1.9 W m^{-2} , 2.6 W m^{-2} , 4.5 W m^{-2} , 7.0 W m^{-2} and 8.5 W m^{-2} . Fig. 3.2 shows the Shared Socio-economic Pathways foreseen by CMIP6 and the climate outcomes in terms of forcing as a matrix of possible scenarios.

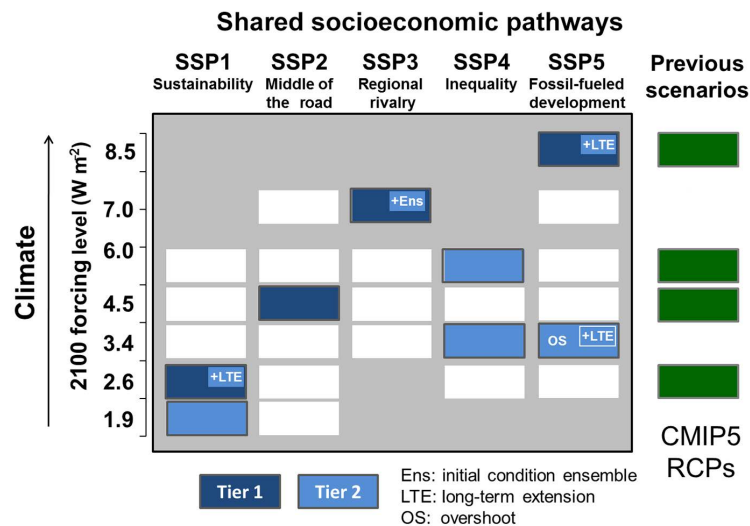


Figure 3.2: SSP-RCP scenario matrix illustrating CMIP6 simulations. Each cell indicates a combination of SSPs and climate outcome based on a particular forcing pathway. Dark blue cells indicate the key scenarios at the basis of climate model projections; light blue cells indicate additional scenarios of interest. White cells indicate scenarios for which climate information is supposed to come from the SSP scenario simulated for that row. Green cells indicate the corresponding CMIP5 RCPs for each row, which were developed from previous socio-economic scenarios rather than SSPs. Figure taken from O’Neill et al., 2016 [7].

SSP1-1.9 represents the low end of future emission pathways, leading to warming below $1.5 \text{ }^\circ\text{C}$ in 2100 and limited temperature overshoot of $1.5 \text{ }^\circ\text{C}$ over the course of this century. Fulfilling it would require huge efforts in terms of emissions reduction and mitigation; it constitutes the scenario that would be followed under the goal of limiting global mean warming to $1.5 \text{ }^\circ\text{C}$ above pre-industrial levels based on the Paris COP21 agreement (UNFCCC, 2015). SSP1-2.6 represents as well a scenario of sustainable-oriented growth, foreseeing strong climate change mitigation and thus low GHG emissions. It was designed to limit global warming within $2 \text{ }^\circ\text{C}$ compared to the pre-industrial era, so is suitable to support policy goals. It stabilises CO_2 at a mole fraction of about 450 ppm by the end of the century. CO_2 emissions in SSP1-1.9 and SSP1-2.6 are declining to net zero around 2050 and 2075 respectively, followed by varying levels of net negative CO_2 emissions, as can be appreciated in Fig. 3.3. SSP2-4.5 is a scenario with intermediate GHG emissions and CO_2 emissions remaining around current levels until the middle of the century and decreasing afterwards, though its concentration reaches 600 ppm by 2100. In SSP3-7.0, scenario with high GHG emissions, CO_2 ones roughly double from current levels by the end of the century, while in SSP5-8.5 they double around 2050. SSP5-8.5, the highest emission scenario, represents the path we are currently on, sometimes called the “business as usual” scenario. It represents a scenario with unconstrained economic growth and fossil-fuel use, in which CO_2 concentration

overcomes 1100 ppm by 2100, provoking mean global warming of 4-5 °C by that time compared to the pre-industrial period.

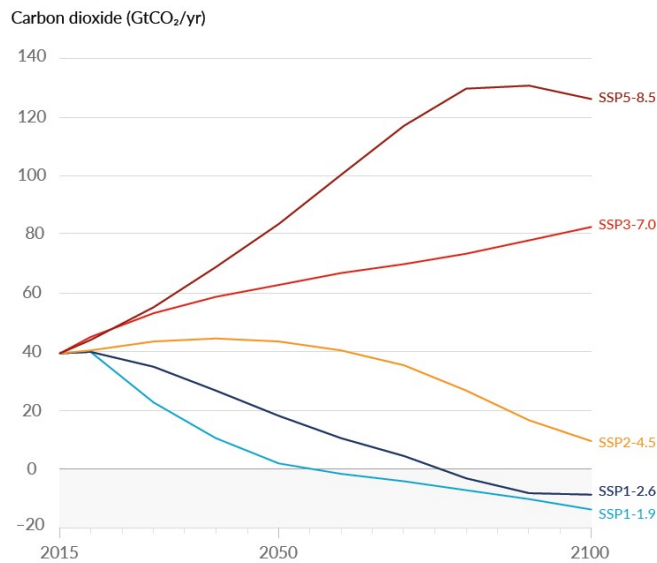


Figure 3.3: Future annual emissions of CO₂ across the five SSP scenarios. Figure taken from IPCC (2021), Assessment Report 6, Working Group I, Summary for Policymakers, Fig. SPM.4 [8].

In CMIP6 models, the period of future projections goes from 2015, after the historical one ends, to 2100; however, some modelling teams developed extended runs until 2300, whereas others stopped the simulations at 2099. For this last reason, in the study it was chosen to investigate future projections until 2099, in order to encompass the largest possible number of models. As far as scenarios are concerned, among the described ones three were selected to conduct the analyses: SSP1-2.6, SSP2-4.5 and SSP5-8.5. These were opted for since deemed the most reasonable ones: the first one envisages a marked decarbonisation, as well as SSP2-4.5, which can be considered a “middle of the road” scenario. On the other hand, SSP5-8.5 is the worst-case scenario, at the opposite end of the future emission pathways range. Not all the CMIP6 models were run over each SSP scenario by the scientist teams: Table 3.2 indicates, among the three considered ones, the scenarios available for the 32 models employed in the study.

3.2 Data and methods

In order to analyse CMIP6 model outcomes it was first necessary to retrieve and download a considerable amount of data. These data, provided with a monthly frequency, were obtained from the ESGF database¹, the official source of global climate data. The purpose of the platform is in fact to develop and maintain “software infrastructure for the management, dissemination, and analysis of model output and observational data”. The CMIP framework guarantees high quality gridded climate data across the globe in a standardised format: in fact, all the model output data are in the same format, called “netCDF” (acronym for Network Common Data Form). This

¹ <https://esgf-node.llnl.gov/projects/esgf-llnl/>

file format, with a *.nc* extension, is very convenient for the climate community, as it allows to store metadata, such as dimensions, variables and global attributes, and contains also precise descriptions of all information used.

Data were retrieved from the ESGF through the software tool “synda”, allowing the construction of a permanent mirror of a part of the ESGF climate model simulation archive². The first processing operations were performed on raw data with the CDO (Climate Data Operators) software, a collection of command-line operators developed by the Max Planck Institute for Meteorology (Hamburg, Germany) to manipulate climate and forecast model data³. The netCDF files output of the models were then processed and analysed on MATLAB environment, using the release 2020b of the software [70]. Whenever a specific function was utilised for carrying out an analysis, that will be pointed out and cited during the explanation of the procedure.

² <https://prodiguer.github.io/synda/>

³ <https://code.mpimet.mpg.de/projects/cdo/>

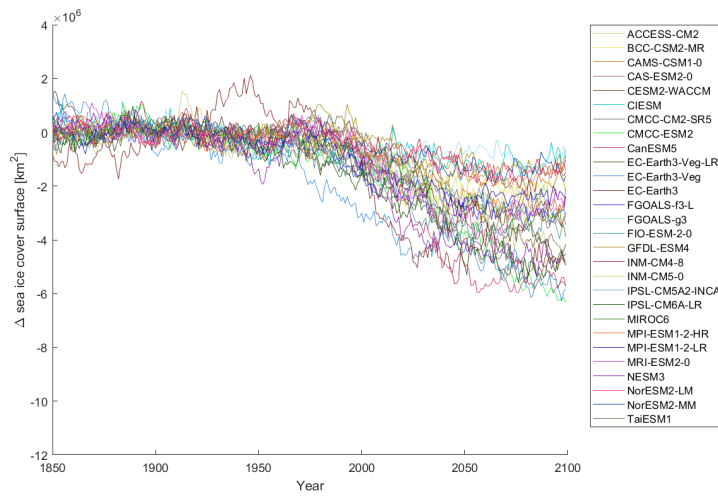
Chapter 4

Definition of clusters of models based on sea ice cover projections

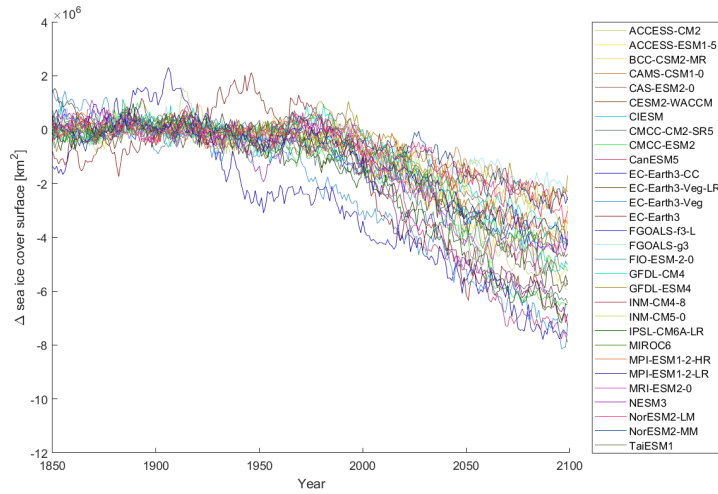
As anticipated in chapter 3, the first part of the analysis is dedicated to isolate the response to future Arctic sea ice changes from its correlation with global temperature ones, due to the ice-albedo feedback. For this initial phase, an approach similar to the one employed by Bellomo et al. (2021) is followed [71]. In particular, differences in sea ice cover are normalised by the corresponding differences in global mean surface temperature (from now on identified as *GMT*): in this way, the difference in *sensitivity* of sea ice cover changes in regard to the temperature variation is analysed.

First of all, since in every considered model sea ice is based on a non-structured grid, all the models are interpolated on a common grid. A resolution of 0.5° both in latitude and longitude is chosen, corresponding to the finest one among the CMIP6 models. In the models, sea ice cover is quantified in terms of sea ice concentration, variable identified as *siconc*. In order to visualise sea ice trend in time in the Northern Hemisphere, *siconc* values in each cell – expressed in covered fraction – are multiplied by the respective area of the cells and summed up, thereby obtaining the total coverage of Arctic sea ice, expressed in km^2 . Yearly values of sea ice cover are plotted from the historical period up to future projections under the three different scenarios, namely SSP1-2.6, SSP2-4.5 and SSP5-8.5. The initial sea ice cover value in the historical period, which in the runs starts in the year 1850, varies largely among the models: the mean annual Arctic sea ice area, in fact, ranges in that period from about 7.5 to 14 million km^2 . Therefore, comparing sea ice cover with a reference period is deemed more meaningful rather than considering values so different between models. The historical reference period, that from now on will be consistent for all variables within the thesis, is picked as the 101 years comprised between 1850 and 1950 included, since in that period models didn't experience sea ice loss, whose area was almost constant. Besides, a such long reference period has the advantage to remove some internal variability, which in the historical run is quite large. Fig. 4.1 compares timeseries of sea ice cover anomaly in the Northern Hemisphere for each model in the three scenarios, that is, sea ice cover mean in the 1850-1950 period subtracted from sea ice yearly values. The plotted time frame goes from 1850 to 2099. In this way time variations of ocean surface covered by sea ice and the variability of the models under the different experiments can be appreciated. To be better comparable, the three plots have the same vertical axis range, so the one taken from the SSP5-8.5 scenario, which shows the highest sea ice anomalies.

(a) *SSP1-2.6*



(b) *SSP2-4.5*



(c) *SSP5-8.5*

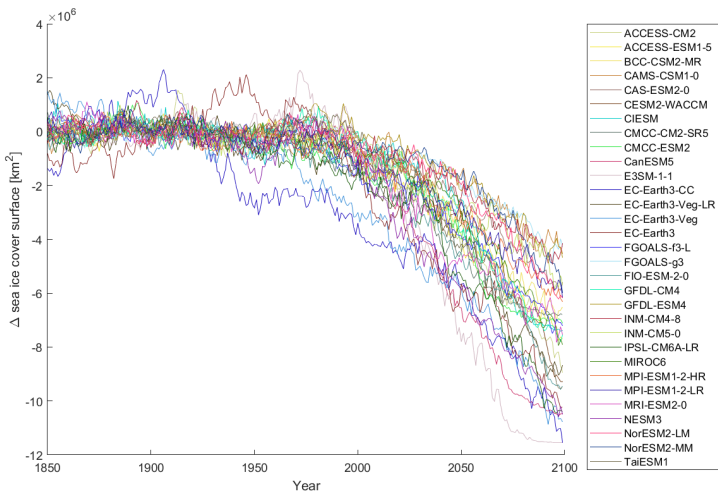


Figure 4.1: Northern Hemisphere sea ice area anomaly from 1850-1950 average under the three scenarios.

From the graphs, it can be observed that the area covered by sea ice remained almost constant until the early eighties, from which it started decreasing. In SSP5-8.5, the highest emission scenario, sea ice reduction is the most dramatic: in particular, the model E3SM-1-1 projects a practically ice-free Arctic Ocean all year round by the end of the century, as can be seen from the lower plateau reached by the tail of its timeseries.

4.1 Correlation between global mean temperature and Arctic sea ice cover

It is clear that, owing to the ice-albedo feedback, the projected decline of sea ice will have a direct impact on the climate, because the temperatures in the Arctic Ocean will change. The interest, though, is to investigate also other changes associated with it: hence the need to distinguish and separate the effects to sea ice and temperature variations. In fact, being the two variables related through a feedback process, it is even difficult to detect which phenomenon triggered the other. In order to isolate the effect of sea ice from that of temperature, an approach similar to the one employed by Bellomo et al. (2021) is adopted [71]. In particular, to extract the difference in sea ice cover changes with respect to the temperature variation, differences in sea ice area are normalised by the corresponding differences in global mean surface temperature (GMT).

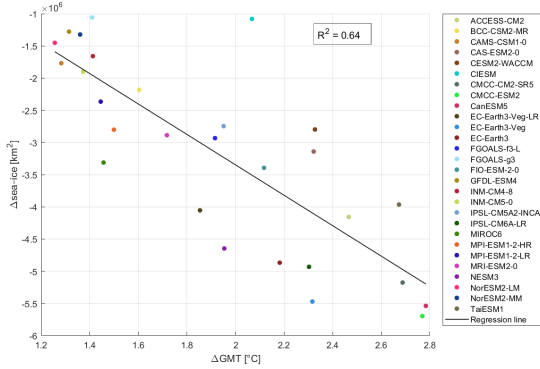
For this purpose, firstly two reference periods are defined: the historical baseline, already mentioned, spanning the century between 1850 and 1950, and a future time frame between 2070 and 2099, that is, the last thirty years of the models' future projections. A difference in sea ice area is computed between the mean of the end-of-century and the mean of the historical period, constituting the $\Delta sea - ice$; the same difference is computed for the variable GMT (ΔGMT). These two quantities, calculated for each model, are then divided, forming the index $\frac{\Delta sea - ice}{\Delta GMT}$. In this way, by normalising by the GMT , it can be evaluated the sensitivity of the models in regard to sea ice loss: in fact, models in which Arctic sea ice declines more have a greater sensitivity, and vice versa.

So, in order to detect the magnitude of the correlation between temperature variations and sea ice ones, scatter plots are employed, one for each scenario. These, having ΔGMT on the x axis and $\Delta sea - ice$ on the y axis, are also an effective way to assess the sensitivity of the considered models. In Fig. 4.2 are reported the scatter plots showing, in each scenario, the relation between sea ice difference and global mean temperature one for every model: in the left plots, only Northern Hemisphere sea ice is considered, in the right ones all world sea ice. In the plots, the black line represents the linear regression between the models; the value of the coefficient of determination R^2 is included as well, providing a measure of the correlation between the two variables.

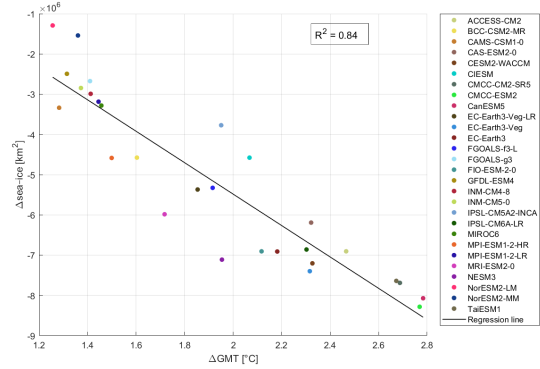
As expected, the plots on the right side exhibit a tighter correlation between $\Delta sea - ice$ and ΔGMT , proved by $R^2 = 0.84 - 0.85$, because in those cases it is considered the total global sea ice cover difference, and ΔGMT is a global quantity too. However, since the focus of the research is on the effects of Arctic sea ice decrease, the scatter plots based on the difference in Northern Hemisphere sea ice are taken into account for the formation of the clusters of models, as will be explained in paragraph 4.2. These scatter plots confirm the existence of a quite strong correlation between expected Arctic sea ice decrease and global mean temperature increase, more marked in

4.1 Correlation between global mean temperature and Arctic sea ice cover

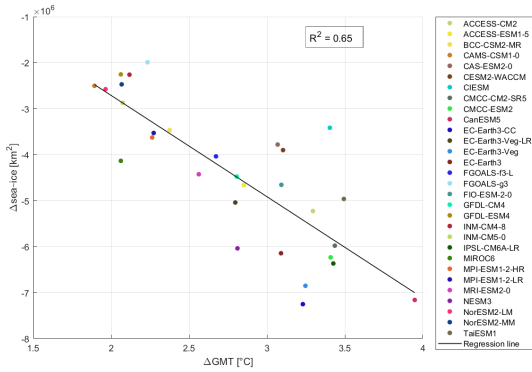
(a) SSP1-2.6 – Northern Hemisphere sea ice



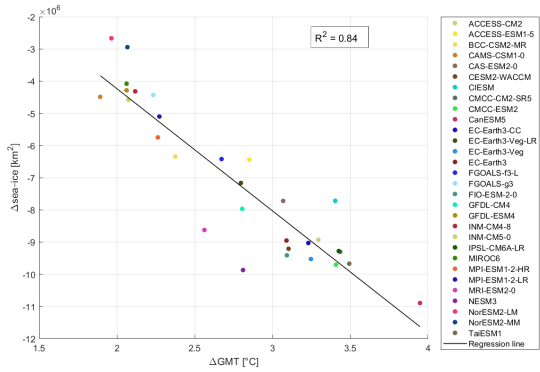
(b) SSP1-2.6 – Global sea ice



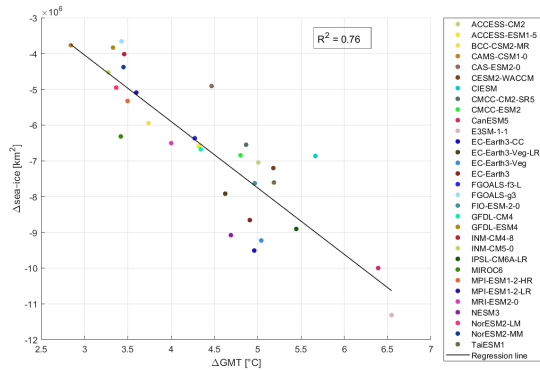
(c) SSP2-4.5 – Northern Hemisphere sea ice



(d) SSP2-4.5 – Global sea ice



(e) SSP5-8.5 – Northern Hemisphere sea ice



(f) SSP5-8.5 – Global sea ice

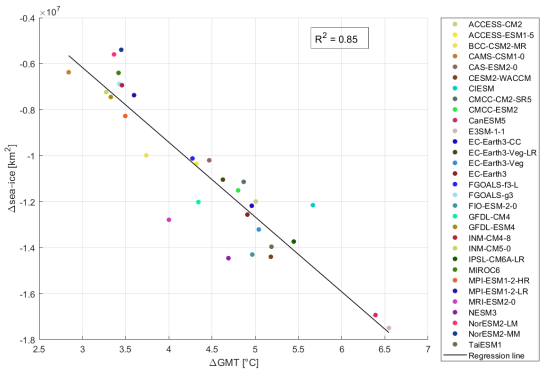


Figure 4.2: Scatter plots showing, in each scenario, the relation between sea ice difference and global mean temperature difference for every model. Differences are computed between the means of the periods 2070-2099 and 1850-1950. In the left plots, Northern Hemisphere sea ice is considered, in the right ones all world sea ice.

the most extreme scenario ($R^2 = 0.76$), thus supporting the usefulness of normalising $\Delta_{sea-ice}$ by Δ_{GMT} . Thereby, the models' sensitivity to sea ice changes is highlighted, and from the plots different sensitivities can be appreciated among the models.

The correlation between temperature and sea ice can be investigated also from another point of view, by visualising a timeseries of Northern Hemisphere (NH) sea ice cover evolution as a function of GMT evolution. For this purpose, it is first necessary to filter both the timeseries of NH sea ice area anomaly relative to the mean of the historical baseline (in Fig. 4.1) and the GMT anomaly timeseries relative to the mean of the same period (1850-1950). In this way, the unwanted noisy component present in the original data is filtered, resulting in a smoother signal. The approach followed is that of a moving average, a simple kind of low-pass filter. In practice, a moving window of 21 years is selected (filter length) and scrolled on the two timeseries. For each year of the timeseries, 21 sample years are taken – the previous 10 years, the input year and the following 10 – and their average value is attributed to the input year. By applying this moving average filter, the 10 initial and last years of the timeseries are lost, so that the period taken into account becomes 1860-2089 both for the timeseries of NH sea ice anomaly and GMT anomaly compared to the historical baseline. A filter length of 21 years is considered appropriate in order to smooth the sharp peaks in the original timeseries; on the other hand, a higher filter length would have produced increasingly blunt output data, with the risk of losing important information. The results of the filtering are shown, for the three scenarios, in Fig. 4.3, both for sea ice area and GMT. The filtered series are much smoother than how they appeared originally; besides, by comparing Arctic sea ice area and global mean temperature projections, in any scenario the two timeseries seem mirrored, meaning that the rate of global temperature increase seems proportional to that of Arctic sea ice decrease.

These filtered timeseries are employed to plot a graph of NH sea ice cover anomaly as function of GMT anomaly. In fact, for each scenario, one is plotted against the other, in a way that global mean temperature – on the x axis – works as time coordinate. This kind of graph allows to appreciate the evolution of the models, as well as the inter-model spread. Fig. 4.4 reports the plots for the SSP2-4.5 and SSP5-8.5 scenarios, in which the models reach a rather high level of global warming. The graphics are interesting and useful for the investigation of the trend of NH sea ice cover as a function of temperature. As a matter of fact, after an initial phase in which the models broaden, the relationship between the two variables' anomalies remains approximately linear. This aspect finds confirmation in the work by Mahlstein and Knutti (2012), who suggested an approximate linear relationship between global temperature change and Arctic sea ice area decline [72], as well as in IPCC AR6 statements [36]. In the initial phase, between 0 and +1 °C of global warming, the relationship between sea ice and temperature changes is more complicated, since a lot of variability is present. After this stage, models stabilise and follow a given trajectory, mainly linear: this reflects the ice-albedo feedback, which causes a further sea ice decrease in response to a mean temperature increase. It is interesting to note that, after a first stabilisation, the models' lines, almost straight, have a comparable slope. If checking the scenario SSP2-4.5 against the SSP5-8.5 one, in their common interval models from SSP2-4.5 appear almost overlapping to those in SSP5-8.5, and some of them are even following the same trajectory between the two scenarios. Definitely, these graphs constitute other proofs of the clear correlation linking Arctic sea ice area decrease and global temperature rise. What is more, in the perspective of the

4.1 Correlation between global mean temperature and Arctic sea ice cover

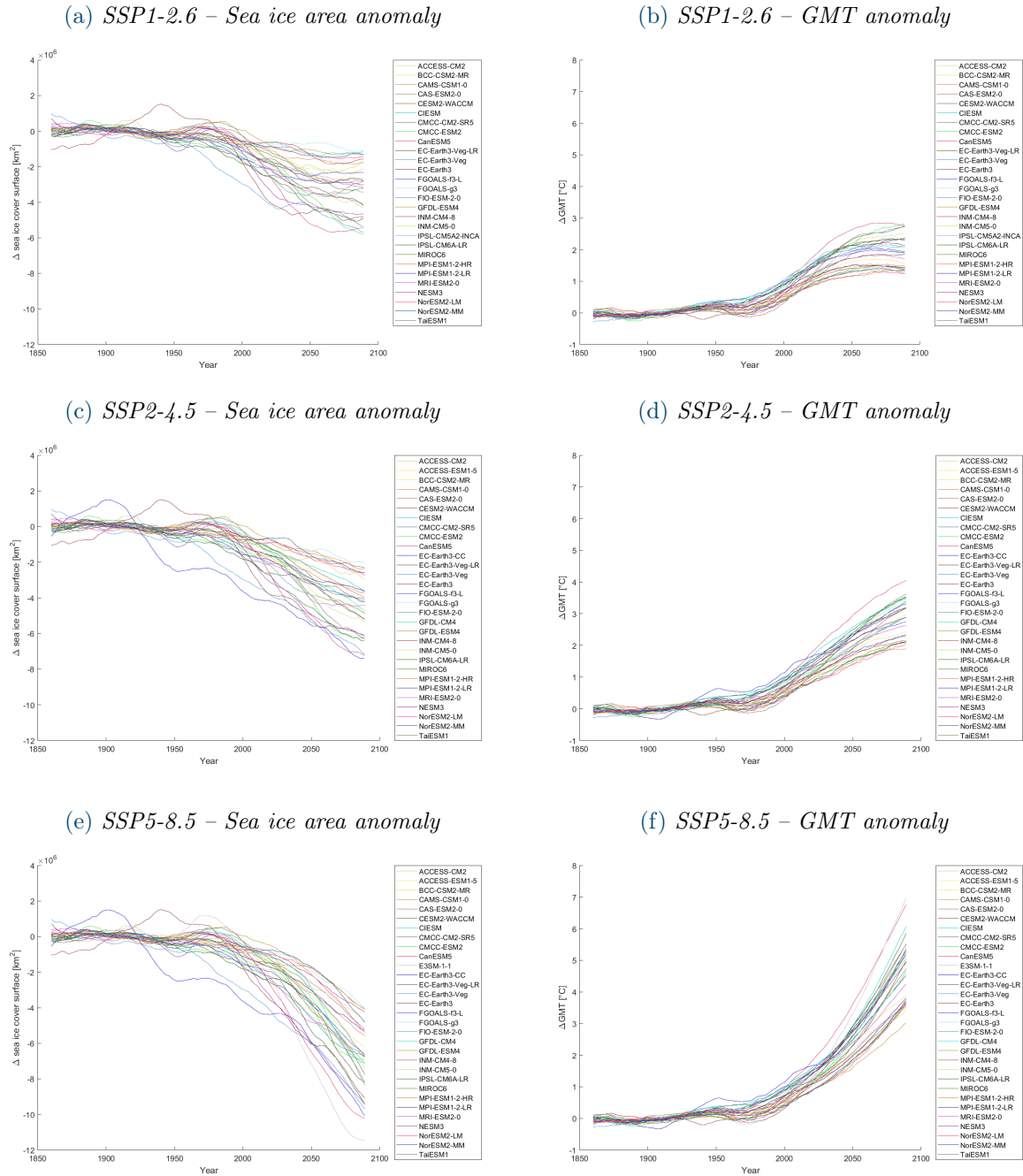


Figure 4.3: 21-year moving average filtered timeseries of (left) Northern Hemisphere sea ice area and (right) GMT anomalies from 1850-1950 average under the three scenarios.

definition of global warming levels – introduced in section 4.3 – these plots are useful to appreciate the spread between models at a given level of global mean temperature, input on the x axis.

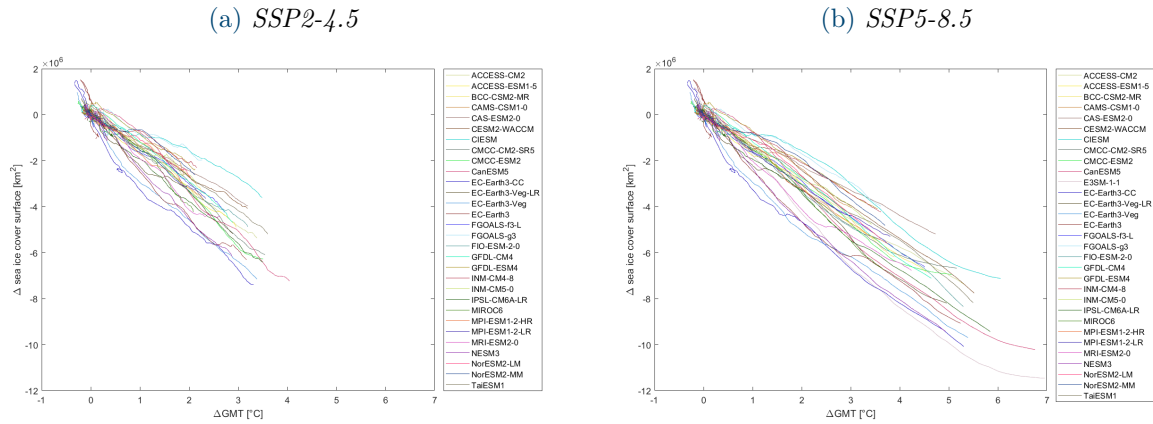


Figure 4.4: Northern Hemisphere sea ice area anomaly as function of GMT anomaly. Based on 21-year moving average filtered timeseries.

A further countercheck is carried out in order to verify the soundness of taking into account the correlation between temperature rise and sea ice decline rather than between temperature rise and sea ice area in absolute terms. To this aim, the same scatter plots in Figures 4.2a, 4.2c and 4.2e are produced, but having on the y axis the sea ice area value reached at the end of the century, that is, the 2070-2099 average. These plots, not reported herein, demonstrate a lower correlation between end-of-century sea ice area and ΔGMT : the R^2 values for the three scenarios, in increasing order of emissions, are 0.56, 0.55 and 0.68, whereas when taking into account $\Delta sea-ice$ against ΔGMT R^2 equal respectively 0.64, 0.65 and 0.76. This proves once more the soundness of investigating Arctic sea ice cover differences (Δ) rather than the values of cover surface projected, since in the first case the correlation between the two quantities is intensified in the models. Furthermore, in the scatter plots having the average 2070-2099 sea ice area value on the vertical axis, some models lie far away from the regression line. In particular, the models CMCC-CM2-SR5 and CMCC-ESM2 lie quite below the line, apart from the group formed by the other models: by looking at the initial sea ice area values in the timeseries, it results that these models are the two with the lowest cover surface in the historical period, having 1850-1950 averages even lower than 7.5 million km^2 . This example underlines the importance of considering sea ice change compared to the baseline, since all the models start from different initial sea ice cover values in the historical period, as pointed out previously.

4.2 Definition of clusters of models

The scatter plots in Fig. 4.2 (left side) represent both a proof of the marked correlation linking Arctic sea ice cover loss with global mean temperature rise, both a measure of the different sensitivities of the models to sea ice variations compared to temperature ones. The sensitivities are expressed by the parameter $\frac{\Delta sea-ice}{\Delta GMT}$ – where Δ indicates differences between 2070-2099 and 1850-1950 averages – distinct for each model: it identifies how much Arctic sea ice will decrease per global warming unit. In order to detect changes in the climate attributable to sea ice decline,

models are separated in two clusters, projecting great and low NH sea ice loss compared to temperature rise. This division is carried out on the basis of the distribution of the models' sensitivities, but must find confirmation in the differences in spatial patterns too.

Through the distribution of the sensitivity of the models it is possible to group them into clusters: in fact, models with higher sensitivity are those projecting the largest Arctic sea ice decline, and vice versa. As already highlighted, the three scatter plots in Figures 4.2a, 4.2c and 4.2e are effective ways for visualising the distribution of the sensitivities of the models employed in the three scenarios. In each scenario, the distribution of the parameter $\frac{\Delta_{sea-ice}}{\Delta_{GMT}}$ (in absolute value) across the models is divided into terciles: the upper tercile includes the models that vary the most in NH sea ice area, whereas the lower tercile those that vary less. Visually, in the previous graphics the models belonging to the upper tercile of the distribution lie below the regression line of the sensitivities and the models belonging to the lower tercile of the distribution lie above the regression line. The division of the models in terciles is reported in the scatter plots in Fig. 4.5, one for each scenario. The formation of the clusters of models is performed on terciles of the distribution, rather than simply splitting the distribution in two, in order to obtain a clear separation of the models, mainly in the case of those at the middle of the distribution of normalised sea ice variation.

Since in the three scenarios the distribution of the models' normalised sea ice cover decrease varies, the division of the models in terciles is made separately for every scenario, thus creating different model groups. Then, during the definition of the global warming levels, all the models belonging to the same clusters are put together, as will be discussed later. The models belonging to the clusters of smaller and greater normalised Arctic sea ice decrease are listed, for each scenario, in Tables 4.1, 4.2 and 4.3. In the SSP1-2.6 scenario, for which 28 models are available, the greater and smaller clusters are composed by 9 models each, while in both SSP2-4.5 and SSP5-8.5 they are composed by 10 models each. From the tables it can be noticed that the values of the sensitivity parameter are more widespread the lower is the scenario, consistently with the lower correlation between $\Delta_{sea-ice}$ and Δ_{GMT} resulting from the scatter plots. Furthermore, the models belonging to the two clusters are in most cases the same throughout the three scenarios: this constitutes an important demonstration of the robustness of the method.

In this phase, to further prove the correctness of the attribution of models to the clusters, we plot maps of sea ice cover difference between the means of the periods 2070-2099 and 1850-1950, normalised by GMT difference between the same periods. These maps, that are not reported, are plotted individually for each model. Even from the maps can be detected remarkable differences in sensitivity to Arctic sea ice cover decline with respect to temperature rise across the models, at least in certain areas. By checking the maps against the scatter plots, we find correspondence between models with higher or lower sensitivity. The division of the models in two clusters of greater and smaller Arctic sea ice change is therefore validated by the differences in spatial patterns.

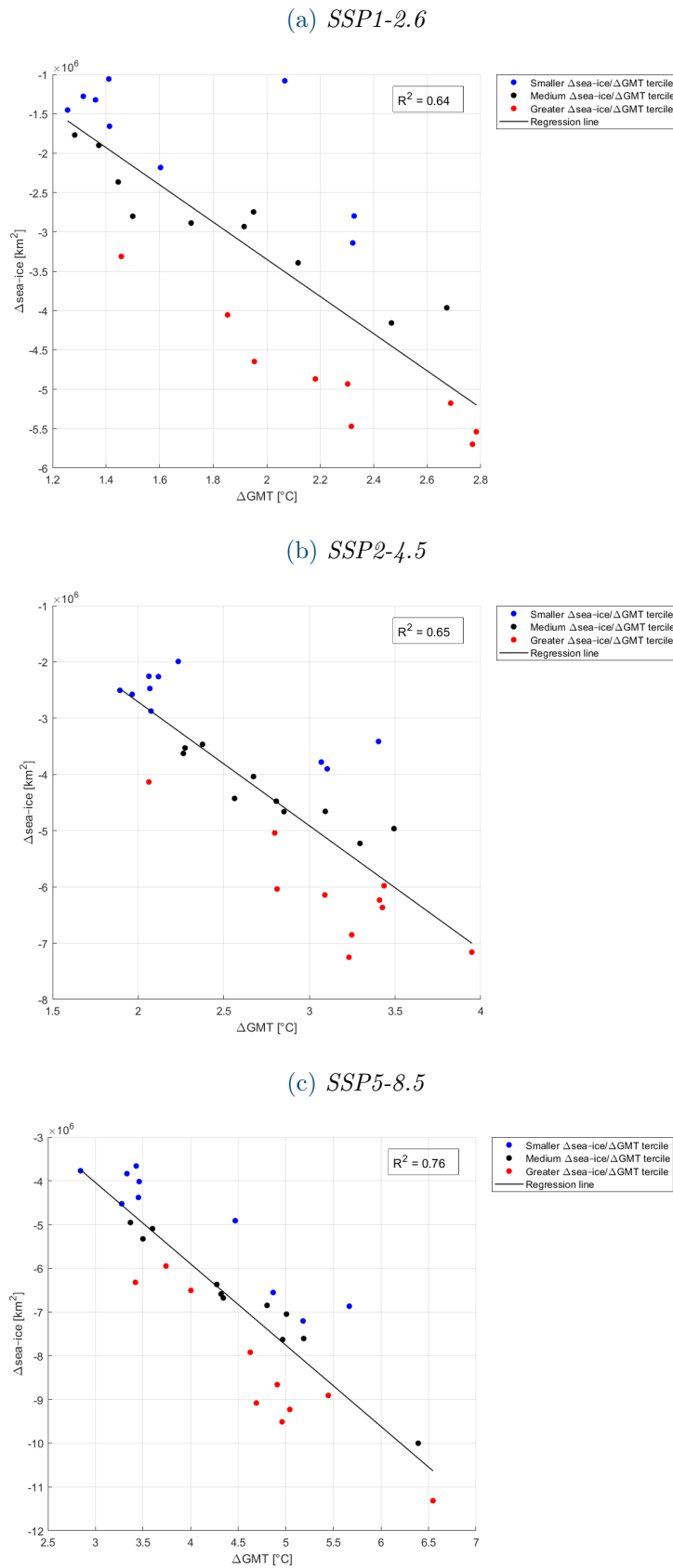


Figure 4.5: Scatter plots of NH sea ice difference against global mean temperature difference for every model showing, in each scenario, the division of the models in tertiles. Differences are computed between the means of the periods 2070-2099 and 1850-1950.

Table 4.1: Models belonging to the clusters of smaller and greater normalised NH sea ice decrease, along with their respective sensitivity value, in the SSP1-2.6 scenario.

| Models with smaller norm. decrease | $\frac{\Delta_{sea-ice}}{\Delta_{GMT}}$ [km ² /°C] | Models with greater norm. decrease | $\frac{\Delta_{sea-ice}}{\Delta_{GMT}}$ [km ² /°C] |
|------------------------------------|---|------------------------------------|---|
| BCC-CSM2-MR | -1.3609E+06 | CMCC-CM2-SR5 | -1.9258E+06 |
| CAS-ESM2-0 | -1.3529E+06 | CMCC-ESM2 | -2.0575E+06 |
| CESM2-WACCM | -1.2025E+06 | CanESM5 | -1.9901E+06 |
| CIESM | -5.2259E+05 | EC-Earth3-Veg-LR | -2.1873E+06 |
| FGOALS-g3 | -7.5022E+05 | EC-Earth3-Veg | -2.3621E+06 |
| GFDL-ESM4 | -9.7244E+05 | EC-Earth3 | -2.2310E+06 |
| INM-CM4-8 | -1.1743E+06 | IPSL-CM6A-LR | -2.1419E+06 |
| NorESM2-LM | -1.1560E+06 | MIROC6 | -2.2735E+06 |
| NorESM2-MM | -9.7251E+05 | NESM3 | -2.3783E+06 |

Table 4.2: Models belonging to the clusters of smaller and greater normalised NH sea ice decrease, along with their respective sensitivity value, in the SSP2-4.5 scenario.

| Models with smaller norm. decrease | $\frac{\Delta_{sea-ice}}{\Delta_{GMT}}$ [km ² /°C] | Models with greater norm. decrease | $\frac{\Delta_{sea-ice}}{\Delta_{GMT}}$ [km ² /°C] |
|------------------------------------|---|------------------------------------|---|
| CAMS-CSM1-0 | -1.3227E+06 | CMCC-CM2-SR5 | -1.7404E+06 |
| CAS-ESM2-0 | -1.2319E+06 | CMCC-ESM2 | -1.8288E+06 |
| CESM2-WACCM | -1.2570E+06 | CanESM5 | -1.8136E+06 |
| CIESM | -1.0031E+06 | EC-Earth3-CC | -2.2448E+06 |
| FGOALS-g3 | -8.9135E+05 | EC-Earth3-Veg-LR | -1.8022E+06 |
| GFDL-ESM4 | -1.0928E+06 | EC-Earth3-Veg | -2.1105E+06 |
| INM-CM4-8 | -1.0672E+06 | EC-Earth3 | -1.9884E+06 |
| INM-CM5-0 | -1.3846E+06 | IPSL-CM6A-LR | -1.8585E+06 |
| NorESM2-LM | -1.3109E+06 | MIROC6 | -2.0047E+06 |
| NorESM2-MM | -1.1949E+06 | NESM3 | -2.1481E+06 |

Table 4.3: Models belonging to the clusters of smaller and greater normalised NH sea ice decrease, along with their respective sensitivity value, in the SSP5-8.5 scenario.

| Models with smaller norm. decrease | $\frac{\Delta_{sea-ice}}{\Delta_{GMT}}$ [km ² /°C] | Models with greater norm. decrease | $\frac{\Delta_{sea-ice}}{\Delta_{GMT}}$ [km ² /°C] |
|------------------------------------|---|------------------------------------|---|
| CAMS-CSM1-0 | -1.3261E+06 | BCC-CSM2-MR | -1.5905E+06 |
| CAS-ESM2-0 | -1.0992E+06 | E3SM-1-1 | -1.7282E+06 |
| CESM2-WACCM | -1.3905E+06 | EC-Earth3-CC | -1.9172E+06 |
| CIESM | -1.2118E+06 | EC-Earth3-Veg-LR | -1.7122E+06 |
| CMCC-CM2-SR5 | -1.3464E+06 | EC-Earth3-Veg | -1.8305E+06 |
| FGOALS-g3 | -1.0679E+06 | EC-Earth3 | -1.7636E+06 |
| GFDL-ESM4 | -1.1518E+06 | IPSL-CM6A-LR | -1.6355E+06 |
| INM-CM4-8 | -1.1613E+06 | MIROC6 | -1.8484E+06 |
| INM-CM5-0 | -1.3809E+06 | MRI-ESM2-0 | -1.6256E+06 |
| NorESM2-MM | -1.2694E+06 | NESM3 | -1.9358E+06 |

4.2.1 EC-Earth3 ensemble test

Another test is carried out to verify the robustness of the detected signal. In the case of many models, the research groups executed several realisations, meaning ensembles of experiments performed with the same model. For this reason, it is interesting to check if even other realisations of the models fall under the same cluster of the model adopted for the analysis (i.e., its realisation r1i1p1f1). This test aims to evaluate the soundness of the signal in regard to the internal variability that each model has, because with several realisations you span all the internal variability of a model.

To keep it within reasonable limits, the analysis is applied on the ensemble of realisations of the model EC-Earth3, which was run under many different realisations. As a matter of fact, this model belongs firmly to the cluster of greater normalised sea ice decrease in all the three scenarios, so it constitutes a proper basis for the test. For the list of realisations of EC-Earth3 employed in the three scenarios, namely the ones for which both historical and future sea ice and temperature data are available, refer to Table 4.4. In particular, 4 realisations of the model are employed in scenario SSP1-2.6, 19 in SSP2-4.5 and 7 in SSP5-8.5. The procedure applied is exactly the same used for the other models: the sensitivity is assessed graphically through scatter plots, having as x-coordinate ΔGMT and as y-coordinate $\Delta sea - ice$, computed as usual as differences between the averages of the future and historical periods.

Table 4.4: List of the realisations of the model EC-Earth3 employed in the three scenarios for the test.

| SSP1-2.6 | SSP2-4.5 | SSP5-8.5 |
|-----------|-----------|-----------|
| r1i1p1f1 | r1i1p1f1 | r1i1p1f1 |
| | r2i1p1f1 | |
| | | r3i1p1f1 |
| r4i1p1f1 | r4i1p1f1 | r4i1p1f1 |
| r6i1p1f1 | r6i1p1f1 | r6i1p1f1 |
| | r7i1p1f1 | |
| | r10i1p1f1 | |
| r11i1p1f1 | r11i1p1f1 | r11i1p1f1 |
| | r12i1p1f1 | |
| | r13i1p1f1 | r13i1p1f1 |
| | r14i1p1f1 | |
| | r15i1p1f1 | r15i1p1f1 |
| | r17i1p1f1 | |
| | r18i1p1f1 | |
| | r20i1p1f1 | |
| | r21i1p1f1 | |
| | r22i1p1f1 | |
| | r23i1p1f1 | |
| | r24i1p1f1 | |
| | r25i1p1f1 | |

The result is robust, since the whole ensemble of models (30 in total) falls, for the three scenarios, within the upper tercile of the distribution of $\frac{\Delta_{sea-ice}}{\Delta GMT}$. This is also visually confirmed by the scatter plots, in which all the realisations lie below the regression line: in Fig. 4.6 it is reported the plot for the scenario SSP2-4.5, the most representative for this purpose due to the highest number of EC-Earth3 realisations, marked in green. In fact, the span of the internal variability of the model EC-Earth3 falls below the line, that to a first approximation divides the models in terciles. The outcome of this analysis is important, as it proves that the differences between the models detected previously are not accidental but represent a real property of the models. Therefore, the test suggests that the assignment of the models to one cluster or the other is robust and reveals a real signal.

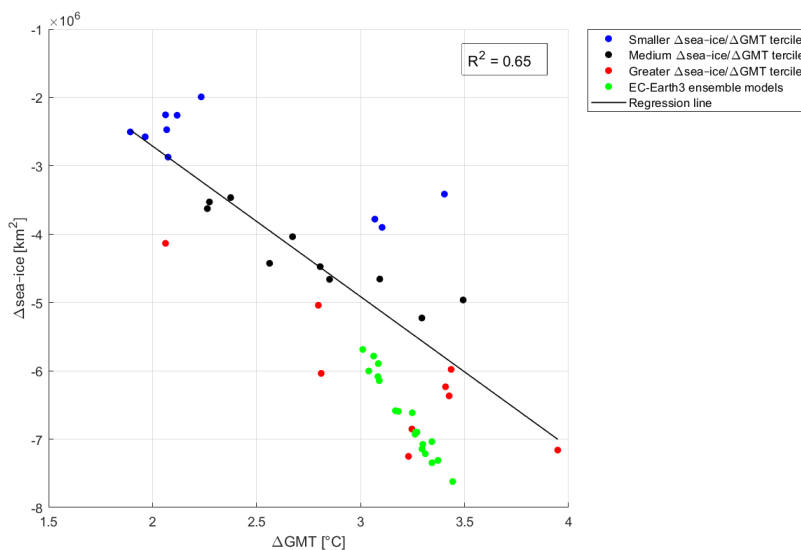


Figure 4.6: Scatter plot of NH sea ice difference against global mean temperature difference for every model of the scenario SSP2-4.5, showing the division of the models in terciles and the ensemble of realisations of the model EC-Earth3 (in green). Differences are computed between the means of the periods 2070-2099 and 1850-1950.

4.3 Global warming levels definition

Once the clusters of models projecting greater and smaller Arctic sea ice decline are defined, the analysis is conducted at levels of global mean temperature warming. Global warming levels (GWLs), expressed in degrees, are usually integer values indicating the global mean temperature warming reached compared to a historical baseline. In order to work at levels of global warming, for each model, and in every scenario, it is necessary to identify the year in which a given GWL is reached compared to the average of the historical reference period (1850-1950). For this purpose, we employ the GMT anomaly timeseries filtered with a 21-year moving average visible in Figures 4.3b, 4.3d and 4.3f, which span the period 1860-2089. For every scenario is picked, from those timeseries, the first year in which in the models is attained a GWL: these can be consulted in Tables 4.5, 4.6 and 4.7.

Table 4.5: Year in which GWLs are reached in the models of the scenario SSP1-2.6, based on 21-year moving average filtered timeseries of GMT anomalies from 1850-1950 average.

| Model | Year GWL +1 °C | Year GWL +2 °C |
|------------------|-------------------|-------------------|
| ACCESS-CM2 | 2016 | 2043 |
| BCC-CSM2-MR | 2019 | / |
| CAMS-CSM1-0 | 2031 | / |
| CAS-ESM2-0 | 2019 | 2058 |
| CESM2-WACCM | 2008 | 2042 |
| CIESM | 2003 | 2054 |
| CMCC-CM2-SR5 | 2004 | 2040 |
| CMCC-ESM2 | 2006 | 2044 |
| CanESM5 | 2002 | 2028 |
| EC-Earth3-Veg-LR | 2011 | / |
| EC-Earth3-Veg | 2000 | 2049 |
| EC-Earth3 | 2006 | 2038 |
| FGOALS-f3-L | 2004 | / |
| FGOALS-g3 | 2008 | / |
| FIO-ESM-2-0 | 2001 | 2041 |
| GFDL-ESM4 | 2025 | / |
| INM-CM4-8 | 2020 | / |
| INM-CM5-0 | 2021 | / |
| IPSL-CM5A2-INCA | 1999 | 2039 |
| IPSL-CM6A-LR | 2005 | 2041 |
| MIROC6 | 2027 | / |
| MPI-ESM1-2-HR | 2015 | / |
| MPI-ESM1-2-LR | 2017 | / |
| MRI-ESM2-0 | 2016 | / |
| NESM3 | 2011 | 2057 |
| NorESM2-LM | 2030 | / |
| NorESM2-MM | 2023 | / |
| TaiESM1 | 2017 | 2040 |

Table 4.6: Year in which GWLs are reached in the models of the scenario SSP2-4.5, based on 21-year moving average filtered timeseries of GMT anomalies from 1850-1950 average.

| Model | Year GWL +1 °C | Year GWL +2 °C | Year GWL +3 °C | Year GWL +4 °C |
|------------------|-------------------|-------------------|-------------------|-------------------|
| ACCESS-CM2 | 2016 | 2041 | 2071 | / |
| ACCESS-ESM1-5 | 2015 | 2046 | / | / |
| BCC-CSM2-MR | 2019 | 2058 | / | / |
| CAMS-CSM1-0 | 2033 | / | / | / |
| CAS-ESM2-0 | 2019 | 2053 | 2082 | / |
| CESM2-WACCM | 2009 | 2042 | 2078 | / |
| CIESM | 2003 | 2030 | 2067 | / |
| CMCC-CM2-SR5 | 2004 | 2040 | 2069 | / |
| CMCC-ESM2 | 2006 | 2043 | 2067 | / |
| CanESM5 | 2002 | 2026 | 2052 | 2087 |
| EC-Earth3-CC | 1995 | 2037 | 2075 | / |
| EC-Earth3-Veg-LR | 2011 | 2054 | / | / |
| EC-Earth3-Veg | 2000 | 2040 | 2075 | / |
| EC-Earth3 | 2006 | 2041 | 2081 | / |
| FGOALS-f3-L | 2004 | 2043 | / | / |
| FGOALS-g3 | 2008 | 2067 | / | / |
| FIO-ESM-2-0 | 2001 | 2036 | 2080 | / |
| GFDL-CM4 | 2015 | 2050 | / | / |
| GFDL-ESM4 | 2023 | 2079 | / | / |
| INM-CM4-8 | 2019 | 2071 | / | / |
| INM-CM5-0 | 2022 | 2079 | / | / |
| IPSL-CM6A-LR | 2005 | 2036 | 2067 | / |
| MIROC6 | 2027 | 2078 | / | / |
| MPI-ESM1-2-HR | 2015 | 2067 | / | / |
| MPI-ESM1-2-LR | 2017 | 2065 | / | / |
| MRI-ESM2-0 | 2017 | 2051 | / | / |
| NESM3 | 2011 | 2045 | / | / |
| NorESM2-LM | 2033 | 2088 | / | / |
| NorESM2-MM | 2028 | 2078 | / | / |
| TaiESM1 | 2019 | 2043 | 2069 | / |

Table 4.7: Year in which GWLs are reached in the models of the scenario SSP5-8.5, based on 21-year moving average filtered timeseries of GMT anomalies from 1850-1950 average.

| Model | Year GWL +1 °C | Year GWL +2 °C | Year GWL +3 °C | Year GWL +4 °C | Year GWL +5 °C | Year GWL +6 °C |
|------------------|-------------------|-------------------|-------------------|-------------------|-------------------|-------------------|
| ACCESS-CM2 | 2015 | 2039 | 2056 | 2071 | 2085 | / |
| ACCESS-ESM1-5 | 2014 | 2040 | 2061 | 2079 | / | / |
| BCC-CSM2-MR | 2017 | 2044 | 2066 | / | / | / |
| CAMS-CSM1-0 | 2025 | 2062 | 2089 | / | / | / |
| CAS-ESM2-0 | 2019 | 2045 | 2062 | 2078 | / | / |
| CESM2-WACCM | 2009 | 2036 | 2055 | 2069 | 2083 | / |
| CIESM | 2003 | 2033 | 2052 | 2065 | 2077 | 2089 |
| CMCC-CM2-SR5 | 2004 | 2035 | 2054 | 2070 | 2087 | / |
| CMCC-ESM2 | 2007 | 2041 | 2056 | 2071 | 2089 | / |
| CanESM5 | 2002 | 2024 | 2042 | 2056 | 2068 | 2080 |
| E3SM-1-1 | 2015 | 2033 | 2047 | 2059 | 2069 | 2079 |
| EC-Earth3-CC | 1995 | 2038 | 2058 | 2073 | 2086 | / |
| EC-Earth3-Veg-LR | 2011 | 2044 | 2063 | 2077 | / | / |
| EC-Earth3-Veg | 2000 | 2033 | 2054 | 2071 | 2085 | / |
| EC-Earth3 | 2006 | 2034 | 2055 | 2073 | 2087 | / |
| FGOALS-f3-L | 2004 | 2038 | 2061 | 2079 | / | / |
| FGOALS-g3 | 2007 | 2047 | 2074 | / | / | / |
| FIO-ESM-2-0 | 2001 | 2034 | 2056 | 2072 | 2086 | / |
| GFDL-CM4 | 2015 | 2042 | 2060 | 2079 | / | / |
| GFDL-ESM4 | 2026 | 2055 | 2078 | / | / | / |
| INM-CM4-8 | 2017 | 2048 | 2072 | / | / | / |
| INM-CM5-0 | 2020 | 2050 | 2077 | / | / | / |
| IPSL-CM6A-LR | 2005 | 2036 | 2052 | 2068 | 2080 | / |
| MIROC6 | 2026 | 2054 | 2077 | / | / | / |
| MPI-ESM1-2-HR | 2015 | 2052 | 2076 | / | / | / |
| MPI-ESM1-2-LR | 2016 | 2051 | 2073 | / | / | / |
| MRI-ESM2-0 | 2015 | 2040 | 2065 | 2085 | / | / |
| NESM3 | 2010 | 2035 | 2056 | 2073 | / | / |
| NorESM2-LM | 2026 | 2057 | 2078 | / | / | / |
| NorESM2-MM | 2025 | 2054 | 2077 | / | / | / |
| TaiESM1 | 2018 | 2036 | 2052 | 2068 | 2082 | / |

In all scenarios the range of years in which GWLs are reached varies a lot from model to model. Even for the period in which the Earth reaches $\text{GWL} = +1 \text{ }^\circ\text{C}$ compared to the baseline there isn't agreement among models: some of them project it already several years in the past, others in the near future, expressing a large model uncertainty as far as surface temperature is concerned. In SSP1-2.6 no model warms as much as $3 \text{ }^\circ\text{C}$, whereas in SSP2-4.5 just one model – CanESM5, belonging to the cluster of greater normalised NH sea ice decrease – reaches $4 \text{ }^\circ\text{C}$ of global mean temperature warming. In SSP5-8.5 the maximum level to which the Earth is projected to warm within 2089 is $6 \text{ }^\circ\text{C}$, reached by three models.

In order to have a congruous number of models available, the following analyses are conducted at the first four global warming levels, at $+1$, $+2$, $+3$ and $+4 \text{ }^\circ\text{C}$ relative to the historical baseline. Clearly, not for each of the four levels of global warming all of the three scenarios can be taken into account. The maps of the climate variables are computed for more GWLs in order to verify the soundness of the results. One of the advantages of working with GWLs is that this method allows us to use the variables with their real unit of measure, instead of analysing their variations per unit of GMT, which alters the original unit of measure of the variables and could lead to difficulties in the interpretation.

Studying climate variables at levels of global warming implies looking for changes in their spatial patterns being future temperature warming equal across the models. Therefore, another important advantage of this approach is that it enables to go beyond the concept of scenario, by grouping the models together under the same GWL, independently from the scenario they were run. In this way, in the respective year in which models attain a given GWL, they can be put together even if belonging to different scenarios, forming a more numerous ensemble. In fact, as it will be pointed out, in the spatial maps of the variables all the models belonging to the same cluster are taken, from the three scenarios, in the period in which they warm globally of the same temperature, and are averaged together. The possibility of grouping models from the different SSPs under the same global warming level is also supported by the fact that the models belonging to the two clusters are almost the same in the three scenarios, as highlighted before.

The idea at the base of the GWLs is that the climatic situation in the time frame in which the Earth warms up the same is comparable regardless the time passed in that scenario. Coming back to Fig. 4.4, in which the filtered NH sea ice area anomaly is plotted as function of GMT anomaly, it was already remarked that in the scenario SSP5-8.5 the models seem overlapping those of the SSP2-4.5 scenario and then even following their trajectory. This graph supports as well the approach of grouping the same changes in GMT throughout the scenarios. To have another evidence of this, sea ice anomalies at $\text{GWL} = +2 \text{ }^\circ\text{C}$ are compared for all the models in common between the SSP2-4.5 and the SSP5-8.5 scenario. Once again, a scatter plot is produced, in which the values of NH sea ice anomalies compared to 1850-1950 average – from the filtered timeseries – projected by SSP2-4.5 are plotted against those projected by SSP5-8.5, both taken at $\text{GWL} = +2 \text{ }^\circ\text{C}$. For this graphic, all the models of the SSP2-4.5 scenario are employed – all in common with the SSP5-8.5 one – except for CAMS-CSM1-0, the only one that under SSP2-4.5 doesn't reach $+2 \text{ }^\circ\text{C}$ of global warming. This graphic is shown in Fig. 4.7.

The result of the analysis is fundamental: all the models are almost aligned on the regression line, and the value of R^2 equal to 0.93 expresses a highly significant correlation between the values of the two scenarios. It is noteworthy the case of the model TaiESM1, in which the difference

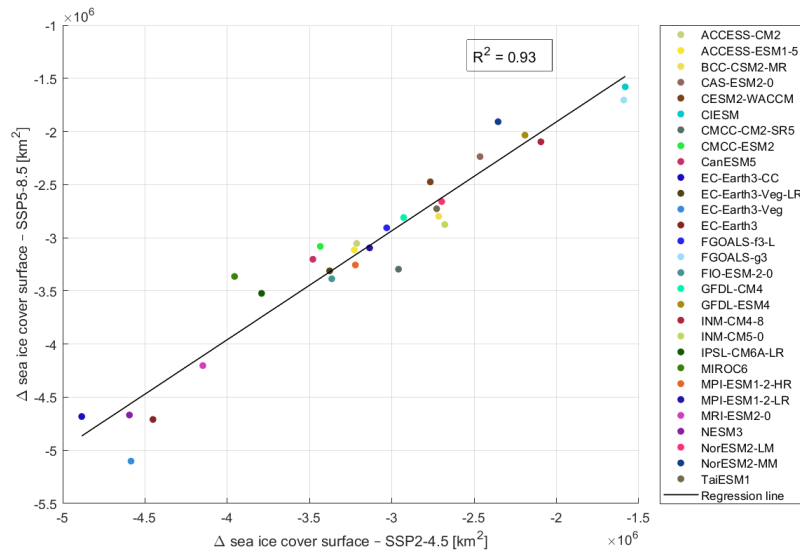


Figure 4.7: Scatter plot of NH sea ice anomalies compared to 1850-1950 average – from the filtered timeseries – at $GWL = +2$ °C: SSP2-4.5 versus SSP5-8.5.

between Arctic sea ice anomalies projected by the two scenarios is just 905 km^2 . The scatter plot verifies that the area of Arctic sea ice at the same level of global warming is similar within the same model in different scenarios; in other words, sea ice response to the same global mean temperature warming is comparable across scenarios. So, this is valid within the same model, independently from how the model simulates the previous period. Therefore, it demonstrates that the approach of GWLs applied to sea ice functions properly: this wasn't to be taken for granted, particularly due to the complex ice-albedo feedback which regulates the mutual response of temperature and sea ice. Thereby, it is proved that there are no relevant hysteresis or instability phenomena in the period prior to the achievement of the same level of warming across scenarios.

Chapter 5

Northern Hemisphere sea ice cover and temperature distributions in the two clusters

After the two clusters of models that project the greater and the smaller changes in Arctic sea ice have been identified, in this chapter they are characterised in terms of spatial patterns of sea ice and temperature. Arctic sea ice and temperature evolutions are analysed together because of their tight correlation, which results in the already illustrated polar amplification effect. For these two variables, since the interest is in the differences in NH sea ice cover projections and on their related differences in temperature, polar maps are analysed, including only latitudes north of 30° N.

The approach followed, adopted even for other climate variables, is to compare the average spatial map of the models belonging to one cluster with that of the models belonging to the other cluster; for the purpose of better appreciating their differences, the difference of the two maps is plotted too. Maps are plotted at levels of global mean temperature warming, until $\text{GWL} = +4\text{ }^{\circ}\text{C}$, so that all the models are taken at the same conditions, globally, of mean temperature anomaly. As with filtered timeseries – in which the values of each cell were weighted for their respective area – the maps of the variables are averaged, for each GWL, over the 21 years centred on the year in which the GWL is achieved. This procedure is applied individually for each model belonging to the two clusters, considering its own years coinciding with the attainment of GWLs compared to its 1850-1950 mean. Then, for each model, from these values the average of the period 1850-1950 is subtracted.

As previously demonstrated, the response of Arctic sea ice to the same global mean temperature warming is almost equal across scenarios. For this reason, by working with GWLs the distinction between scenarios can be overcome: all the models reaching a given GWL are considered together, independently from the scenario, and form an ensemble. In this way, a greater number of models contributes to corroborate the results.

The maps are produced this way for each model; then, they are averaged within their respective clusters of smaller and greater NH sea ice decrease. Thereby, for every GWL until $+4\text{ }^{\circ}\text{C}$ compared to the historical baseline, three maps are produced: one for the cluster of models projecting smaller sea ice decrease, one for the cluster of models projecting greater sea ice decrease and one map of the differences between the previous two, following the convention to subtract the map of the cluster “smaller” from that of the cluster “greater”. Owing to this procedure, by analysing maps as function of GWLs, the differences detected between the two clusters are not attributable to

changes in GMT, which is set equal.

The method just described is applied herein for examining differences in sea ice cover and temperature distributions, but it is the general process followed for the analysis of all climate variables' spatial patterns, unless differently specified.

5.1 Measure of the significance of the results

For every variable, the maps of the difference between the cluster “greater” and “smaller” for the four GWLs must be made more robust by including information about the uncertainty of the results. For this purpose, stippling is plotted over these maps in areas of the planet where detected changes are significant. In this paragraph we explain the method adopted for calculating the significance of the changes identified between the two clusters, applied to the maps of all the climate variables.

In order to assess significance in the differences between clusters, along with the true difference calculated between the clusters of greater and smaller normalised sea ice decrease, a number of differences between fictitious clusters is calculated. To this end, models are randomly picked to form two new fictitious clusters, so that models from the original cluster “smaller” can be grouped with the ones of the cluster “greater” and vice versa. In any global warming level, the number of models in the fictitious clusters is equal, respectively, to that of the two original ones, including all the models from the same cluster that, in any scenario, reach that GWL. Both the fictitious clusters are averaged, and the one with the number of models of the original cluster “smaller” is subtracted from that with the number of models of the original cluster “greater”. This operation is repeated 1000 times for each GWL map, to retrieve a reliable measure of the significance of the calculated differences between clusters. In this way, 1000 matrices of potential maps are created, whose cells of the grid have distinct values of differences. This constitutes the null hypothesis of the significance test, namely that the measured difference between the effects of a cluster of models and the other on a given climate variable is accidental.

Thereby, in every cell of the grid in which the Earth is divided, the 1000 realisations make up a distribution with the shape of a gaussian, having two tails. The significant points of the detected differences between the two clusters of models are the cells in which the signal falls within the lower or higher 2.5% of the distribution, that is to say within the 5% rarest of the distribution. Over the areas where the significance of the detected signal, through this method, results $> 95\%$, stippling is plotted on the original maps of difference between the clusters of greater and smaller Arctic sea ice decrease, with the functions “stipple” and “stipplem” from the Climate Data Toolbox for MATLAB realised by Chad Greene¹ [73].

This methodology is a useful and effective measure of the significance of the results achieved.

¹ For graphical purposes, stippling markers are not plotted on the map for every significant point, but with a lower density, depending on the case.

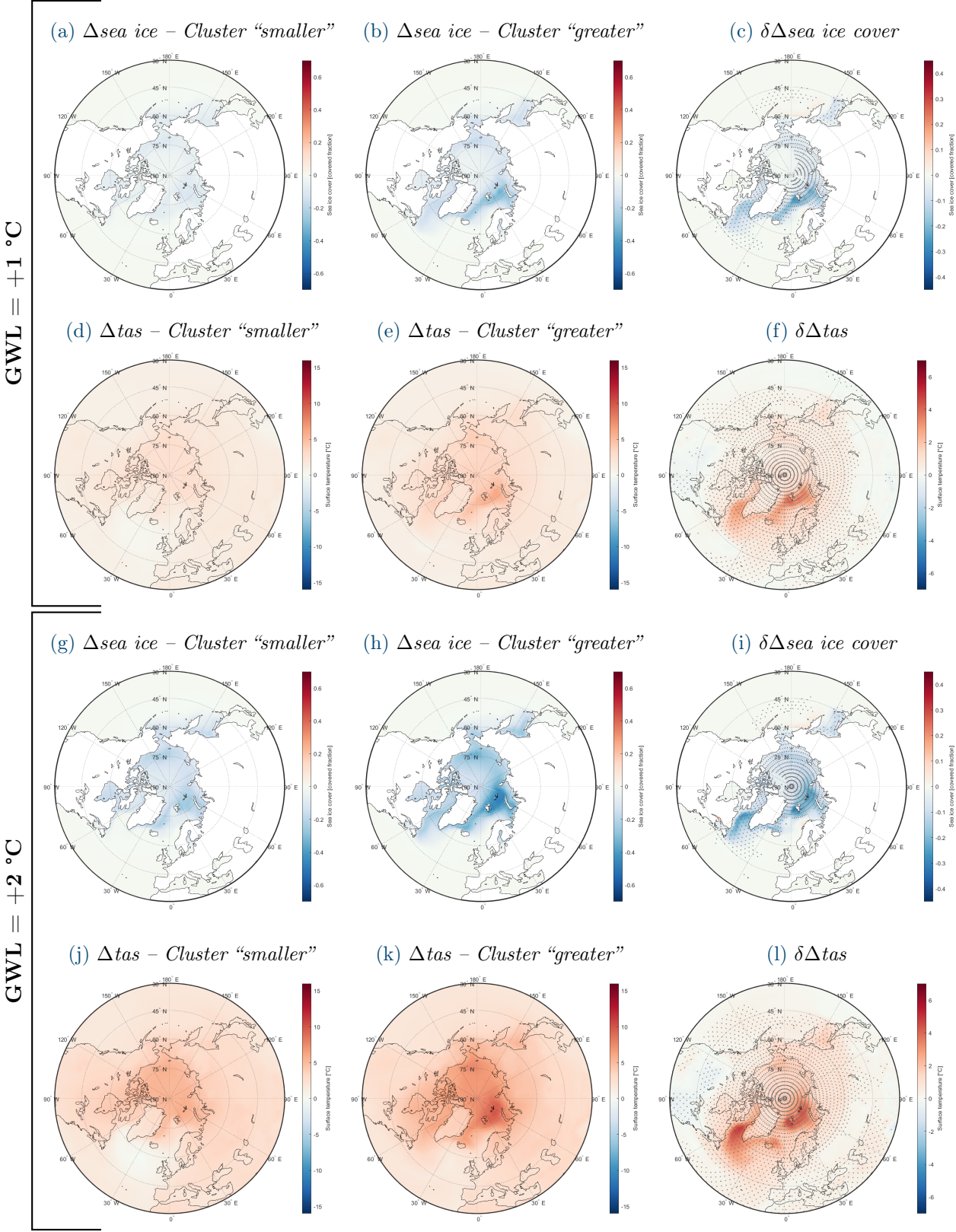
5.2 Sea ice cover distribution

In this paragraph, the maps of Northern Hemisphere projected yearly average sea ice cover distribution in the two clusters of models are reported and analysed, along with their difference (cluster “greater” – cluster “smaller”). Because we are dealing with Arctic sea ice, the maps are plotted for latitudes north of 30° N, with a Lambert azimuthal equal-area projection. As only sea ice is taken into account, ice over the continents is masked, so that land areas in the maps appear in white. Maps show, for the four GWLs, average sea ice anomalies relative to 1850-1950 in the cluster of models with higher sensitivity and in the cluster with lower sensitivity, and their differences. As a convention valid for other climate variables too, the difference between the period of attainment of a GWL and the historical baseline is indicated with Δ before the name of the variable, whereas δ stands for the difference between the two clusters. In other words, Δ expresses differences in time and δ differences between two ensembles.

The aim of these maps is to assess the average change in Arctic sea ice between the two clusters at +1, 2, 3 or 4 °C global warming levels. In Figure 5.1, maps of sea ice cover distribution are reported together with temperature ones, in order to achieve a thorough characterisation of the clusters and to investigate the tight correlation that links sea ice decline and temperature rise in terms of spatial patterns. Note that only in this chapter, for these purposes and for providing an example of the method carried out along the research, maps are displayed for all the four GWLs. On the other hand, when analysing the effects of the different sea ice decrease clusters on other variables, only the more representative levels of global warming will be exposed. Then, interpretations about the clusters’ characterisation in terms of surface temperature distribution are set forth in paragraph 5.3.

Considering the maps of the two clusters themselves, it arises that the greatest sea ice loss will affect northern Barents Sea, in the surroundings of Franz Josef Land, and Greenland Sea; this loss, as expected, is foreseen more markedly by the models of the cluster “greater”. Projected Arctic sea ice decrease in these portions of ocean is impressive for rather high GWLs, with peaks even higher than -70% in annual mean sea ice concentration in models of the cluster “greater” for GWL +4 °C. The fact that the greatest sea ice changes, in particular in the models with highest decrease, are at the edges of the oceanic glacial zones, gives a measure of what will be the extent of ice melting, which will undergo a substantial retreat.

By comparing the maps of the two clusters of models projecting different sea ice area declines, differences between them appear already from the first degree of global warming gained compared to the historical period. Most of the differences in the patterns of sea ice anomalies affect Greenland Sea, encompassed between Iceland and Svalbard, Barents Sea and, especially from GWL +2 °C, the portion of ocean between south-west Greenland and the Labrador Peninsula. In these areas, the differences between the extent of sea ice decrease are more marked between the two clusters compared to other areas, and supported by the 95% significance test up to 4 °C of global warming. On the other hand, in oceanic regions such as the Hudson Bay, a small portion of Barents Sea immediately north of Norway and part of the Bering Sea, models belonging to the cluster “smaller” experience slightly greater decline in sea ice than the others, as well as, for very high global warming, in western Arctic Ocean. Generally speaking, it is reasonable that the difference between sea ice spatial patterns of the two clusters is increasing in extent for increasing global warming



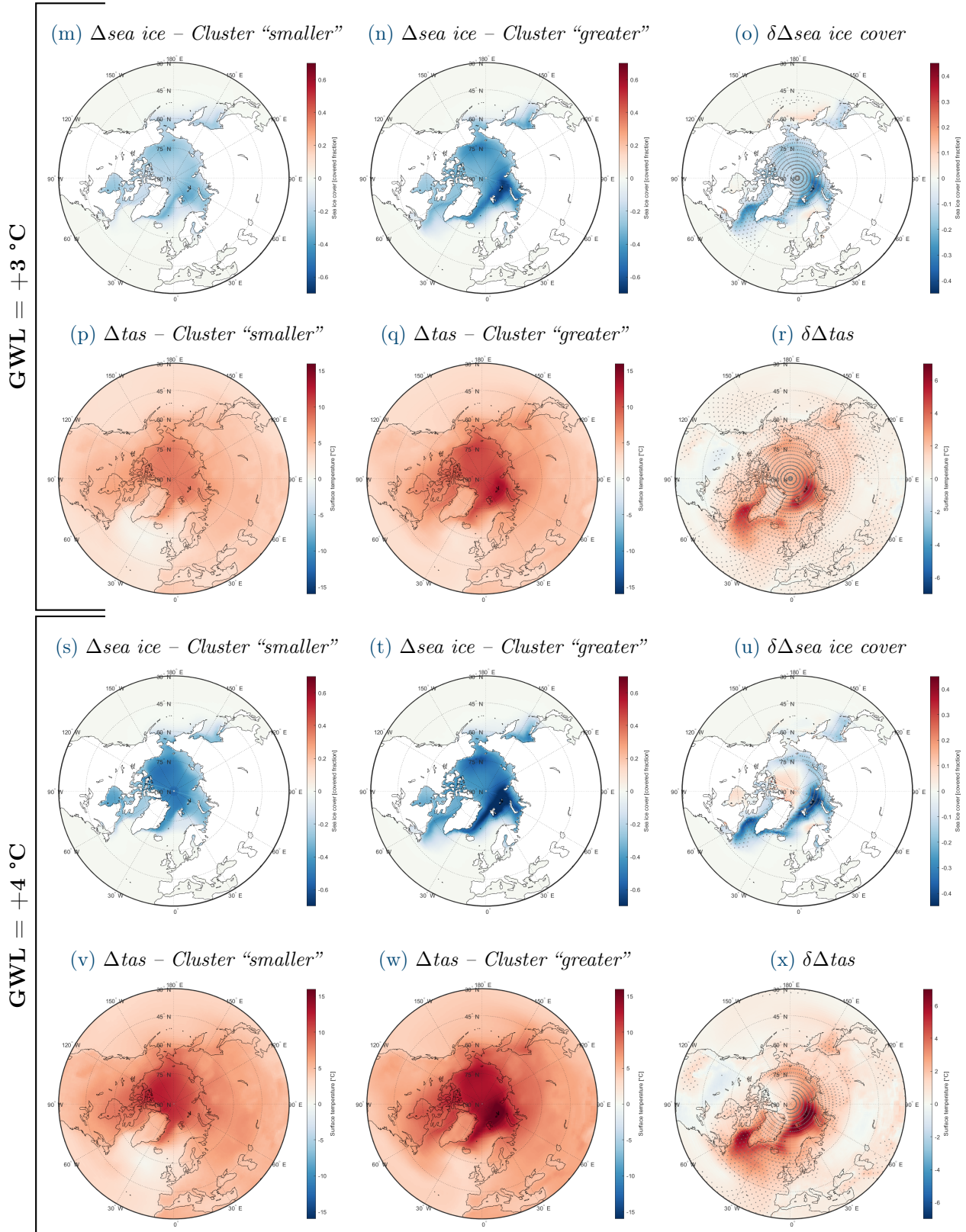


Figure 5.1: Northern Hemisphere maps (for latitudes north of 30° N) of yearly average sea ice cover and surface temperature (*tas*) anomalies relative to 1850-1950 mean (Δ) for the four GWLs. Left: mean of the models of cluster “smaller”; center: mean of the models of cluster “greater”; right: difference between clusters “greater” and “smaller” (δ). Stippling indicates areas where the multi-model ensemble mean response is significant (95% confidence interval).

levels, since the models constituting them have different sensitivities relative to GMT changes. Moreover, the high level of significance obtained for sea ice cover over all the Arctic Ocean in the first three degrees of global temperature warming is an important confirmation that the greatest differences in sea ice among models are indeed those between the two defined clusters.

5.3 Surface temperature distribution

By analysing spatial maps of annual mean surface air temperature (variable named *tas*) we want to identify changes in its patterns in response to the important differences in sea ice cover highlighted between the two clusters, taking into account that all the models are taken at the same level of global mean temperature anomaly. Therefore, the interest is in the characteristics of temperature distribution in two clusters of models that, being the global mean temperature equal, have a very different Arctic sea ice cover.

As a tendency, all temperature maps in the Northern Hemisphere resemble sea ice ones, but with an opposite sign trend. In fact, it is particularly relevant the so tight correlation existing between temperature and sea ice in the Arctic region, underlined by the spatial patterns too. For every GWL, both in the maps of anomalies from the past of the two clusters and in their differences, the distribution of the two variables is practically the same, with shades of red proportional to blue ones in the case of temperature. In other words, the maps of the two climate variables are almost symmetric in sign, meaning that to a given sea ice decrease distribution corresponds a commensurate temperature rise one in the region.

In the maps of the two clusters' anomalies, temperature rise appears extremely stronger over the ocean than on the continents in the Northern Hemisphere, as a direct effect of polar amplification. This result, respectively proportional by increasing the GWL, appears more heavily in the cluster of greater normalised sea ice decline, owing to stronger sea-ice-albedo-feedback in models with higher sensitivities. In fact, while the average of the cluster “smaller” reveals an increase of +8 and +12 °C respectively in the face of +3 and +4 °C globally, almost evenly distributed over the Arctic Ocean, the other cluster projects for those GWLs warming of +12 and +15 °C in the Arctic, with peaks of nearly +17 °C in the surroundings of Franz Josef Land in the case of +4 °C of warming globally. Nevertheless, changes in temperature are not negligible over continental lands, but several degrees lower; still, for the reasons specified, in the cluster “smaller” differences in temperature rise between the Arctic Ocean and the northern continents are far less pronounced than in cluster “greater”.

As for the differences between the maps of the two clusters, they appear more intense exactly on the same areas where differences in sea ice cover appear more intense. Dealing with the ocean, where lie the greatest differences, the portions where they are more marked are Greenland Sea, Barents-Kara Sea and the portion of ocean encompassed between south-west Greenland and the Labrador Peninsula. These diversities in the extent of temperature rise are due to the different sea ice cover between the two clusters of models and classified as significant. They appear clearly already from GWL +1 °C, and grow proportionally throughout the following levels, becoming very substantial – in the order of 7 °C – in the highest considered GWL. Besides, northern continental lands appear more affected by sea ice changes, since northern Canada, Greenland, Scandinavia and Siberia warm up little more in response to greater sea ice loss. It is also interesting to

note that continental Canada, in every level of mean global warming, is undergoing a very slight temperature reduction in the maps of differences between clusters, that could be due to differences in the extent of their sea ice reduction.

The diversities detected in mean annual temperature patterns are therefore the effect of the difference in Arctic sea ice area decline, although global temperature rise is set equal in any model. Furthermore, stippling over the majority of the hemisphere gives confidence that the results are the effect of the different sea ice cover distributions between the models of the two clusters. By analysing four global warming levels the temperature signal has been proved robust, since consistent in all of them. As they are usually conveying the same signal, but with increasing intensity, in the other climate variables studied are not reported maps for every GWL, but just the one or ones deemed more representative.

Chapter 6

Impacts of sea ice decrease on the clusters' global climatology

This chapter presents the results obtained starting from the initial research question that motivated this work, namely the detection of the impacts of the different Arctic sea ice distributions shown by the models throughout this century. Herein we analyse the climatic effects of the projected changes in sea ice cover, aside from the different global mean temperature between the models. To this aim, once defined and described the two clusters in terms of sea ice and temperature distributions in the Arctic region, we characterise their climatology and look for statistically significant differences between them.

Since the interest is in large-scale responses of the climate and on corresponding global impacts, in this chapter global maps are represented. At first surface temperature is analysed at a global scale, together with precipitation; then we delve into distributions of sea level pressure and geopotential height at 500 hPa (Z_{500}). To have a more complete characterisation of the climatology of the two clusters of models, atmospheric circulation is investigated as well, through the study of different future patterns of mean zonal wind and meridional mass streamfunction. The effects on these climate variables are examined on annual, winter (December-January-February) and summer (June-July-August) scales, in order to appreciate seasonal variability too. Lastly, we look for changes in North Atlantic Oscillation (NAO) patterns caused by different sea ice covers, analysed through the Empirical Orthogonal Function (EOF) method.

6.1 Surface temperature distribution

The first sea ice impact analysed at a global scale is the one on near-surface temperature (*tas*), meant as temperature at the height of two meters. Maps of temperature anomalies relative to 1850-1950 average are plotted for both clusters, according to the procedure set out in the previous chapter. Fig. 6.1 shows maps of differences between the clusters “greater” and “smaller” at $\text{GWL} = +3\text{ }^\circ\text{C}$ averaged over different time frames: yearly average, boreal winter (December-January-February, identified with DJF) and boreal summer (June-July-August, identified with JJA). The same figure reports maps of precipitation differences at equal conditions, in order to better identify connected changes between the two variables. The maps are plotted with a Robinson projection, as are all the global maps in this chapter.

From the global scale analysis, it is very interesting to appreciate differences in the distribution

of surface temperature between the two clusters, even though all their models are experiencing the same mean global temperature warming in the maps. In the following, we work through the impacts of sea ice loss on temperature separately based on their temporal scale.

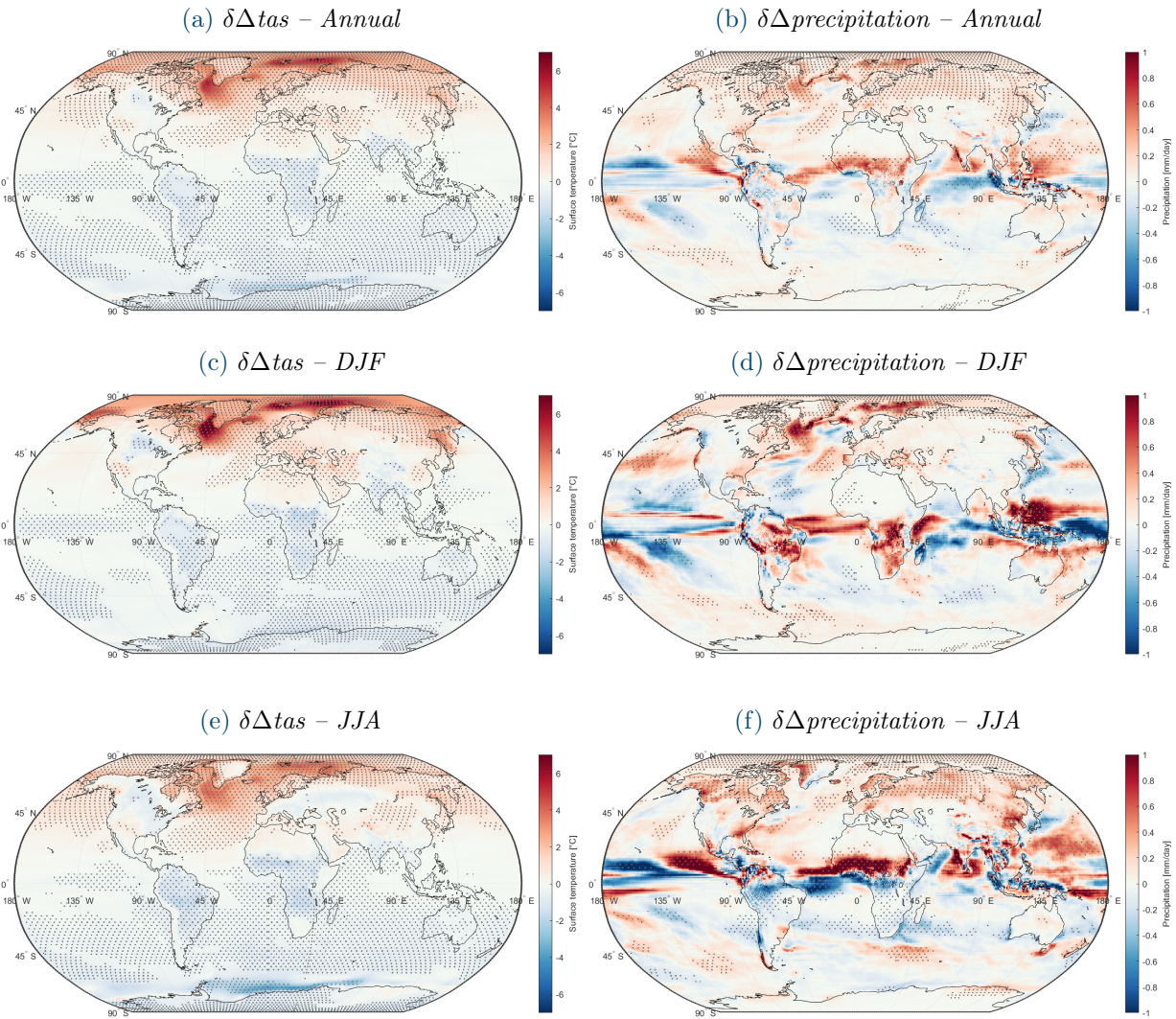


Figure 6.1: Maps of annual, DJF and JJA average surface temperature (tas , left) and precipitation (right) difference between clusters "greater" and "smaller" (δ) for $GWL = +3$ °C. Δ stands for anomalies relative to 1850-1950 mean. Stippling indicates areas where the multi-model ensemble mean response is significant (95% confidence interval).

Annual

Temperature patterns show that, as expected, where sea ice declines most, temperature rise is stronger. In fact, already from $GWL = +1$ °C we observe remarkable differences between the two clusters in polar areas such as Barents Sea, Greenland Sea and Labrador Sea, as previously pointed out, in the order of 3-4 °C. Differences accentuate in the northern polar area for higher GWLs, but southern than NH mid latitudes an opposite sign difference is detected. As a matter of fact, starting from 1 °C of global warming, in almost the entire Southern Hemisphere and in some continental areas of the Northern one, the cluster of models with greater sea ice decrease projects

lower temperature rise than the one in which ice decreases less. In particular, over the continents, this effect appears in continental Canada and eastern United States, in all South America apart from the Andes, in sub-Saharan Africa except the Horn of Africa and South Africa, in India (southern than the Himalayan mountain range), Southeast Asia, Australia and in Antarctica. Therefore, in general, in response to Arctic sea ice decline, Northern Hemisphere is projected to warm up considerably, whereas Southern Hemisphere to cool down. This pattern is reasonable and significant: due to sea ice loss, Arctic regions will get hotter because of the ice-albedo feedback. On the other hand, since the two clusters are experiencing the same global temperature anomaly, in their difference map this temperature increase must be balanced globally, and this occurs mainly in the aforementioned areas.

In the case of annual mean temperature, the maps for the four GWLs represent the same patterns, with a reinforced trend as you increase the GWL. However, differences with negative sign increase in intensity much less than those found at northern latitudes. Besides, detected differences are significant over the majority of the globe until $+3\text{ }^{\circ}\text{C}$ (see stippling in Fig. 6.1a), supporting the soundness of the results. Then, over the annual scale, a greater Arctic sea ice decrease would bring about a softened increase in temperatures in Southern Hemisphere.

DJF

In boreal winter, maps of temperature difference are very similar to the annual ones, showing the same patterns. Yet, the greater ice extension during winter months leads to a stronger polar amplification effect. Hence, in the same GWL, Arctic polar areas warm up even more in the models in which sea ice decrease is more considerable, displaying more intense red hues in the regions highlighted before. As an example, in these areas differences in warming between the two clusters are already in the order of $8\text{ }^{\circ}\text{C}$ at $\text{GWL} = +2\text{ }^{\circ}\text{C}$, then of $9\text{ }^{\circ}\text{C}$ at $\text{GWL} = +3\text{ }^{\circ}\text{C}$ and of almost $11\text{ }^{\circ}\text{C}$ at $\text{GWL} = +4\text{ }^{\circ}\text{C}$ – in this last case the spot appears substantially broadened.

JJA

During boreal summer months, in which sea ice extent is much reduced compared to the other trimester taken into account, the polar amplification effect is much more dampened. Overall, temperature distribution in the maps of differences reproduces the annual and winter ones, as further proof that the identified changes, apart from Arctic ones, constitute a steady tendency within the year, and are not dominated by a specific season. Central Eurasia is an exception, because has a trend of the same – light – order of magnitude, but of opposite sign, represented in blue on the maps.

It can be noticed that South America and in particular the edges of the Antarctic continent appear in a darker blue, meaning that models projecting a more limited NH sea ice decline forecast greater warming in these regions during boreal summer. In other words, during austral winter, models belonging to the cluster “smaller” warm up more than the others in these areas. Given that these differences are more than 95% significant, we can assess that they are ascribable to the different projected distribution of sea ice in the Northern Hemisphere.

6.2 Precipitation distribution

Effects on precipitation have been explored exactly through the same process adopted for surface temperature, so considering its anomalies compared to the historical baseline. The differences in the two clusters' anomalies at $+3$ °C of global warming – taken as representative of the trend – can be appreciated in Fig. 6.1, in the annual, DJF and JJA cases. In fact, even for precipitation, every GWL expresses the same distribution of differences within the same time frame, with changes more intense for higher GWLs. The variable precipitation, as it is defined in the climate models, includes both liquid and solid phases; for convenience, its units are expressed in *mm/day*. Global maps are useful in the case of precipitation to seek large-scale responses, for instance at the Equator, that could be led by variations in the atmospheric circulation. As in the previous case, sea ice decline impacts on precipitation are addressed separately for the three temporal scales.

As far as precipitation is concerned, it is useful to linger on the description of its global patterns and on how it will vary in a climate change context. The uneven distribution of solar radiation over the Earth's surface, for which it is heated stronger at the Equator than at the poles, generates a temperature gradient, which causes atmospheric circulation to transport energy toward the poles. From a zonal perspective, precipitation has a maximum near the Equator, where the average water content of the air is high and tropical convective systems are responsible for much of the rainfall. This heavy precipitation band is known as Inter-Tropical Convergence Zone (ITCZ), where the moisture-laden trade winds converge from either hemisphere. The ITCZ lies at about 5° N and affects mainly Pacific and Atlantic oceans; in this band, formed by high clouds, the moist air is released in thunderstorms, tropical cyclones, and other precipitation-producing weather systems. Secondary precipitation maxima are present in the mid latitudes of both hemispheres. In Northern Hemisphere ones, the precipitation is concentrated near the western margins of the Atlantic ocean, where storm tracks form, whereas in the Southern Hemisphere precipitation in mid latitudes is strong over all longitudes. On the other hand, the entire hydrologic cycle is slowed down in polar regions because of the low temperatures and consequent low water-carrying capacity of the atmosphere, thus precipitation declines [74].

As far as changes in precipitation distribution due to climate change are concerned, they are mainly influenced by changes in the solar radiation-related temperature difference. In fact, those will in turn influence the atmospheric circulation and thus also regional precipitation patterns. According to the IPCC assessment reports, as a general tendency the contrast in precipitation between wet and dry regions and between wet and dry seasons will increase, albeit there could be regional exceptions. Examples of expected changes are decrease in the mean precipitation in many mid-latitude and subtropical dry regions, increase in many mid-latitude wet regions, increase in high-latitudes precipitation and increase in equatorial Pacific Ocean [5]. In all the CMIP6 models adopted in this study, independently from the cluster they belong to, these effects appear clearly from $\text{GWL} = +2$ °C, the strongest of which being by far the increase in equatorial Pacific rainfall. Besides, they all project a decrease in rainfall over the Amazon region and an increase over Central Africa and the northern Indian Ocean. The models forecast a general increase in precipitation over the entire Northern Hemisphere, except from the Mediterranean basin.

Annual

As far as the global impacts on precipitation of NH sea ice decrease are concerned, inferred from the map in Fig. 6.1b, several variations are detected. Greater sea ice loss causes precipitation increase in the North Atlantic, particularly in the Labrador Sea; in this portion of ocean, the result is more than 95% significant until $\text{GWL} +4\text{ }^{\circ}\text{C}$. This effect is consistent with the higher temperature increase due to more robust sea ice loss in that area (polar amplification), as discussed before, which will bring to increased local evaporation. In the inner Arctic Ocean, where the difference in sea ice decline between the two clusters is lighter, there is almost no precipitation increase. Since the clusters of models have been defined on the basis of Arctic sea ice, it is reasonable to note that differences in precipitation patterns affect mostly the Arctic Ocean and the Equator, not Antarctica, which isn't practically influenced. Furthermore, the signal identified in the Arctic is entirely significant, as it is labelled with stippling.

Over the Atlantic Ocean, Arctic sea ice loss is associated with precipitation increases also at the northern tropics. Instead, already from $\text{GWL} = +2\text{ }^{\circ}\text{C}$ can be observed a generalised increase in precipitation over the European continent. From higher levels of global mean temperature rise, it arises that this intensification affects in particular the Italian Alps. Interestingly, a strong precipitation increase is noticed over Central Africa, in the order of $+0.6\text{-}0.8\text{ mm/day}$ on an annual basis for $\text{GWL} +3\text{ }^{\circ}\text{C}$: this signal is present clearly in the models belonging to the cluster "greater" and is absent in the others. Therefore, in the case NH sea ice decreases more, precipitation over that African region increases dramatically; besides, this result is confirmed by the 95% significance test in every GWL .

Overall, a greater change in sea ice cover leads to precipitation increase in the Northern Hemisphere, at the expense of a mean decrease in equatorial precipitation. These differences are likely associated to a change in circulation patterns, discussed in the following paragraphs. In fact, it can be appreciated an impact on the ITCZ as well: this signal doesn't resemble a shift in the ITCZ annual mean band, rather, a reduction in its intensity. However, these differences are not very significant. Some effects on the precipitation pattern are noted also over India, South China Sea and Philippine Sea, but can be better evaluated from seasonal analysis.

DJF

In the boreal winter season, the signal detected over the annual scale on the Arctic Ocean and on Labrador Sea is strengthened, indicating peaks of almost $+1\text{ mm/day}$ for $\text{GWL} = +3\text{ }^{\circ}\text{C}$. The sectors affected by the most marked precipitation increase are Labrador Sea, Greenland Sea and northern Barents-Kara Sea, coinciding with those experiencing the highest winter temperature increase due to sea ice loss. This significant impact reveals the direct link not only between sea ice loss and temperature rise, but also with precipitation, within a series of concatenated effects in the region: due to strong ice-albedo feedback, greater sea ice decline brings temperature to rise more, enhancing local evaporation, which in turn produces more precipitation.

The Atlantic Equatorial sector undergoes strong precipitation increase in DJF, up to 1 mm/day in the GWL considered, confirmed by significance test. On the other hand, the same latitudes on the Pacific Ocean experience less precipitation due to sea ice loss in the NH, in accordance with the average annual trend. Over large part of the Amazon rainforest we notice a very relevant

increase in rainfall in response to greater sea ice decline, as well as in Africa southern than the Equator and in western Indian Ocean. The response over South China Sea and Philippine Sea is statistically significant and very pronounced, even greater than +1 mm/day at GWL +3 °C, explaining the annual signal over the area. There is light positive response over Europe, and almost no response in continental North America, North and Central Africa, and all the Asian continent. Another impact in terms of precipitation increase is on Western United States and the facing ocean; this increase due to sea ice loss was also found by Blackport and Kushner, in a study conducted in 2017 through combined CMIP5 model experiments. The authors point out that this effect appears to be connected with the deepening of the Aleutian low, aspect which will be developed when dealing with sea level pressure distribution. By comparing the response at northern latitudes, with which their research deals, the distribution of precipitation due to sea ice cover decrease appears similar. Blackport and Kushner also state that, when not a direct effect of sea ice through enhanced local temperature and evaporation, changes in precipitation can be linked to the barotropic circulation response to sea ice changes in sea level pressure and Z_{500} [75].

JJA

In boreal summer months, as expected, the effect on precipitation increase over the Arctic due to sea ice loss is far less evident, since also the effect on temperature isn't marked in summer. Overall, summer evolution of precipitation reflects well the annual trend, with more marked changes everywhere worldwide. This suggests that JJA is more representative of the annual trend than DJF.

In the Atlantic Ocean the major effect is observed between the Equator and the northern tropical zone. In particular, two very intense bands appear: one blue, indicating rainfall decrease, over the Equator, and a red one, northern, indicating intensification. The very strong red band expands also over Central Africa, explaining the signal present in the annual map. Therefore, these changes could imply a northern shift of the summer ITCZ over the area, leading to a stronger African monsoon, as an effect of NH sea ice decrease. These changes are also corroborated by the statistical significance test. On the other hand, in the Pacific ocean the effects are multiple. In the central part there is a marked decrease in rainfall in the northern tropical zone, lying over a band indicating increase at the Equator; this would suggest a southward shift of the ITCZ in central Pacific. On the other hand, a strong increase is detected East, close to the American continent, and a bit less marked one in Western Pacific.

All the continental northern latitudes undergo an increase in summer precipitation owing to greater sea ice decline; also the increase over the Italian Alps is driven by summer increase. Lastly, the JJA analysis confirms the rainfall intensification trend over the Indian subcontinent: then, NH sea ice decline can lead to a stronger summer monsoon over India and the surrounding ocean. Higher precipitation levels are detected in this season over the Himalayas too.

6.3 Sea level pressure and geopotential height distributions

In this section, impacts on the distribution of sea level pressure and geopotential height are addressed together, since both represent useful quantities to visualise pressure fields. Air pressure at mean sea level, for simplicity denoted with SLP, is an effective way to describe pressure at any altitude: it is the equivalent pressure of an air particle adiabatically brought to the sea level. It is preferable to surface pressure, which instead is very dependent on the orography of the place where is measured, thus isn't reliable over land areas. On the other hand, geopotential height can be interpreted as an adjustment to the geometric altitude above mean sea level that accounts for the variation of gravity with latitude and altitude. It is a vertical coordinate referenced to the Earth's mean sea level (therefore measured in m) and numerically similar to the altitude (or geometric height) above the geoid, i.e., the reference geopotential surface. From a physical point of view, geopotential is the specific gravitational potential energy relative to the geoid:

$$\Phi(z) = \int_0^z g(\phi, z) dz \quad (6.1)$$

where $g(\phi, z)$ is the acceleration due to gravity, ϕ is latitude and z the geometric elevation. Geopotential height is the geopotential divided by the standard acceleration due to gravity [76] [77]:

$$Z_g(z) = \frac{\Phi(z)}{g_0} = \frac{1}{g_0} \int_0^z g(\phi, z) dz \quad (6.2)$$

where g_0 is the global average of $g(\phi, z)$, approximately equal to 9.81 ms^{-2} . In this study, the geopotential height is taken at 500 hPa: we refer to this variable as Z_{500} . The 500 hPa height field is a useful scalar quantity for characterizing extratropical (e.g. mid-latitude) atmospheric variability. In fact, since 500 hPa is at the mid-point of the mass of the atmosphere, "it captures phenomena that extend through the depth of the troposphere" [78].

Before approaching to the future changes in SLP and Z_{500} fields attributable to sea ice decline, it is convenient to have a brief overview of the main general atmospheric circulation patterns. Most of the persistent high or low pressure patterns, denominated "centres of action", are situated in the Northern Hemisphere, and include:

- **Siberian high:** a dominant area of high pressure forming over Siberia in cold winter months, particularly apparent on mean charts of SLP. This anticyclone is strengthened by the surrounding mountains, and replaced by a low pressure area in boreal summer;
- **Icelandic low:** a low pressure centre located between Iceland and southern Greenland, which can affect the atmospheric circulation in the NH. It is most intense during winter, with a January central pressure even lower than 996 hPa. In summertime, it weakens and tends to split into two centres. It can vary greatly in position and intensity daily;
- **Azores high:** a semipermanent subtropical high (anticyclone) over the eastern part of North Atlantic Ocean, which can influence European weather;
- **Pacific high:** nearly permanent subtropical high of the North Pacific Ocean, having mean centre at $30^\circ\text{-}40^\circ \text{ N}$ and $140^\circ\text{-}150^\circ \text{ W}$;

- **Aleutian low:** a low pressure centre located on the Aleutian Islands – a chain of mainly volcanic island in the North Pacific, extending between the Kamchatka Peninsula and Alaska. It is prevalent in the winter months and, as the Icelandic low, is not stationary and can alternate high and low pressure centres on a daily basis [79].

Maps of differences between mean anomalies of the clusters “greater” and “smaller” for the variables SLP and Z_{500} are plotted on global maps and reported in Fig. 6.2 for $\text{GWL} = +3\text{ }^{\circ}\text{C}$. Because of the important seasonal variability in pressure distribution, highlighted in the description of the centres of action, the average annual, DJF and JJA conditions are analysed.

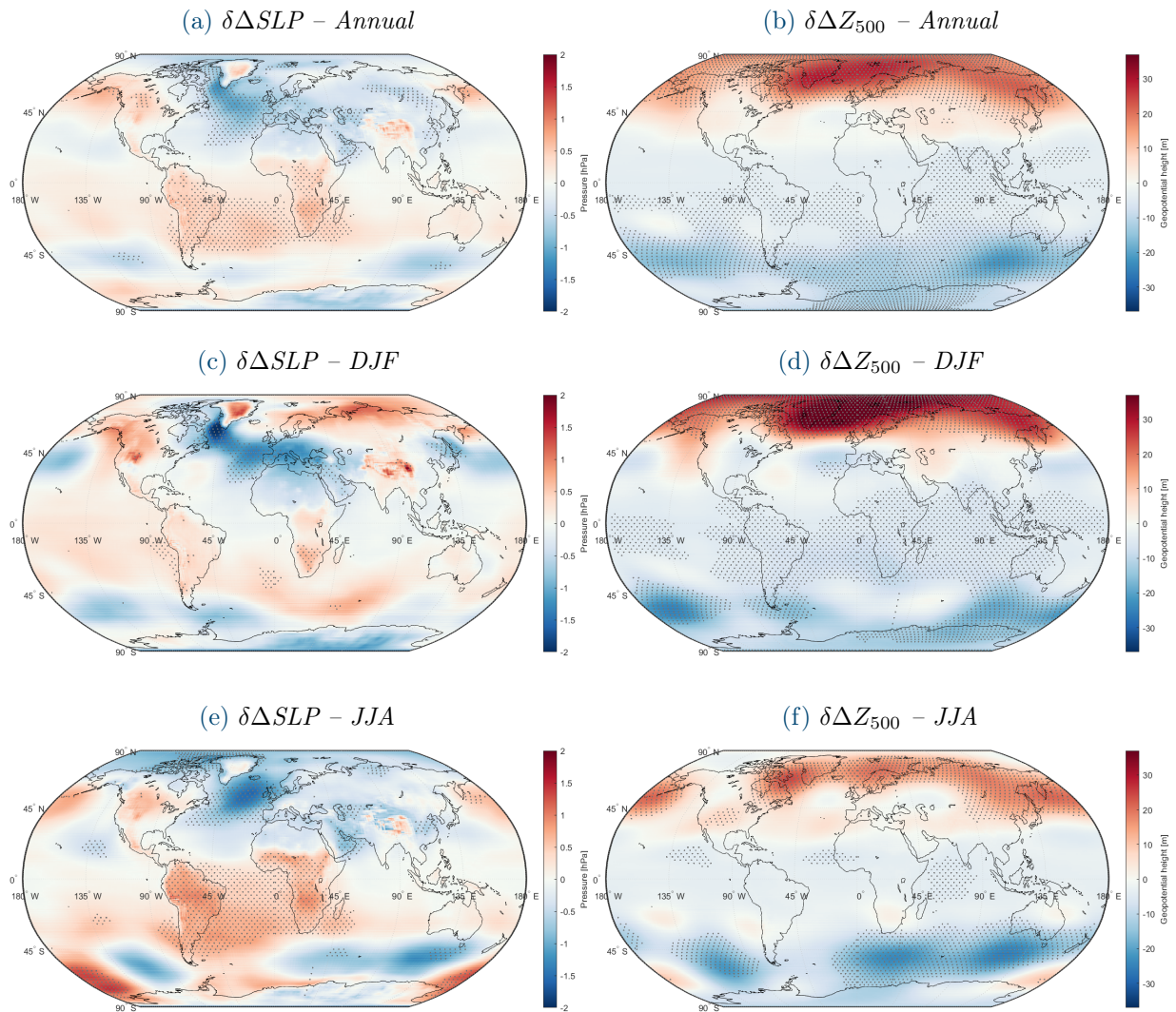


Figure 6.2: Maps of annual, DJF and JJA average sea level pressure (SLP, left) and geopotential height at 500 hPa (Z_{500} , right) difference between clusters “greater” and “smaller” (δ) for $\text{GWL} = +3\text{ }^{\circ}\text{C}$. Δ stands for anomalies relative to 1850-1950 mean. Stippling indicates areas where the multi-model ensemble mean response is significant (95% confidence interval).

Annual

As a general rule, variations in atmospheric pressure are linked to temperature ones: in an open system such as the atmosphere, colder air, which is denser, tends to sink, increasing air pressure. On the other hand, warm air is buoyant because has a lower density due to thermodynamics, thus in its presence atmospheric pressure decreases. From this arises that increase in temperature can lead to pressure lowering, while cooling can enhance the pressure of the air.

By comparing temperature and pressure maps, this mechanism finds confirmation: in general, almost all the regions that are projected to increase in temperature because of sea ice loss will undergo pressure decrease and vice versa, consistent with a thermodynamic heat low response to surface warming. On annual scale, all Eurasia except from India and the Tibetan Plateau, as well as North Africa, will experience pressure decrease. The Americas, sub-Saharan Africa and the Tibetan Plateau, which in the $\delta\Delta t_{as}$ annual map in Fig. 6.1a show a temperature reduction response, are affected by pressure increase. Even inland Greenland, though, is impacted by a SLP rise. As for the oceans, more meaningful responses are in the Atlantic, where two distinct trends are identified: the northern sector has a rather marked decrease response, stronger over the Labrador Sea, while in the south the sign is opposite. Both responses are statistically significant.

Geopotential height is instead linked to surface temperature and pressure. In fact, an increase in temperature over an area leads the air column above it to expand and, following its definition, Z_g to increase. As a consequence, in that case surface pressure would reduce. Geopotential height distribution in the annual case resembles temperature one, but with smoother transitions. The difference in Z_{500} between the two clusters is positive over northern latitudes, with an average increase of more than 25 m over the Arctic, and negative in the Southern Hemisphere. The majority of these differences are statistically significant.

DJF

In the boreal winter season, some changes in the aforementioned centres of actions can be recognised, which could be linked to variations in the atmospheric circulation, addressed in the next paragraph. The map in Fig. 6.2c demonstrates a ridge of high pressure extending from Greenland to Siberia, with low pressure further south. The higher SLP in northern Siberia suggests a strengthening of the Siberian high in these months. Also the North Atlantic reveals very interesting features: the north-eastern sector undergoes a slight increase in sea level pressure, whereas the mid latitudes over the Azores a decrease in SLP, which is statistically significant. This suggests a response that resembles a negative NAO phase, that is, a reduced SLP gradient between the Icelandic low and the Azores high during DJF, as supported by Smith et al. (2022), Cheung et al. (2018) and other studies [61] [80]. However, the strongest winter SLP decrease is the one in Labrador Sea, which also experiences great sea ice decline and consequent air temperature rise. Even over the Mediterranean and the European continent, apart from Scandinavia, the impact is of a SLP reduction, also projected by Blackport and Kushner (2017) and Zappa et al. (2018) [75] [9]. Over the North Pacific, models in which sea ice declines more show a lower pressure than the others, indicating a deepening of the Aleutian low in the future. This impact might result from the indirect effects of sea ice loss on global sea surface temperature (SST) changes [81], not explored in this study, and from the land-sea thermal contrast between the Asian continent and

the Pacific Ocean [82]. Anyway, according to Blackport and Kushner (2017), the more intense Aleutian low could trigger the increase in winter precipitation on the west coast of North America and the facing ocean discussed previously [75].

All the findings related to sea ice loss impacts on the main centres of action are in agreement with many other studies conducted on the influence of sea ice loss on the NH. There is wide consensus on the reinforcement of the Siberian high [61] [9] [80] [83] [75] [48], on the deepening of the Aleutian low [62] [82] [75] [83] [84], on the weakening of the Icelandic low [61] [9] [80] [83] [75], littler on the weakening of the Azores high [61] [80]. However, there is not full understanding of the physical mechanisms driving the sea level pressure response to Arctic sea ice loss, but they probably include changes in baroclinicity and storm tracks [52], planetary wave activity [85].

As far as the geopotential height is concerned, the DJF trend seems to govern the average annual response. In fact, almost all the variations identified on the annual scale are confirmed and intensified in boreal winter months. In particular, all the northern latitudes show a statistically significant increase in Z_{500} , and a less intense one is present on north-western North America and part of Central Asia. All the other areas over the globe project a decrease in Z_{500} , with significance over the tropical zones and where changes have greater magnitude. The geopotential height at 500 hPa increase is striking in boreal winter over all the Arctic, Greenland and Greenland Sea, and differences with the anomalies of cluster “smaller” are in the order of +40-45 m. This effect is caused by deeper tropospheric warming resulting from the reinforced warming of the Arctic Ocean, and is consistent with other studies [9] [84]. Therefore, the impact on Z_{500} is explained by local heating near the surface above sea ice loss areas, propagating upwards and resulting in a thermal expansion of the lower troposphere [84].

JJA

Boreal summer months are usually a rarer matter of research in studies addressing the influence of Arctic sea ice loss on the climate. However, sea ice loss results in a significant cyclonic anomaly over North Atlantic and a general SLP decrease over Eurasia and North Africa. Pressure decrease over the North Atlantic could indicate a weakening of the Azores high, which is semipermanent, extending the DJF trend also during summer months. It is interesting to note that Greenland appears symmetric in colours compared to its pattern retrieved for surface temperature (see map in Fig. 6.1e), for the reasons specified previously. Other features detected from the $\delta\Delta SLP$ map in Fig. 6.2e concern mainly South America, the South Atlantic Ocean and sub-Saharan Africa, whose general pressure increase is regarded as statistically significant.

The Z_{500} map in JJA resembles that of temperature in the same months, detecting an increase in the Arctic regions and on eastern Siberia, even if of much smaller extent than in winter. The response on Southern Hemisphere mid latitudes, on the other hand, has opposite sign. Impacts over the mentioned regions have 95% statistical significance; other areas of the world have practically no impact on Z_{500} in JJA because of NH sea ice decrease.

6.4 Impacts on global atmospheric circulation

In this section are investigated dynamic impacts of future NH sea ice loss on the main aspects related to the global atmospheric circulation. These are namely mean zonal winds, i.e., winds blowing along the latitudinal direction, and mass streamfunction (MSF), which quantifies the strength of the atmospheric circulation and the direction of the flow of air masses. The circulation aspects related to the two variables are explained in the following paragraphs, in which are then exposed the results in terms of impacts derived from the decrease in Arctic sea ice. Since the atmospheric circulation has a great seasonal variability, the DJF and JJA means are calculated, along with the mean over the annual scale. As a matter of fact, it is necessary to separate the winter and summer effects because both wind jets position and the Hadley cells are largely dependent on the season, as will be elucidated.

For convenience, in describing these aspects of the circulation of the atmosphere, zonal average is computed, which is the average over longitude, λ , at a particular latitude and pressure, and is herein represented by an overbar.

$$\bar{x} = \frac{1}{2\pi} \int_0^{2\pi} x d\lambda \quad (6.3)$$

Then, the zonal averages of the annual, DJF and JJA quantities are further averaged over the 21 years centred on the year in which the models reach a given level of global warming, as performed for the other climate variables. Since we look for global scale impacts, zonal averages are computed at all latitudes of either hemisphere. As for the elevation, we focus on changes at the tropospheric level, therefore pressures are considered until 100 hPa, roughly coinciding with the height of the tropopause. For both zonal winds and MSF, the zonal-mean plots have latitude as horizontal coordinate – ranging from 90° S to 90° N – and pressure as vertical coordinate, as a proxy for elevation.

6.4.1 Mean zonal wind patterns

The distribution of the zonal mean of the eastward component of wind, u , through latitude and height, is one of the best-known characterisations of the global atmospheric circulation, and is often called the *zonal mean wind*. In meteorology, winds are called westerly when they flow from west to east and easterly when they flow from east to west. Zonal winds are a dominant feature in the atmospheric circulation, as the zonal-average meridional and vertical components of wind are much weaker than the zonal wind [86].

Fig. 6.3 plots the average annual zonal-mean zonal wind (\bar{u}) distribution computed from the models of both clusters in the historical reference period (1850-1950). Some relevant patterns can be recognised from the global map. The zonal mean wind is westerly through most of the troposphere, with peaks on both hemispheres even greater than 30 m s^{-1} in the subtropical jet stream, centred near 30° of latitude and at an altitude of about 12 km, in the high troposphere. The subtropical jet stream is strongest in the winter season. The zonal winds at the surface are westerly at most latitudes between 30° and 70°, but in the belt between 30° N and 30° S zonal mean easterly surface winds prevail, which take the name of trade winds [86].

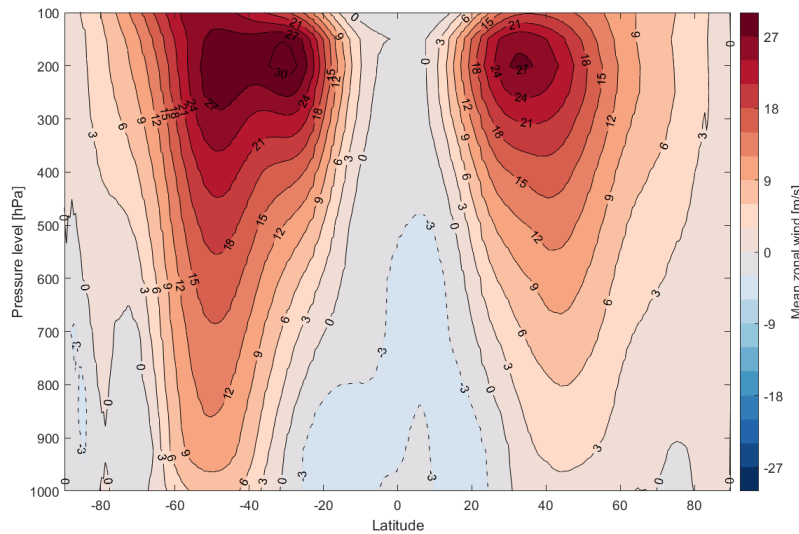


Figure 6.3: Historical average annual zonal-mean zonal wind (\bar{u}) computed from the models of both clusters. Positive (negative) values indicate eastward (westward) direction of the wind speed.

In the following we report the zonal-mean zonal wind plots obtained with the usual approach. In this case, as for the mass streamfunction, are shown the individual maps of the two clusters' mean anomalies for $\text{GWL} + 3^\circ\text{C}$, along with their difference (cluster “greater” – cluster “smaller”). In this way, since winds are vectorial quantities, having all the three maps allows for a better interpretation of the results. The interest is in the research of future Arctic sea ice loss impacts on the circulation of the wind jets.

Annual

Owing to the global climate warming, two main phenomena affect the circulation of zonal winds:

- **tropical upper tropospheric warming:** in tropical latitudes, in the upper troposphere occurs a more intense warming than at surface level, driven by moist convective processes. By its own, this upper tropospheric warming causes the tendency of the mean zonal winds to shift toward the poles. This consequence affects both Southern and Northern Hemispheres;
- **polar amplification:** this phenomenon, already discussed, consists in a stronger warming of the polar regions compared to the other latitudes, in response to the ice-albedo feedback. This effect is in contrast with the one described for the tropics: due to polar amplification, in the Northern (Southern) Hemisphere, wind jets tend to move towards the Equator rather than the North (South) Pole.

The first effect can find validation in particular in the anomalies of the cluster “smaller”, more markedly in the Southern Hemisphere: the intense red band between 45° and 65° S indicates a southern shift of the jet stream, whereas the lighter positive band between 45° and 60° N stands for a northward shift of the NH wind jet. In the other cluster of models, the southern intensification is visible at the same latitudes, but the Northern Hemisphere's one is replaced by negative values.

This occurs because in the cluster “greater” the consequences of polar amplification prevail over the tropical upper tropospheric warming. Therefore, the more temperatures in the Arctic rise due to stronger sea ice dwindling, the more the effect of tropical upper tropospheric warming weakens, and with it the effect of zonal winds shifting northward. The difference between the two clusters in Fig. 6.4c is then consistent, as the impacts are of a general decrease in the strength of zonal winds in the Northern Hemisphere, especially at the high levels of the troposphere. More specific results are obtained from the seasonal analysis.

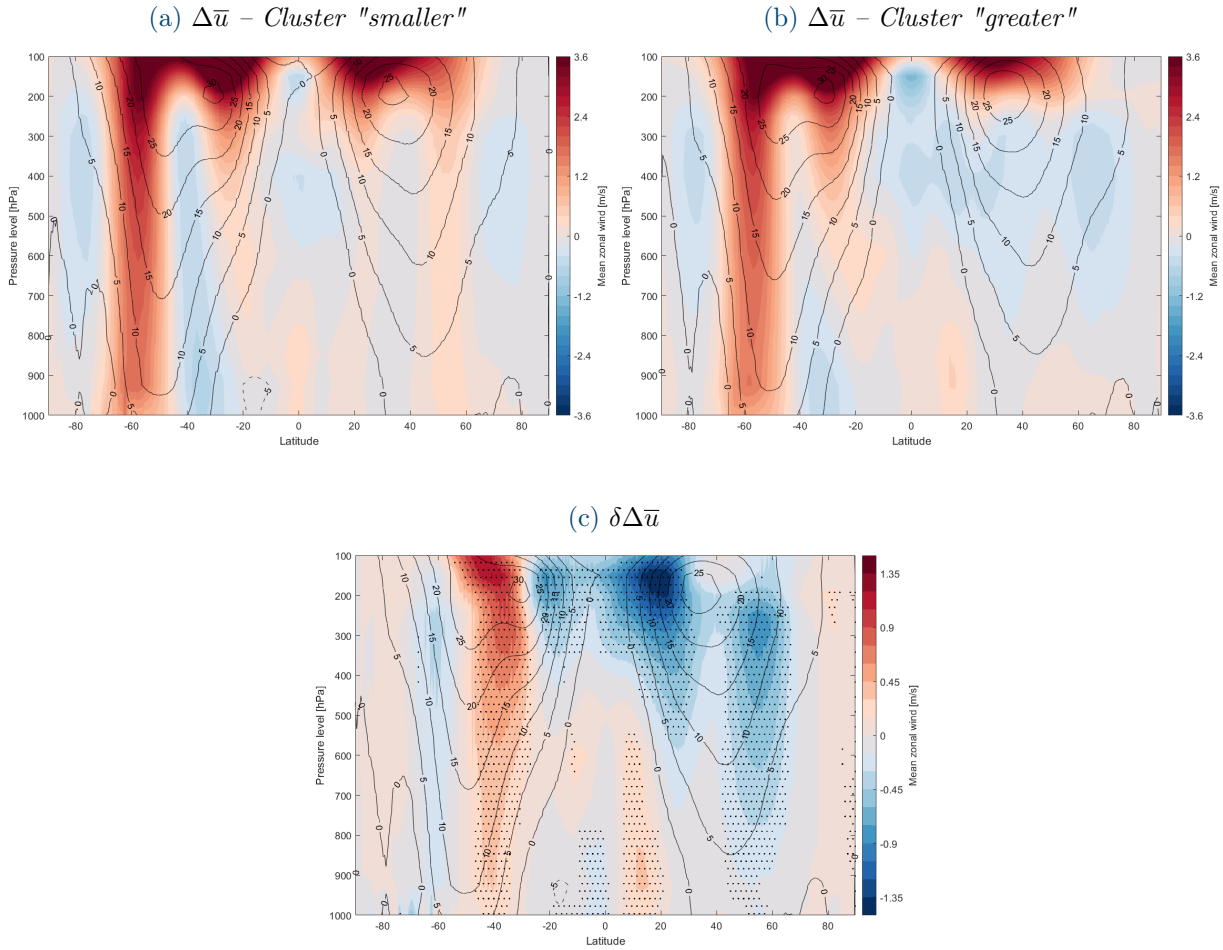


Figure 6.4: Average annual zonal-mean zonal wind (\bar{u}) anomalies relative to 1850-1950 mean (Δ) for $\text{GWL} = +3^\circ\text{C}$. 6.4a: mean of the models of cluster "smaller"; 6.4b: mean of the models of cluster "greater"; 6.4c: difference between clusters "greater" and "smaller" (δ). In panels 6.4a and 6.4b, superimposed contours show the average historical annual zonal-mean wind speed computed from the models of the respective represented cluster; in panel 6.4c, contours show the average historical annual zonal-mean wind speed computed from the models of both clusters. Stippling indicates areas where the multi-model ensemble mean response is significant (95% confidence interval).

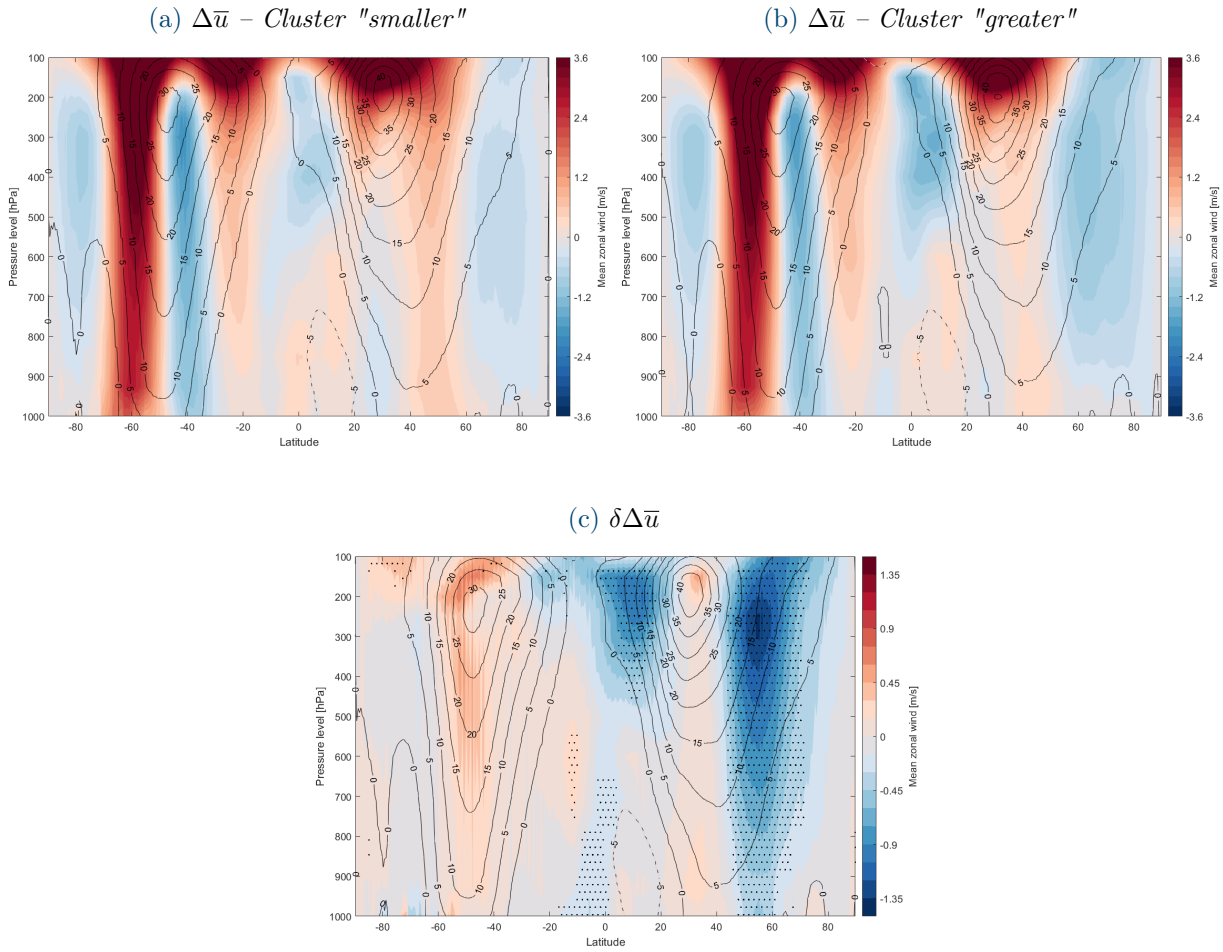


Figure 6.5: Average DJF zonal-mean zonal wind (\bar{u}) anomalies relative to 1850-1950 mean (Δ) for $\text{GWL} = +3^\circ\text{C}$. **6.5a:** mean of the models of cluster "smaller"; **6.5b:** mean of the models of cluster "greater"; **6.5c:** difference between clusters "greater" and "smaller" (δ). In panels **6.5a** and **6.5b**, superimposed contours show the average historical DJF zonal-mean wind speed computed from the models of the respective represented cluster; in panel **6.5c**, contours show the average historical DJF zonal-mean wind speed computed from the models of both clusters. Stippling indicates areas where the multi-model ensemble mean response is significant (95% confidence interval).

DJF

In the boreal winter months, the average zonal mean wind change relative to the historical control period supports the general annual trend and exhibits starker variations; the patterns of the clusters are in line with those demonstrated by Bellomo et al. (2021) for \bar{u} anomalies [71]. Once again, the anomaly in the wind jet is more evident in the Southern Hemisphere than in the northern one in either cluster. The same considerations produced before about the contrasting effects of the tropical upper tropospheric warming and the polar amplification hold.

Looking at the differences between the two clusters, one dominant effect is highlighted as a consequence of the decrease in Arctic sea ice. This consists in a weakening of the northern jet stream, centred at around 55°N . This tropospheric response indicates a weakening of mid-latitude westerly winds in DJF, consistent with many other studies addressing the response of

the atmospheric circulation to NH sea ice decline [61] [9] [75] [84]. In particular, the mean zonal wind difference pattern shown in Fig. 6.5c is coherent with that obtained by Smith et al. (2022) through model projections by PAMIP: this gives confidence of the goodness of the method adopted in isolating the response to future sea ice loss. This impact, which is robustly significant from the 95% statistical test, also suggests an equatorward shift of the storm track developing in boreal winter. This is reported by some research as a repercussion of the decrease in the surface meridional temperature gradient because of the enhanced Arctic warming, via the thermal wind relation [61]. The result is important because proves that Arctic sea ice acts in opposing the poleward shift of the mid-latitude westerly winds – promoted by the strong tropical upper tropospheric warming – which is a common feature of the future projections of atmospheric circulation change, detectable in particular in Fig. 6.5a. Furthermore, if enlarging the analysis to higher elevations (i.e., lower pressure levels) – not shown in these plots – the blue band detected at mid latitudes extends to high northern latitudes, indicating that sea ice loss is associated with a weakening of the stratospheric polar vortex, as confirmed by other researchers [61] [75].

6.4.1.1 Northern Hemisphere 850-hPa zonal wind distribution

Since the weakening of the mid-latitude westerly circulation affects the whole troposphere from approximately 50° to 70° N, it is interesting to investigate, in the winter months, if this phenomenon as a response to sea ice loss is detectable across all the longitudes in that band or more intensely on specific areas. In fact, as the zonal-mean plots are averaged over all the longitudes, information about differences between regions at the same latitudes is not expressed. Therefore, we plot the DJF impacts on the zonal wind at 850 hPa (u_{850}) – the surface level jet stream – in the NH, for latitudes north of 20° N. The map for GWL +3 °C can be appreciated in Fig. 6.6a: the blue band can be clearly recognised as a ring of zonal speed decrease affecting approximately the aforementioned latitudes. The spatial map, which represents a horizontal section at 850 hPa of the previous $\delta\Delta\bar{u}$ graphic, proves that in the northern mid latitudes, winds in the cluster “greater”, in which the polar amplification effect is more evident, are weaker than in cluster “smaller” across the globe. These differences among models, representing the same mean level of global warming, exceed 1 m s^{-1} over some regions, and are caused by diversities in the extent of Arctic sea ice decrease, supported by 95% statistical significance too.

The same map of the effects of NH sea ice cover decline on u_{850} is reported for comparison from a work on the same matter of research by Zappa et al. (2018), even if representing late winter situation (January-February-March, JFM) [9]. The resemblance, although a one-month shift, is striking: all the areas of the NH where the computed differences have high statistical significance correspond, as well as the general u_{850} distribution over the considered latitudes. Both the spatial maps show a weakening of the westerly flow at latitudes comprised between around 45° and 65° N, strongest in the North Atlantic sector, together with a slight, and less robust, strengthening further south in the oceanic basins. The ring of westerly winds weakening affects all longitudes except western North America, where the effect is much lighter. Besides, the red band at lower latitudes, indicating an increase in the surface zonal wind speed, confirms the southward displacement of the jet stream, more intense on both the Atlantic and Pacific oceans. These results are crucial in determining the role of the massive Arctic sea ice loss in modifying

the atmospheric circulation response to climate change, at least in boreal winter.

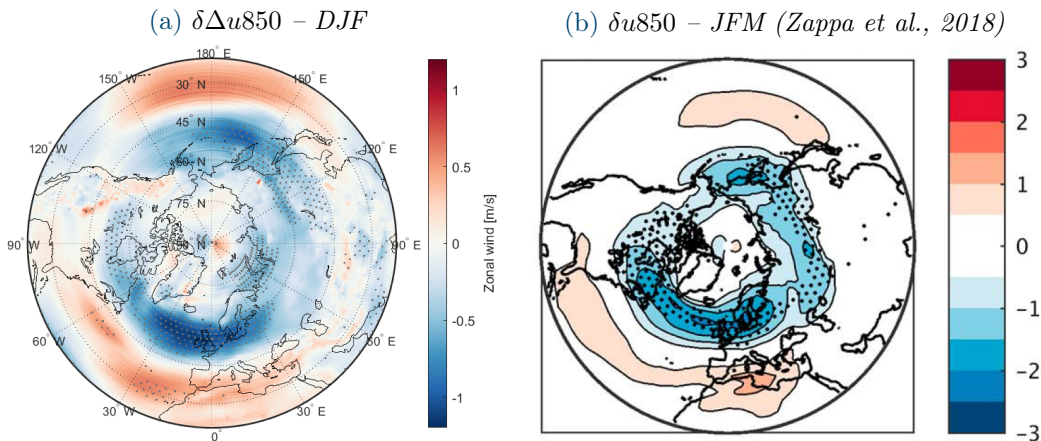


Figure 6.6: Northern Hemisphere maps (for latitudes north of 20° N) of **6.6a**: DJF average zonal wind at 850 hPa (u_{850}) difference between clusters "greater" and "smaller" (δ) for $\text{GWL} = +3^\circ\text{C}$. Δ stands for anomalies relative to 1850-1950 mean. Stippling indicates areas where the multi-model ensemble mean response is significant (95% confidence interval); **6.6b** (from Zappa et al., 2018 [9]): late winter (JFM) CMIP5 mean response (10-model subset) in zonal wind at 850 hPa (u_{850} , m s^{-1}) computed as difference between the RCP8.5 scenario and AMIPsst+co2. Stippling indicates areas where the response has the same sign in at least 90% of the models.

JJA

In boreal summer, the maps of the two clusters' anomalies point out a far lighter effect of shifting the subtropical jet stream to the poles driven by the tropical upper tropospheric warming. Both clusters demonstrate a tendency of climate change to weaken the subtropical jet stream, which in summer is already less strong than in the winter season. Looking at the zonal map of the differences in Fig. 6.7c, the extent of this change doesn't appear much diverse in those latitudes and at those heights, being just slightly more accentuated in the cluster "greater". On the other hand, the contours of either cluster – displaying the respective historical mean JJA \bar{u} – show an easterly jet stream in the troposphere above the tropical latitudes around the Equator. This pattern represents the ITCZ flow, which prevails in the months of the boreal summer. The difference between the clusters in these latitudes is notable: in the upper levels of the troposphere, models with the largest decrease in sea ice project a stark reduction in the zonal wind speed, with peaks lower than -2 m s^{-1} at latitudes where the ITCZ lies in this season. Another marked change is the strengthening of the wind currents at northern polar latitudes, with centre at about 80° N. As for the Southern Hemisphere, an effect consistent with the mechanisms exposed previously can be detected. In fact, the very intense red band centred on 40° S is an implication of the tropical upper tropospheric warming, which now prevails in the cluster of greater sea ice decline because of the much weaker contribution by the polar amplification during summer months, as already pointed out. This last contribution during JJA appears to drive the overall annual tendency of zonal mean impacts on the annual scale. All the mentioned changes are statistically significant, proving that they are led by the projected loss of sea ice in the NH.

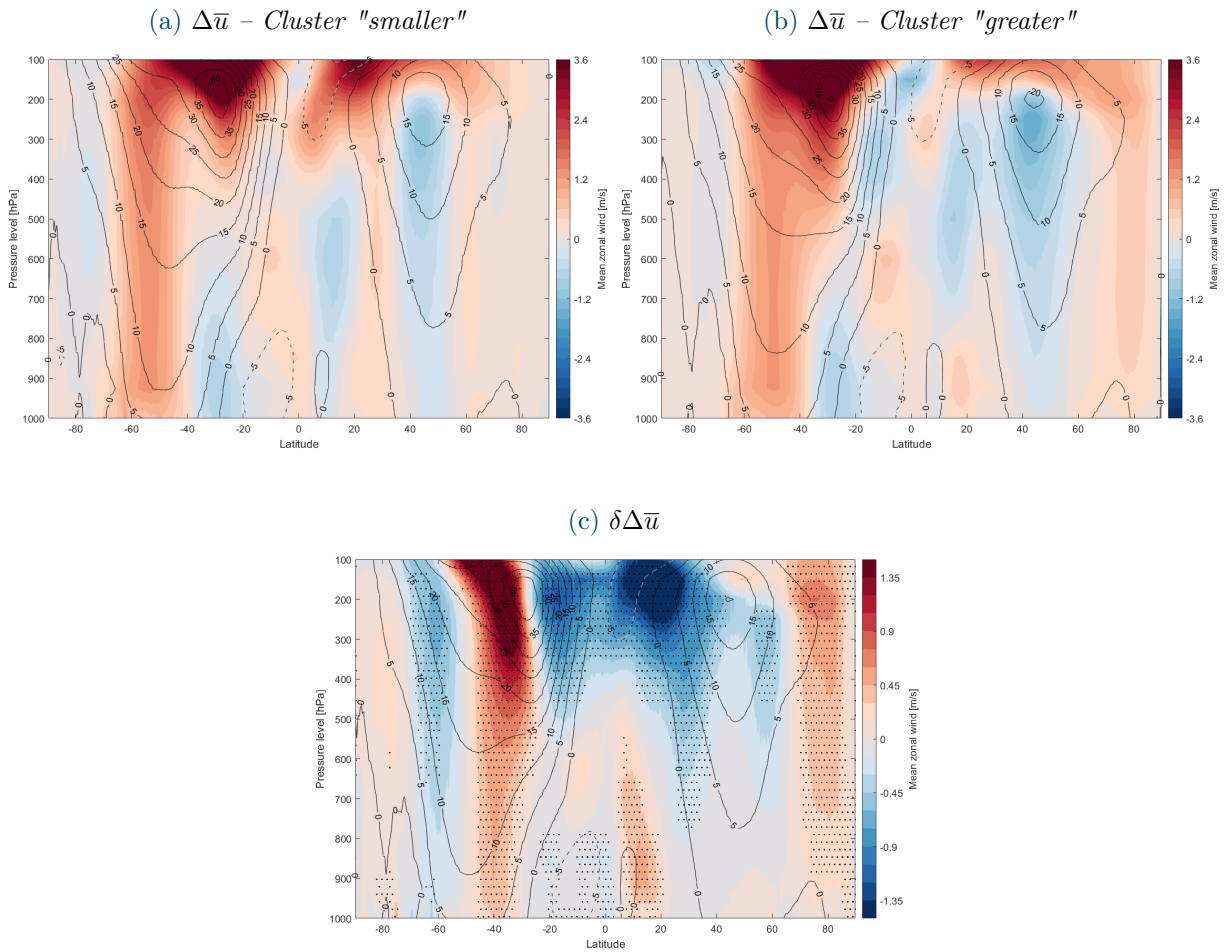


Figure 6.7: Average JJA zonal-mean zonal wind (\bar{u}) anomalies relative to 1850-1950 mean (Δ) for $\text{GWL} = +3^\circ\text{C}$. 6.7a: mean of the models of cluster "smaller"; 6.7b: mean of the models of cluster "greater"; 6.7c: difference between clusters "greater" and "smaller" (δ). In panels 6.7a and 6.7b, superimposed contours show the average historical JJA zonal-mean wind speed computed from the models of the respective represented cluster; in panel 6.7c, contours show the average historical JJA zonal-mean wind speed computed from the models of both clusters. Stippling indicates areas where the multi-model ensemble mean response is significant (95% confidence interval).

6.4.2 Changes in the meridional mass streamfunction

We stated previously that the meridional and vertical components of the wind velocity are much weaker than the zonal component, responsible for the jets, respectively of one and three orders of magnitude. However, the zonal mean meridional and vertical velocities are crucial for the atmospheric circulation too, since give rise to the *mean meridional circulation* (MMC). The MMC is described by a mass streamfunction (MSF), which is defined by calculating the northward mass flux above a particular pressure level, p . The MSF measures the air mass transport through a vertical integral, at a particular latitude, of the zonal-mean meridional velocities \bar{v} :

$$\Psi_M = \frac{2\pi a \cos \phi}{g} \int_{p_0}^p \bar{v} dp \quad (6.4)$$

being a the radius of Earth and p_0 the surface pressure. The mass flow between any two streamlines of the mean meridional streamfunction, measured in $kg\ s^{-1}$, is equal to the difference in the streamfunction values [86]. The meridional MSF, as the zonal winds, is visualised through vertical cross sections, function of latitude and pressure.

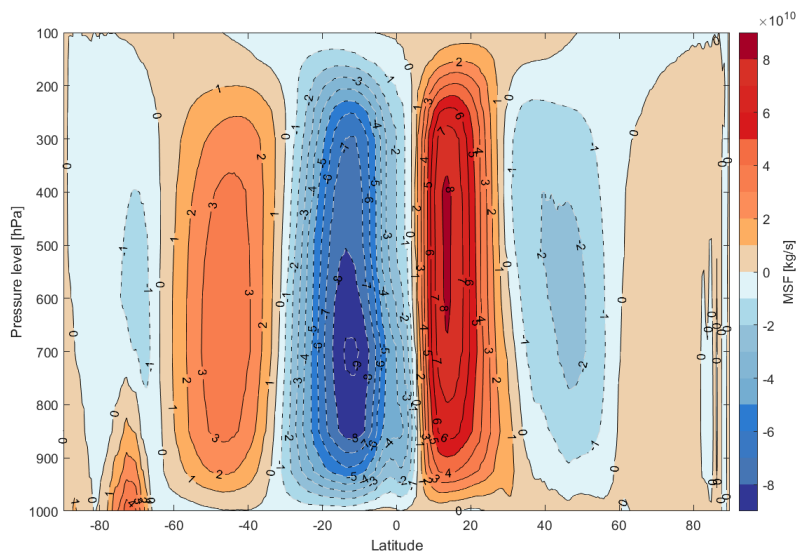


Figure 6.8: Historical average annual meridional mass streamfunction (MSF) computed from the models of both clusters. Positive (negative) values indicate air masses clockwise (anti-clockwise) rotation.

In Fig. 6.8 is reported the cross section of the historical average annual MSF, computed using the models belonging to both clusters, for all latitudes, in order to visualise the full MMC¹. Mean meridional circulation is a system of air cells rotating clockwise or anti-clockwise in the troposphere, depending on the season. The atmospheric meridional circulation, and in particular the Hadley cell, influences regional climates and controls the global distribution of precipitation, clouds and humidity. This occurs because it not only transports warm air, which rises, but also moistened air in its lower limb. The Hadley cell is the single circulation cell which dominates the MMC in the solstitial seasons: near the Equator, heated air masses rise, then flow toward the

¹ For the computation of the MSF, Eq. 6.4 is implemented through the "mastrfu" function by CDO (<https://code.mpimet.mpg.de/projects/cdo/>), applied on time averages of zonal-mean meridional velocities \bar{v} .

winter hemisphere at upper levels, underneath the tropopause. In its motion, air progressively cools down, and sinks in the subtropical latitudes of the winter hemisphere, at about 30° . Then, the air is blown back toward the Equator by the mean meridional winds near the surface. The upward branch of the Hadley cell occurs in the summer hemisphere during the solstitial seasons. As can be appreciated from the plot, in the annual mean, the rising branch is positioned slightly north of the Equator, and the Hadley cell in the Southern Hemisphere is stronger. This asymmetry corresponds to a weak transport of energy from the Northern to the Southern Hemisphere. Moreover, the mean northward displacement of the rising branch of the cell affects the positioning of the ITCZ, which in fact is – on average – located around 5° N. The ITCZ forms from the trade winds blowing in the lower limb of the Hadley cell, which transport dry air that absorbs moisture while approaching the Equator.

Other cells compose the MMC system: these are the Ferrel cells, weaker cells that circulate in the mid latitudes in the opposite direction to the Hadley cell. This implies that the rising branch lifts cold air, which sinks as warmer air. Since they transport energy from a cold area to a warm one, these cells are thermodynamically indirect. As the historical cross section proves, the Ferrel cell in the Southern Hemisphere is stronger in the annual mean, because it persists in all seasons, whereas the NH one is present only in boreal winter [86].

In the following we evaluate the dynamic impacts on the meridional circulation cells on annual, DJF and JJA averages, thereby achieving a rather broad picture of the changes driven by pan-Arctic sea ice decline on the main aspects of the climate. As usual, global warming level $+3^\circ\text{C}$ is taken as representative of the tendency of the impacts; meridional MSF cross sections are reported for the anomalies of cluster “greater” and “smaller” and for differences between the two at a global scale, so encompassing all latitudes.

Annual

From the two clusters' anomalies in Figures 6.9a and 6.9b we can detect some common features simulated by all the models as consequences of the climate change. The global mean temperature warming, amplified at the poles, will cause the meridional temperature gradient between the Equator and the poles to decrease. For this reason, for the MMC cells will be possible to extend to latitudes that in the future climate will become warmer, that is, respectively northward and southward in the Northern and Southern Hemispheres [87]. The expansion toward higher latitudes can be identified in both the anomalies plots, in which shades of red indicate increase in the case of clockwise circulation and blue shades indicate strengthening of the anti-clockwise circulation cells. In particular, the annual average Hadley cell of both hemispheres expands toward the poles, as well as either Ferrel cell, although more robustly in the southern one, since present in any month.

To have a better understanding of the mechanisms underpinning changes in the meridional circulation, it is useful to bring an opposite example, related to experiments simulating a collapse of the Atlantic meridional overturning circulation (AMOC). Those simulations exhibit a glaciation, mostly in the NH, so, in a way, an opposite situation to the one studied herein. In that case, the stark reduction in temperatures at high latitudes leads to a southward shift of the NH Hadley cell. This occurs, in those experiments, because a decline in the strength of the AMOC decreases

the heat transport from the tropics to the NH. A lower heat transport through the thermohaline circulation of the ocean gets therefore compensated by increased transport by the Hadley cell [88]. This case can be extended to the general situation in which a cooling at the poles takes place: the Hadley cell shifts equatorward and strengthens in order to compensate for the lack of heat at the poles. In the occurrence of NH cooling, the Hadley cell acts by carrying more heat from Southern to Northern Hemisphere.

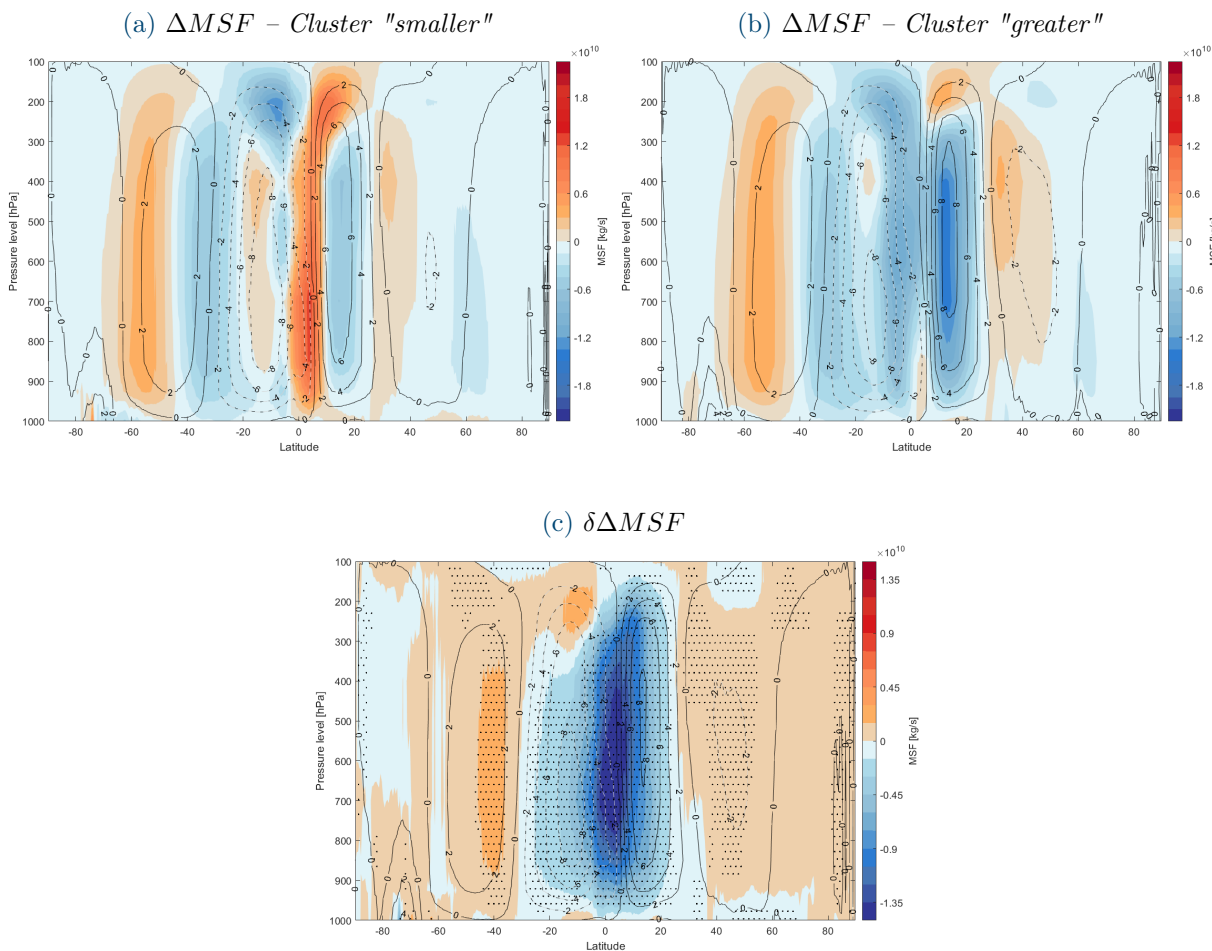


Figure 6.9: Average annual meridional mass streamfunction (MSF) anomalies relative to 1850-1950 mean (Δ) for $\text{GWL} = +3^\circ\text{C}$. **6.9a:** mean of the models of cluster "smaller"; **6.9b:** mean of the models of cluster "greater"; **6.9c:** difference between clusters "greater" and "smaller" (δ). In panels **6.9a** and **6.9b**, superimposed contours show the average historical annual MSF computed from the models of the respective represented cluster; in panel **6.9c**, contours show the average historical annual MSF computed from the models of both clusters (contour interval is $2 \times 10^{10} \text{ kg s}^{-1}$). Stippling indicates areas where the multi-model ensemble mean response is significant (95% confidence interval).

The effect demonstrated by this study is exactly the opposite. Since the models with greater sea ice decline are those that warm most at the North Pole, the Hadley cell doesn't transport additional energy, rather, it generally weakens in order to compensate for the increased warming and for the reduced Equator-pole temperature gradient. In fact, as for the strength of the atmospheric transport, the NH mean annual Hadley cell weakens more in the cluster "greater" than in the other.

Owing to the higher polar amplification, and consequent more uniform temperatures meridionally, in the models of greater sea ice decrease the cell expands more poleward and, due to conservation of energy, undergoes a strength loss. On annual average, the northern Hadley cell is projected to extend up to about 50° N in the cluster "greater" and up to around 45° N in the "smaller". The southern Hadley cell, on the other hand, weakens and shifts southward more in the models of cluster "smaller". This effect is less evident in the other cluster: therefore, sea ice loss has an opposing impact on this phenomenon. It is remarkable that all the findings presented are made more robust by higher than 95% statistical significance.

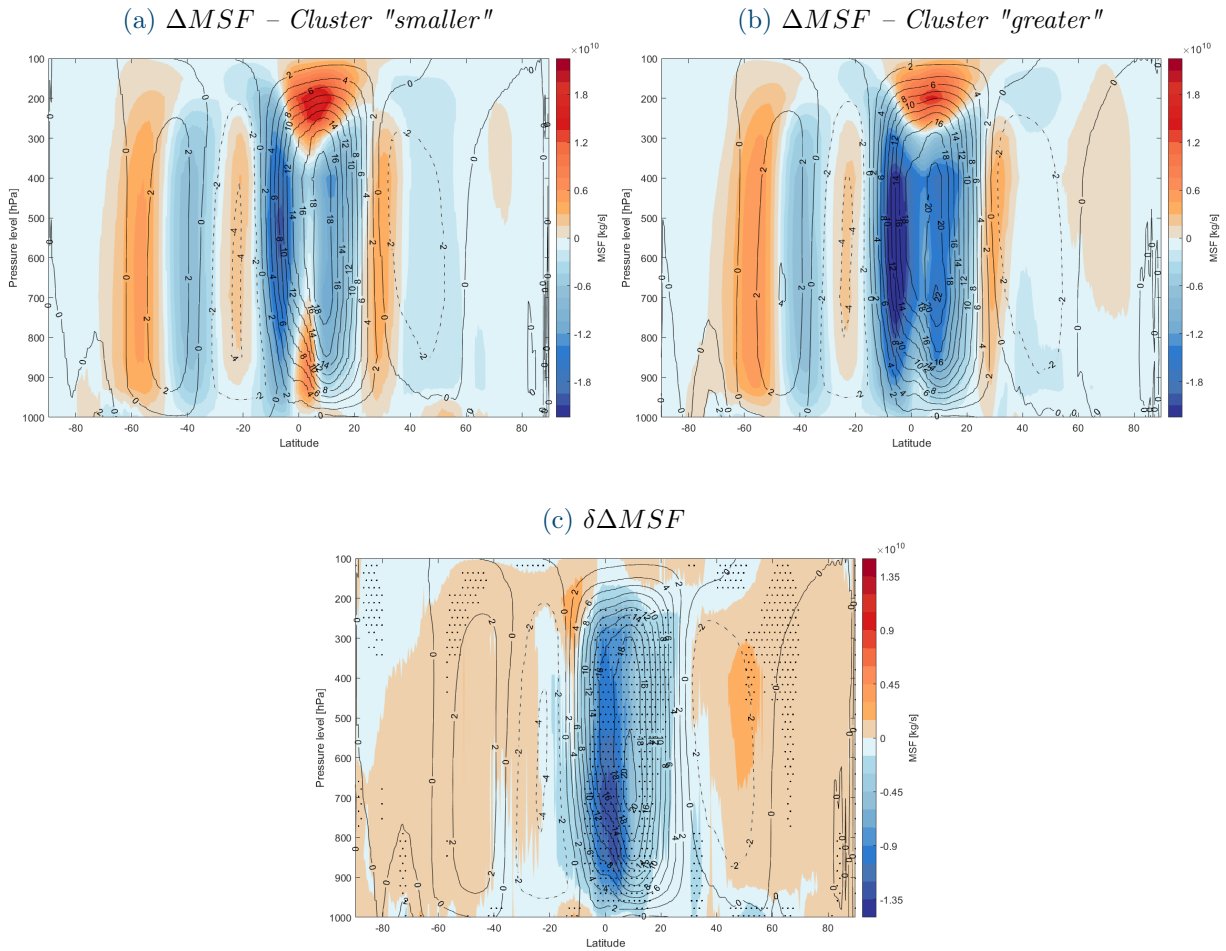


Figure 6.10: Average DJF meridional mass streamfunction (MSF) anomalies relative to 1850-1950 mean (Δ) for $GWL = +3^\circ\text{C}$. **6.10a**: mean of the models of cluster "smaller"; **6.10b**: mean of the models of cluster "greater"; **6.10c**: difference between clusters "greater" and "smaller" (δ). In panels **6.10a** and **6.10b**, superimposed contours show the average historical DJF MSF computed from the models of the respective represented cluster; in panel **6.10c**, contours show the average historical DJF MSF computed from the models of both clusters (contour interval is $2 \times 10^{10} \text{ kg s}^{-1}$). Stippling indicates areas where the multi-model ensemble mean response is significant (95% confidence interval).

DJF

The impacts recognised in the average annual MSF are confirmed by the seasonal analysis. The DJF Hadley cell, transporting energy from Southern to Northern Hemisphere, is substantially weakened in the case of greater sea ice loss. The patterns of both clusters demonstrate that on average, the boreal winter Hadley cell will decrease in strength due to future warming, because it won't be as necessary as in the control period to transport heat to the warmer NH, as previously stated. Anyway, the impact due to Arctic sea ice decrease is dominant over this effect, mostly in the first degrees north, as proved by stippling in Fig. 6.10c. All the models project a northward shift of the cell too. These impacts imply a weakening of the tropospheric circulation and a decrease in the poleward transport of heat and energy in this season. Also the Ferrel cell, which has the opposite direction compared to the Hadley one, results weakened by larger sea ice loss. This reduction in the strength of the Ferrel cell is consistent with the identified weakening of the mid-latitude westerly winds in DJF. All the results discussed are identified also by two research papers by Cheung et al. (2018 and 2022), whose MSF pattern in boreal winter looks very similar [80] [62].

JJA

In the boreal summer season, the same mechanisms highlighted previously hold and are, once more, in line with the annual trend. In any model the transport to the Southern Hemisphere is decreased in response to the lower temperature gradient in the meridional direction; however, this effect is much more marked in the models belonging to the cluster "smaller", particularly on the northern ascending branch of the Hadley cell. This is again explained by the difference in the extent of temperature rise in the NH between the two clusters in JJA – when Arctic sea ice shrinks toward its annual minimum – owing to the starker polar amplification of models with greater decrease, as recognised from Fig. 6.1e. Hence, as models projecting lower sea ice cover change warm less in the NH, they will have a lower temperature gradient between this hemisphere and the austral winter one, thus reducing the need for heat transport southward. A warmer NH, represented by the models of the cluster "greater", will have instead more excess of heat, which has to be displaced to the Southern Hemisphere. For this reason, in the face of a generally decreased meridional temperature gradient (the warming is globally the same among models), a more severe Arctic ice loss causes a dampening of the weakening effect of the JJA Hadley cell. Besides, as a response to the described impact on the Hadley cell, the Southern Hemisphere Ferrel cell compensates by strengthening more in the models with greater Arctic sea ice loss, for the energy balance. All the impacts identified are corroborated by 95% significance test, as visible from Fig. 6.11c.

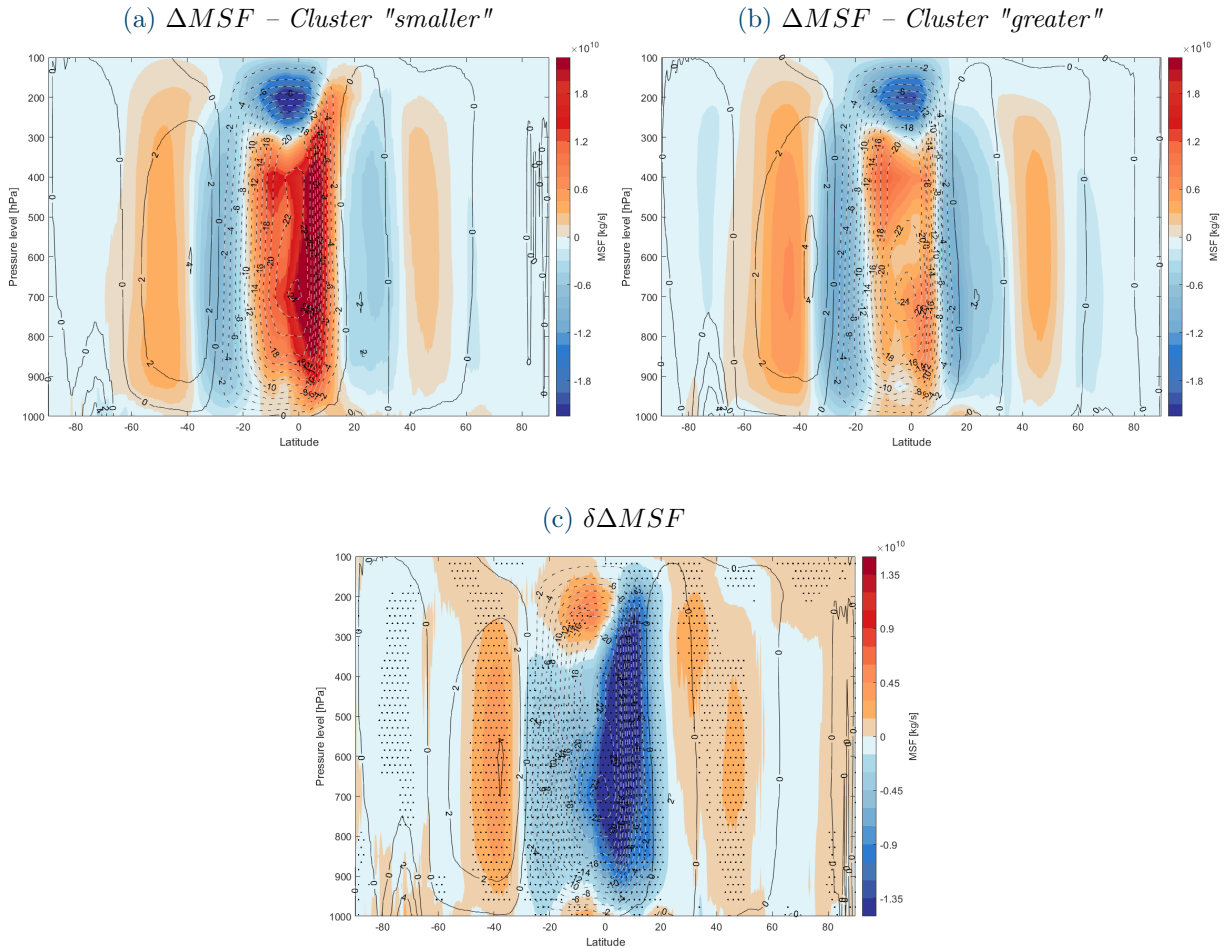


Figure 6.11: Average JJA meridional mass streamfunction (MSF) anomalies relative to 1850-1950 mean (Δ) for $GWL = +3\text{ }^{\circ}\text{C}$. **6.11a**: mean of the models of cluster "smaller"; **6.11b**: mean of the models of cluster "greater"; **6.11c**: difference between clusters "greater" and "smaller" (δ). In panels **6.11a** and **6.11b**, superimposed contours show the average historical JJA MSF computed from the models of the respective represented cluster; in panel **6.11c**, contours show the average historical JJA MSF computed from the models of both clusters (contour interval is $2 \times 10^{10}\text{ kg s}^{-1}$). Stippling indicates areas where the multi-model ensemble mean response is significant (95% confidence interval).

6.4.3 North Atlantic Oscillation (NAO) analysis

To further develop the overview of the impacts on the climate driven by projected changes in the Northern Hemisphere sea ice cover, an additional analysis has been carried out on one of the most important atmospheric teleconnection patterns: the North Atlantic Oscillation (NAO). A teleconnection pattern is a large-scale pattern of pressure and circulation anomalies, persistent over long timescales, generally higher than half a month. In fact, in the atmosphere energy is concentrated in structures with scales of thousands of kilometres or more, that are of interest for weather and climate. The NAO is the dominant mode of low-frequency variability in the North Atlantic: in fact, that sector exhibits a height correlation with a strong north-south dipole pattern, elongated in the east-west direction [78]. The NAO is usually related to the extent of the difference in sea level pressure between two areas of the North Atlantic, roughly coinciding with the Azores and Iceland. As set out during the description of the centres of action, the Azores are interested by a semipermanent anticyclone, so a high pressure area, whereas Iceland lies under a low pressure area – or cyclone – deeper during the winter months. The NAO switches between two distinct phases, which influence the European weather and climate in different ways. A *positive NAO phase* is defined whenever the difference between the Azores high and Icelandic low is particularly marked; whenever sea level pressure difference between the two areas is weaker, the mode is called a *negative NAO phase*. In the former configuration, eddies laden with humid air are deviated toward Northern Europe, without affecting the Mediterranean. During a negative NAO phase, on the other hand, eddies bring precipitation to the Mediterranean regions, while over Northern Europe the rainfall amount is lower [89].

Several methods have been developed to quantify the NAO signal, mainly related to the boreal winter months. Among these are the box-based calculation of the difference between SLPs, the computation of NAO index power spectra, the employment of Empirical Orthogonal Functions (EOFs) and the definition of “weather regimes” to distinguish the two phases of NAO. In this study, a first attempt of the quantification of the impacts on the North Atlantic Oscillation signal was performed based on the difference in DJF sea level pressures between two small boxes located around the Azores (28-20° W, 36-40° N) and Iceland (25-16° W, 63-70° N)². Then, for the computation of the NAO index we employed the function “nao” from the Climate Data Toolbox for MATLAB by Chad Greene [73]. The power spectrum of the detected signal was calculated as the squared absolute values of the amplitude of the discrete Fourier transform of these data. The spectra, calculated for the models of both clusters at the same GWL, were very noisy and, apart from the typical peak on the annual periodicity, didn’t represent any relevant difference in the models’ signal. This could be due to the poor representativeness of the two selected pressure boxes, quite small compared to the oceanic sector over which the NAO is detected.

Then, a more dynamic analysis has been performed to investigate whether impacts can be detected on the NAO signal due to Arctic sea ice decline, using the Empirical Orthogonal Function method. EOFs allow to identify the structures of the atmosphere that best describe the observed variance in a mean-square sense. It is an objective mathematical technique able to find spatial patterns in data that explain a disproportionate amount of variance. EOFs decompose a spatiotemporal field $A(x, y, t)$ into a series of spatial patterns $E_i(x, y)$ (the basis functions) mul-

² Coordinates from the reference boxes retrieved from Smith et al., 2022 [61].

multiplied by a timeseries of coefficients $w_i(t)$ (called principal components), only time-dependent:

$$A(x, y, t) = \sum_i w_i(t) E_i(x, y) \quad (6.5)$$

The basis functions (EOFs) are spatial fields that take advantage of the correlations between different locations to represent important fluctuations in the data, i.e., explain a lot of variance. The basis functions are chosen so that they are orthonormal to each other³

$$\iint E_i(x, y) E_j(x, y) dx dy = \delta_{ij} \quad (6.6)$$

and starting from the first, represent as much variance as possible in decreasing order [78] [89].

EOFs for the detection of the NAO signal are computed from the DJF Z_{500} field, whereby the first EOF, representing the highest variance, corresponds to the NAO. In this study, we make use of the Empirical Orthogonal Function Toolbox for MATLAB, realised by Zehun Wu [90]. Z_{500} values are taken for each model of the clusters keeping the monthly variability, over the area encompassed between 90° W-40° E and 20°-85° N. The EOFs are calculated from the monthly anomalies of geopotential height at 500 hPa of each model, in the 21-year period centred on the respective year of attainment of GWLs. Through the EOF analysis are retrieved the principal components too, which constitute the coefficients relative to the basis functions, multiplied by which they combine to generate a field for each month of the timeseries. With the principal components of the first obtained EOF, representative of the NAO, are computed spectra following the approach described before. Power spectra are a useful climatological analysis of the importance of the variability of the signal at each frequency. Unfortunately, neither these spectra, based on a broader area of the Atlantic Ocean, represent differences in the signal variability between one cluster and the other.

However, being the EOFs the representations of spatial patterns, this kind of analysis allows to visualise the NAO anomaly on a map. For this purpose, since different basis functions carry a different amount of variance, the EOFs are normalised as to represent the explained variance of the signal. EOFs are calculated also in the historical period of the models; then, the first EOF of the historical period of each model is subtracted from their respective first EOF at the different GWLs. Maps are plotted for the average of the models of cluster “greater” and for the average of the models of cluster “smaller”, and subtracted: in Fig. 6.12 is reported the map of the differences for GWL +3 °C. Also in this case is plotted stippling for indicating areas over which the results are statistically significant.

The map, which shows the same signal as GWL +2 °C but reinforced, demonstrates a marked increase in the NAO pattern over the North Atlantic, including Iceland, and an important decrease over Europe, centred on the Mediterranean Sea, which expands in a band affecting the subtropical latitudes. The centre of the area affected by NAO pattern increase due to sea ice loss lies halfway between the Azores and Iceland, thus making possible assessments not straightforward. However, Icelandic low is directly impacted by the area of increase, whereas the subtropical anticyclone is located at the border between the two effects, where the sign of the response changes. Furthermore,

³ In Eq. 6.6, δ_{ij} stands for the Kronecker delta, expressing the orthonormality condition.

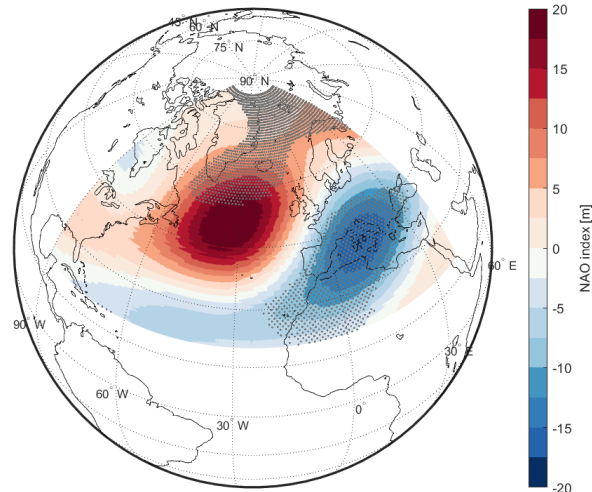


Figure 6.12: Map of DJF average NAO index difference between anomalies of clusters "greater" and "smaller" for $GWL = +3$ °C. Stippling indicates areas where the multi-model ensemble mean response is significant (95% confidence interval).

the spatial patterns are very similar to those representing negative NAO phases, even if shifted few degrees southward. One other aspect to take into account is the information provided by the statistical test: the response of the isolated impacts to sea ice is 95% significant over the blue area surrounding the Mediterranean and, for the area of positive difference, just at northern latitudes and where the Icelandic cyclone sits in winter months. A response similar to a negative NAO phase could affect European climate by leading to an increase in the Mediterranean precipitation.

In scientific literature dealing with impacts of Arctic sea ice decline on the atmospheric circulation, the assessments on the response of the NAO are not very homogeneous. For instance, Smith et al. (2022) cite a great number of modelling studies reporting contrasting responses, such as negative NAO, positive NAO, little response, and a response that depends on the details of the forcing or the background state of the climate system [61]. Overall, most of the research that finds a response of the NAO to Arctic sea ice loss detects a resemblance with a negative NAO phase [9] [81] [75] [37], consistent with higher SLP response over northern Eurasia, although a few report that it is not robust across models [80]. Ultimately, we should be cautious about interpretations of changes in the NAO signal due to projected NH sea ice decrease, also in light of the little consensus among modelling studies on the topic.

Conclusions

The purpose of this thesis is to investigate the role of future Arctic sea ice loss projected by CMIP6 models in shaping the response of the main climatic features to climate change. In order to isolate the contribution due to the strong reduction in sea ice in the Northern Hemisphere, two clusters of models have been formed based on different projections of sea ice cover anomalies at the end of the century relative to a historical baseline, normalised by the relative global mean temperature anomalies. Differences between the averages of the two clusters are attributed to differences in the magnitude of Arctic sea ice area decline, as supported by rigorous statistical testing. The impacts are studied at four levels of mean global warming, thereby allowing to consider more SSP scenarios all at once.

It results that the greatest sea ice loss will affect northern Barents Sea, in the surroundings of Franz Josef Land, and Greenland Sea. In these areas, as well as over Labrador Sea, sea ice projections exhibit the greatest differences across models. Local temperature responses come accordingly, owing to the strong ice-albedo feedback causing Arctic amplification. A general temperature rise affects the whole Northern Hemisphere, except certain Eurasian and North American regions, more markedly in boreal winter months. For other climatic responses, instead, the average annual trend is driven by the JJA response, which is usually not believed of great interest in this matter of research. For instance, in boreal summer changes in the equatorial precipitation are very intense, likely implying a shift in the ITCZ position. Overall, a greater change in sea ice cover leads to precipitation increase in the Northern Hemisphere, at the expense of a mean decrease in equatorial precipitation over the year. The effect is consistent with greater temperature rise in NH, which increases both local evaporation and the moisture content in the troposphere, besides influencing the atmospheric circulation patterns. Even the mean annual surface level pressure response to sea ice loss is governed by the summer distribution rather than winter one, even though the most relevant features affect the winter response. Among these, the most important cyclonic and anticyclonic patterns result weakened or strengthened by intense sea ice loss: examples are higher pressure over the Siberian high and the Icelandic low and weakening of the Azores anticyclone, in line with findings from similar studies.

Atmospheric circulation patterns are crucial in influencing regional and large-scale weather and climate and have therefore been deeply examined. Zonal winds, both from the perspectives of zonal-average cross sections and spatial patterns, and the meridional mass streamfunction, suitable for visualising the MMC, have been addressed. The former exhibit a weakening of the northern mid-latitude westerlies, accompanied by a southward shift, in response to sea ice cover changes. This result is largely consistent with other studies, which followed different methods, giving confidence of the soundness of the methodology adopted in this study for isolating response to future sea ice loss. Also the circulation of atmospheric cells results impacted, as the Hadley

cell gets weakened in both solstitial seasons. The Ferrel cell reduces in strength as well in DJF, in accordance with the identified weakening of mid-latitude westerly winds. We also attempted to find a response in the North Atlantic Oscillation, much debated across studies. The impact could resemble a negative NAO phase, consistent with some studies and with the detected changes in SLP patterns in the North Atlantic, but uncertainties remain, even if adopting several approaches.

Overall, the methodology applied for detecting changes on climate have been proved robust, both by statistical testing and from consistence with other research developed on the subject. The results are important as they provide assessments that Arctic sea ice loss is fundamental in all seasons for many climatic and atmospheric circulation responses to climate change, based on a large number of climate models.

Bibliography

- [1] N. T. Kurtz, NASA’s Goddard Space Flight Center, “GMS: Record-Breaking Climate Trends Briefing – July 19, 2016,” <https://svs.gsfc.nasa.gov/12305>, accessed: 2022-10-17.
- [2] J. C. Comiso, C. L. Parkinson, T. Markus, D. J. Cavalieri, and R. Gersten, “Current State of Sea Ice Cover,” <https://earth.gsfc.nasa.gov/cryo/data/current-state-sea-ice-cover>, accessed: 2022-10-17.
- [3] C. Kinnard, C. M. Zdanowicz, R. M. Koerner, and D. A. Fisher, “A changing Arctic seasonal ice zone: Observations from 1870–2003 and possible oceanographic consequences,” *Geophysical Research Letters*, vol. 35, no. 2, 2008.
- [4] W. Meier, D. Perovich, S. Farrell, C. Haas, S. Hendricks, A. Petty, M. Webster, D. Divine, S. Gerland, L. Kaleschke *et al.*, “Sea ice,” 2021.
- [5] Intergovernmental Panel on Climate Change, *Technical Summary*. Cambridge University Press, 2014, p. 31–116.
- [6] National Oceanic and Atmospheric Administration, “NOAA 200th Top Tens: Breakthroughs: The First Climate Model,” http://celebrating200years.noaa.gov/breakthroughs/climate_model/welcome.html, accessed: 2022-10-17.
- [7] B. C. O’Neill, C. Tebaldi, D. P. Van Vuuren, V. Eyring, P. Friedlingstein, G. Hurtt, R. Knutti, E. Kriegler, J.-F. Lamarque, J. Lowe *et al.*, “The scenario model intercomparison project (ScenarioMIP) for CMIP6,” *Geoscientific Model Development*, vol. 9, no. 9, pp. 3461–3482, 2016.
- [8] Intergovernmental Panel on Climate Change, *Summary for Policymakers*. Cambridge, United Kingdom and New York, NY, USA: Cambridge University Press, 2021, p. 3-32.
- [9] G. Zappa, F. Pithan, and T. G. Shepherd, “Multimodel evidence for an atmospheric circulation response to Arctic sea ice loss in the CMIP5 future projections,” *Geophysical Research Letters*, vol. 45, no. 2, pp. 1011–1019, 2018.
- [10] WCRP-CMIP, “Controlled Vocabularies (CVs) for use in CMIP6,” https://wcrp-cmip.github.io/CMIP6_CVs/docs/CMIP6_source_id.html, accessed: 2022-10-28.
- [11] Intergovernmental Panel on Climate Change, *The Ocean and Cryosphere in a Changing Climate: Special Report of the Intergovernmental Panel on Climate Change*. Cambridge University Press, 2022.

- [12] D. L. Hartmann, "Chapter 13 - Anthropogenic Climate Change," in *Global Physical Climatology (Second Edition)*, D. L. Hartmann, Ed. Boston: Elsevier, 2016, pp. 397–425.
- [13] I. V. Polyakov, A. Beszczynska, E. C. Carmack, I. A. Dmitrenko, E. Fahrback, I. E. Frolov, R. Gerdes, E. Hansen, J. Holfort, V. V. Ivanov, M. A. Johnson, M. Karcher, F. Kauker, J. Morison, K. A. Orvik, U. Schauer, H. L. Simmons, O. Skagseth, V. T. Sokolov, M. Steele, L. A. Timokhov, D. Walsh, and J. E. Walsh, "One more step toward a warmer Arctic," *Geophysical Research Letters*, vol. 32, no. 17, 2005.
- [14] F. Kauker, C. Koeberle, R. Gerdes, and M. Karcher, "Modeling the 20th century Arctic Ocean/Sea ice system: Reconstruction of surface forcing," *Journal of Geophysical Research*, vol. 113, 08 2008.
- [15] M. Steele, W. Ermold, and J. Zhang, "Arctic Ocean surface warming trends over the past 100 years," *Geophysical Research Letters*, vol. 35, no. 2, 2008.
- [16] NASA's Goddard Space Flight Center, "Arctic Sea Ice Reaches 2019 Minimum Extent," <https://svs.gsfc.nasa.gov/13309>, accessed: 2022-10-17.
- [17] L. Polyak, R. B. Alley, J. T. Andrews, J. Brigham-Grette, T. M. Cronin, D. A. Darby, A. S. Dyke, J. J. Fitzpatrick, S. Funder, M. Holland, A. E. Jennings, G. H. Miller, M. O'Regan, J. Saville, M. Serreze, K. St. John, J. W. White, and E. Wolff, "History of sea ice in the Arctic," *Quaternary Science Reviews*, vol. 29, no. 15, pp. 1757–1778, 2010, Special Theme: Arctic Palaeoclimate Synthesis (pp. 1674-1790).
- [18] I. H. Onarheim, T. Eldevik, L. H. Smedsrud, and J. C. Stroeve, "Seasonal and Regional Manifestation of Arctic Sea Ice Loss," *Journal of Climate*, vol. 31, no. 12, pp. 4917–4932, 2018.
- [19] I. H. Onarheim and M. Årthun, "Toward an ice-free Barents Sea," *Geophysical Research Letters*, vol. 44, no. 16, pp. 8387–8395, 2017.
- [20] J. E. Walsh, F. Fetterer, J. Scott Stewart, and W. L. Chapman, "A database for depicting Arctic sea ice variations back to 1850," *Geographical Review*, vol. 107, no. 1, pp. 89–107, 2017.
- [21] C. Kinnard, C. Zdanowicz, D. Fisher, E. Isaksson, d. V. Anne, and L. Thompson, "Reconstructed changes in Arctic sea ice over the past 1,450 years," *Nature*, vol. 479, pp. 509–12, 11 2011.
- [22] J. Halfar, W. H. Adey, A. Kronz, S. Hetzinger, E. Edinger, and W. W. Fitzhugh, "Arctic sea-ice decline archived by multicentury annual-resolution record from crustose coralline algal proxy," *Proceedings of the National Academy of Sciences*, vol. 110, no. 49, pp. 19737–19741, 2013.
- [23] J. Stroeve and D. Notz, "Changing state of Arctic sea ice across all seasons," *Environmental Research Letters*, vol. 13, no. 10, p. 103001, Sep 2018.

- [24] J. C. Stroeve, M. C. Serreze, M. M. Holland, J. E. Kay, J. Malanik, and A. P. Barrett, “The Arctic’s rapidly shrinking sea ice cover: a research synthesis,” *Climatic Change*, vol. 110, no. 3-4, pp. 1005–1027, Feb. 2012.
- [25] M. C. Serreze, J. Stroeve, A. P. Barrett, and L. N. Boisvert, “Summer atmospheric circulation anomalies over the Arctic Ocean and their influences on September sea ice extent: A cautionary tale,” *Journal of Geophysical Research: Atmospheres*, vol. 121, no. 19, pp. 11–463, 2016.
- [26] D. K. Perovich and C. Polashenski, “Albedo evolution of seasonal Arctic sea ice,” *Geophysical Research Letters*, vol. 39, no. 8, 2012.
- [27] J. Stroeve, T. Markus, L. Boisvert, J. Miller, and A. Barrett, “Changes in Arctic melt season and implications for sea ice loss,” *Geophysical Research Letters*, vol. 41, no. 4, pp. 1216–1225, 2014.
- [28] J. Liu, M. Song, R. M. Horton, and Y. Hu, “Revisiting the potential of melt pond fraction as a predictor for the seasonal Arctic sea ice extent minimum,” *Environmental Research Letters*, vol. 10, no. 5, p. 054017, 2015.
- [29] Robert B. Schmunk (NASA/GSFC GISS), “NASA’s Scientific Visualization Studio: Global Temperature Anomalies from 1880 to 2019,” <https://svs.gsfc.nasa.gov/4787>, accessed: 2022-10-18.
- [30] R. Kwok and D. Rothrock, “Decline in Arctic sea ice thickness from submarine and ICESat records: 1958–2008,” *Geophysical Research Letters*, vol. 36, no. 15, 2009.
- [31] J. Maslanik, J. Stroeve, C. Fowler, and W. Emery, “Distribution and trends in Arctic sea ice age through spring 2011,” *Geophysical Research Letters*, vol. 38, no. 13, 2011.
- [32] N. T. Kurtz and S. L. Farrell, “Large-scale surveys of snow depth on Arctic sea ice from Operation IceBridge,” *Geophysical Research Letters*, vol. 38, no. 20, 2011.
- [33] A. Schweiger, R. Lindsay, J. Zhang, M. Steele, H. Stern, and R. Kwok, “Uncertainty in modeled Arctic sea ice volume,” *Journal of Geophysical Research: Oceans*, vol. 116, no. C8, 2011.
- [34] M. Nicolaus, C. Katlein, J. Maslanik, and S. Hendricks, “Changes in Arctic sea ice result in increasing light transmittance and absorption,” *Geophysical Research Letters*, vol. 39, no. 24, 2012.
- [35] Intergovernmental Panel on Climate Change, *Summary for Policymakers*. Cambridge University Press, 2022, p. 3–36.
- [36] —, *Technical Summary*. Cambridge, United Kingdom and New York, NY, USA: Cambridge University Press, 2021, p. 33-144.
- [37] J. A. Screen, I. Simmonds, C. Deser, and R. Tomas, “The atmospheric response to three decades of observed Arctic sea ice loss,” *Journal of climate*, vol. 26, no. 4, pp. 1230–1248, 2013.

- [38] D. L. Hartmann, “Chapter 4 - The Energy Balance of the Surface,” in *Global Physical Climatology (Second Edition)*, D. L. Hartmann, Ed. Boston: Elsevier, 2016, pp. 95–130.
- [39] M. Serreze, A. Barrett, J. Stroeve, D. Kindig, and M. Holland, “The emergence of surface-based Arctic amplification,” *The Cryosphere*, vol. 3, no. 1, pp. 11–19, 2009.
- [40] J. A. Screen and I. Simmonds, “The central role of diminishing sea ice in recent Arctic temperature amplification,” *Nature*, vol. 464, no. 7293, pp. 1334–1337, 2010.
- [41] —, “Increasing fall-winter energy loss from the Arctic Ocean and its role in Arctic temperature amplification,” *Geophysical Research Letters*, vol. 37, no. 16, 2010.
- [42] I. Simmonds and K. Keay, “Extraordinary September Arctic sea ice reductions and their relationships with storm behavior over 1979–2008,” *Geophysical Research Letters*, vol. 36, no. 19, 2009.
- [43] J. E. Overland and M. Wang, “Large-scale atmospheric circulation changes are associated with the recent loss of Arctic sea ice,” *Tellus A: Dynamic Meteorology and Oceanography*, vol. 62, no. 1, pp. 1–9, 2010.
- [44] C. Strong, G. Magnusdottir, and H. Stern, “Observed feedback between winter sea ice and the North Atlantic Oscillation,” *Journal of Climate*, vol. 22, no. 22, pp. 6021–6032, 2009.
- [45] Q. Wu and X. Zhang, “Observed forcing-feedback processes between Northern Hemisphere atmospheric circulation and Arctic sea ice coverage,” *Journal of Geophysical Research: Atmospheres*, vol. 115, no. D14, 2010.
- [46] J. A. Francis and S. J. Vavrus, “Evidence linking Arctic amplification to extreme weather in mid-latitudes,” *Geophysical research letters*, vol. 39, no. 6, 2012.
- [47] D. Ghatak, A. Frei, G. Gong, J. Stroeve, and D. Robinson, “On the emergence of an Arctic amplification signal in terrestrial Arctic snow extent,” *Journal of Geophysical Research: Atmospheres*, vol. 115, no. D24, 2010.
- [48] M. Honda, J. Inoue, and S. Yamane, “Influence of low Arctic sea-ice minima on anomalously cold Eurasian winters,” *Geophysical Research Letters*, vol. 36, no. 8, 2009.
- [49] V. Petoukhov and V. A. Semenov, “A link between reduced Barents-Kara sea ice and cold winter extremes over northern continents,” *Journal of Geophysical Research: Atmospheres*, vol. 115, no. D21, 2010.
- [50] J. Liu, J. A. Curry, H. Wang, M. Song, and R. M. Horton, “Impact of declining Arctic sea ice on winter snowfall,” *Proceedings of the National Academy of Sciences*, vol. 109, no. 11, pp. 4074–4079, 2012.
- [51] S. Outten and I. Esau, “A link between Arctic sea ice and recent cooling trends over Eurasia,” *Climatic Change*, vol. 110, no. 3, pp. 1069–1075, 2012.

- [52] J. Inoue, M. E. Hori, and K. Takaya, “The role of Barents Sea ice in the wintertime cyclone track and emergence of a warm-Arctic cold-Siberian anomaly,” *Journal of Climate*, vol. 25, no. 7, pp. 2561–2568, 2012.
- [53] J. García-Serrano, C. Frankignoul, G. Gastineau, and A. De La Càmara, “On the predictability of the winter Euro-Atlantic climate: Lagged influence of autumn Arctic sea ice,” *Journal of Climate*, vol. 28, no. 13, pp. 5195–5216, 2015.
- [54] J.-S. Kug, J.-H. Jeong, Y.-S. Jang, B.-M. Kim, C. K. Folland, S.-K. Min, and S.-W. Son, “Two distinct influences of Arctic warming on cold winters over North America and East Asia,” *Nature Geoscience*, vol. 8, no. 10, pp. 759–762, 2015.
- [55] M. P. King, M. Hell, and N. Keenlyside, “Investigation of the atmospheric mechanisms related to the autumn sea ice and winter circulation link in the Northern Hemisphere,” *Climate dynamics*, vol. 46, no. 3, pp. 1185–1195, 2016.
- [56] A. Simon, C. Frankignoul, G. Gastineau, and Y.-O. Kwon, “An observational estimate of the direct response of the cold-season atmospheric circulation to the Arctic Sea Ice Loss,” *Journal of Climate*, vol. 33, no. 9, pp. 3863–3882, 2020.
- [57] T. Koenigk, Y. Gao, G. Gastineau, N. Keenlyside, T. Nakamura, F. Ogawa, Y. Orsolini, V. Semenov, L. Suo, T. Tian *et al.*, “Impact of Arctic sea ice variations on winter temperature anomalies in northern hemispheric land areas,” *Climate Dynamics*, vol. 52, no. 5, pp. 3111–3137, 2019.
- [58] S. Yang and J. H. Christensen, “Arctic sea ice reduction and European cold winters in CMIP5 climate change experiments,” *Geophysical Research Letters*, vol. 39, no. 20, 2012.
- [59] F. Ogawa, N. Keenlyside, Y. Gao, T. Koenigk, S. Yang, L. Suo, T. Wang, G. Gastineau, T. Nakamura, H. N. Cheung, N.-E. Omrani, J. Ukita, and V. Semenov, “Evaluating Impacts of Recent Arctic Sea Ice Loss on the Northern Hemisphere Winter Climate Change,” *Geophysical Research Letters*, vol. 45, no. 7, pp. 3255–3263, 2018.
- [60] R. Blackport, J. Screen, K. van der Wiel, and R. Bintanja, “Minimal influence of reduced Arctic sea ice on coincident cold winters in mid-latitudes,” *Nature Climate Change*, vol. 9, 09 2019.
- [61] D. M. Smith, R. Eade, M. Andrews, H. Ayres, A. Clark, S. Chripko, C. Deser, N. Dunstone, J. García-Serrano, G. Gastineau *et al.*, “Robust but weak winter atmospheric circulation response to future Arctic sea ice loss,” *Nature communications*, vol. 13, no. 1, pp. 1–15, 2022.
- [62] H.-N. Cheung, N. Keenlyside, T. Koenigk, S. Yang, T. Tian, Z. Xu, Y. Gao, F. Ogawa, N.-E. Omrani, S. Qiao *et al.*, “Assessing the influence of sea surface temperature and Arctic sea ice cover on the uncertainty in the boreal winter future climate projections,” *Climate Dynamics*, pp. 1–22, 2022.
- [63] T. Nakamura, K. Yamazaki, T. Sato, and J. Ukita, “Memory effects of Eurasian land processes cause enhanced cooling in response to sea ice loss,” *Nature communications*, vol. 10, no. 1, pp. 1–8, 2019.

- [64] R. E. Petrie, L. C. Shaffrey, and R. Sutton, “Atmospheric response in summer linked to recent Arctic sea ice loss,” *Quarterly Journal of the Royal Meteorological Society*, vol. 141, no. 691, pp. 2070–2076, 2015.
- [65] D. L. Hartmann, “Chapter 11 - Global Climate Models,” in *Global Physical Climatology (Second Edition)*, D. L. Hartmann, Ed. Boston: Elsevier, 2016, pp. 325–360.
- [66] J.-C. Golaz, P. M. Caldwell, L. P. Van Roekel, M. R. Petersen, Q. Tang, J. D. Wolfe, G. Abeshu, V. Anantharaj, X. S. Asay-Davis, D. C. Bader *et al.*, “The DOE E3SM coupled model version 1: Overview and evaluation at standard resolution,” *Journal of Advances in Modeling Earth Systems*, vol. 11, no. 7, pp. 2089–2129, 2019.
- [67] G. A. Meehl, R. Moss, K. E. Taylor, V. Eyring, R. J. Stouffer, S. Bony, and B. Stevens, “Climate Model Intercomparisons: Preparing for the Next Phase,” *Eos, Transactions American Geophysical Union*, vol. 95, no. 9, pp. 77–78, 2014.
- [68] C. Tebaldi and R. Knutti, “The use of the multi-model ensemble in probabilistic climate projections,” *Philosophical transactions of the royal society A: mathematical, physical and engineering sciences*, vol. 365, no. 1857, pp. 2053–2075, 2007.
- [69] Z. Hausfather, “CMIP6: the next generation of climate models explained,” <https://www.carbonbrief.org/cmip6-the-next-generation-of-climate-models-explained/>, accessed: 2022-10-28.
- [70] MATLAB, *9.9.0.1467703 (R2020b)*. Natick, Massachusetts: The MathWorks Inc., 2020.
- [71] K. Bellomo, M. Angeloni, S. Corti, and J. von Hardenberg, “Future climate change shaped by inter-model differences in Atlantic meridional overturning circulation response,” *Nature Communications*, vol. 12, no. 1, pp. 1–10, 2021.
- [72] I. Mahlstein and R. Knutti, “September Arctic sea ice predicted to disappear near 2°C global warming above present,” *Journal of Geophysical Research: Atmospheres*, vol. 117, no. D6, 2012.
- [73] C. A. Greene, K. Thirumalai, K. A. Kearney, J. M. Delgado, W. Schwanghart, N. S. Wolfenbarger, K. M. Thyng, D. E. Gwyther, A. S. Gardner, and D. D. Blankenship, “The Climate Data Toolbox for MATLAB,” *Geochemistry, Geophysics, Geosystems*, vol. 20, no. 7, pp. 3774–3781, 2019.
- [74] D. L. Hartmann, “Chapter 5 - The Hydrologic Cycle,” in *Global Physical Climatology (Second Edition)*, D. L. Hartmann, Ed. Boston: Elsevier, 2016, pp. 131–157.
- [75] R. Blackport and P. J. Kushner, “Isolating the Atmospheric Circulation Response to Arctic Sea Ice Loss in the Coupled Climate System,” *Journal of Climate*, vol. 30, no. 6, pp. 2163–2185, 2017.
- [76] CMIP6 Data Request, “MIP Variables,” <https://clipc-services.ceda.ac.uk/dreq/mipVars.html>, accessed: 2022-11-19.

- [77] J. M. Wallace and P. V. Hobbs, “3 - Atmospheric Thermodynamics,” in *Atmospheric Science (Second Edition)*, J. M. Wallace and P. V. Hobbs, Eds. San Diego: Academic Press, 2006, pp. 63–111.
- [78] D. L. Hartmann, “Chapter 8 - Natural Intraseasonal and Interannual Variability,” in *Global Physical Climatology (Second Edition)*, D. L. Hartmann, Ed. Boston: Elsevier, 2016, pp. 233–259.
- [79] American Meteorological Society, “Glossary of Meteorology,” <https://glossary.ametsoc.org/wiki/Welcome>, accessed: 2022-11-19.
- [80] H. N. Cheung, N. Keenlyside, N.-E. Omrani, and W. Zhou, “Remarkable Link between Projected Uncertainties of Arctic Sea Ice Decline and Winter Eurasian Climate,” *Advances in Atmospheric Sciences*, vol. 35, pp. 38–51, 01 2018.
- [81] C. Deser, L. Sun, R. A. Tomas, and J. Screen, “Does ocean coupling matter for the northern extratropical response to projected Arctic sea ice loss?” *Geophysical Research Letters*, vol. 43, no. 5, pp. 2149–2157, 2016.
- [82] B. Gan, L. Wu, F. Jia, S. Li, W. Cai, H. Nakamura, M. A. Alexander, and A. J. Miller, “On the Response of the Aleutian Low to Greenhouse Warming,” *Journal of Climate*, vol. 30, no. 10, pp. 3907–3925, 2017.
- [83] J. Screen, C. Deser, D. Smith, X. Zhang, R. Blackport, P. Kushner, T. Oudar, K. McCusker, and L. Sun, “Consistency and discrepancy in the atmospheric response to Arctic sea-ice loss across climate models,” *Nature Geoscience*, vol. 11, Feb. 2018.
- [84] Y. Peings, Z. M. Labe, and G. Magnusdottir, “Are 100 Ensemble Members Enough to Capture the Remote Atmospheric Response to +2°C Arctic Sea Ice Loss?” *Journal of Climate*, vol. 34, no. 10, pp. 3751–3769, 2021.
- [85] D. M. Smith, N. J. Dunstone, A. A. Scaife, E. K. Fiedler, D. Copsey, and S. C. Hardiman, “Atmospheric Response to Arctic and Antarctic Sea Ice: The Importance of Ocean–Atmosphere Coupling and the Background State,” *Journal of Climate*, vol. 30, pp. 4547–4565, 2017.
- [86] D. L. Hartmann, “Chapter 6 - Atmospheric General Circulation and Climate,” in *Global Physical Climatology (Second Edition)*, D. L. Hartmann, Ed. Boston: Elsevier, 2016, pp. 159–193.
- [87] P. Ceppi, G. Zappa, T. G. Shepherd, and J. M. Gregory, “Fast and Slow Components of the Extratropical Atmospheric Circulation Response to CO₂ Forcing,” *Journal of Climate*, vol. 31, no. 3, pp. 1091–1105, 2018.
- [88] S.-Y. Lee, J. C. H. Chiang, K. Matsumoto, and K. S. Tokos, “Southern Ocean wind response to North Atlantic cooling and the rise in atmospheric CO₂: Modeling perspective and paleoceanographic implications,” *Paleoceanography*, vol. 26, no. 1, 2011.
- [89] J. von Hardenberg, “Lecture notes of the course "The Climate System",” A.Y. 2020-2021, Master of Science in Environmental and Land Engineering – Politecnico di Torino.

- [90] Z. Wu, “Empirical Orthogonal Function Toolbox,” <https://github.com/zulunwu/eof/releases/tag/v1.2>, GitHub, 2022, retrieved on September 2022.

Abbreviations

| | |
|--------|---|
| AGCM | Atmospheric General Circulation Model |
| AMOC | Atlantic meridional overturning circulation |
| AOGCM | Atmosphere–Ocean General Circulation Model |
| AR | Assessment Report |
| CDO | Climate Data Operators |
| CMIP | Coupled Model Intercomparison Project |
| COP | Conference of the Parties |
| DJF | December-January-February |
| EOF | Empirical Orthogonal Function |
| ESGF | Earth System Grid Federation |
| GCM | Global Climate Model |
| GDP | Gross Domestic Product |
| GHG | Greenhouse gas |
| GMT | Global Mean surface air Temperature |
| GWL | Global warming level |
| IPCC | Intergovernmental Panel on Climate Change |
| ITCZ | Inter-Tropical Convergence Zone |
| JFM | January-February-March |
| JJA | June-July-August |
| MMC | Mean meridional circulation |
| MSF | Mass streamfunction |
| NAO | North Atlantic Oscillation |
| NetCDF | Network Common Data Form |
| NH | Northern Hemisphere |
| PAMIP | Polar Amplification Model Intercomparison Project |
| Ppm | Parts per million |
| RCP | Representative Concentration Pathway |
| Siconc | Sea ice concentration |
| SLP | Sea level pressure |
| SSP | Shared Socio-economic Pathway |
| SST | Sea surface temperature |
| Tas | Temperature at surface |
| UNFCCC | United Nations Framework Convention on Climate Change |
| WCRP | World Climate Research Programme |

